



저작자표시-비영리-변경금지 2.0 대한민국

이용자는 아래의 조건을 따르는 경우에 한하여 자유롭게

- 이 저작물을 복제, 배포, 전송, 전시, 공연 및 방송할 수 있습니다.

다음과 같은 조건을 따라야 합니다:



저작자표시. 귀하는 원저작자를 표시하여야 합니다.



비영리. 귀하는 이 저작물을 영리 목적으로 이용할 수 없습니다.



변경금지. 귀하는 이 저작물을 개작, 변형 또는 가공할 수 없습니다.

- 귀하는, 이 저작물의 재이용이나 배포의 경우, 이 저작물에 적용된 이용허락조건을 명확하게 나타내어야 합니다.
- 저작권자로부터 별도의 허가를 받으면 이러한 조건들은 적용되지 않습니다.

저작권법에 따른 이용자의 권리는 위의 내용에 의하여 영향을 받지 않습니다.

이것은 [이용허락규약\(Legal Code\)](#)을 이해하기 쉽게 요약한 것입니다.

[Disclaimer](#)

**Thesis for the degree of Doctor of Philosophy**

**Bioinspired Modification of TiO<sub>2</sub> and g-C<sub>3</sub>N<sub>4</sub> for Enhanced  
Photocatalytic Activities**

**The Graduate School of the University of Ulsan  
Department of Chemical Engineering**

**Yujie Wu**

**August 2023**

**Bioinspired Modification of TiO<sub>2</sub> and g-C<sub>3</sub>N<sub>4</sub> for Enhanced  
Photocatalytic Activities**

**Supervisor: Prof. Ik-Keun Yoo**

A Dissertation

Submitted to  
the Graduate School of the University of Ulsan  
In partial Fulfillment of the Requirements  
for the Degree of

**Doctor of Philosophy**

by

**Yujie Wu**

Department of Chemical Engineering

University of Ulsan, Korea

August 2023

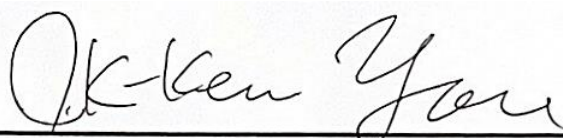
# Bioinspired Modification of $\text{TiO}_2$ and $g\text{-C}_3\text{N}_4$ for Enhanced Photocatalytic Activities

This certifies that the dissertation  
of **Yujie Wu** is approved.



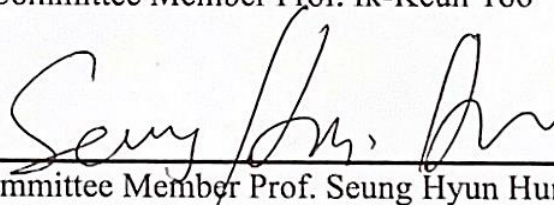
---

Committee Chair Prof. Won Mook Choi



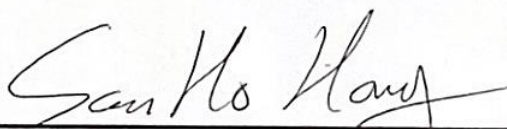
---

Committee Member Prof. Ik-Keun Yoo



---

Committee Member Prof. Seung Hyun Hur



---

Committee Member Prof. Soon-Ho Hong



---

Committee Member Prof. Yong Hwan Kim

Department of Chemical Engineering

University of Ulsan, Korea

August 2023

*This Thesis is dedicated to my thesis advisor, colleagues,  
friends, families, and my dearest sister.*

## ACKNOWLEDGEMENT

I am deeply grateful to all those who have contributed to the completion of my doctoral thesis. Their unwavering support and guidance have played an invaluable role in shaping my research journey over the past six years at UOU.

I would like to express my heartfelt appreciation to my advisor, *Prof. Ik-Keun Yoo*, for his profound expertise, invaluable insights, and thoughtful instruction throughout my whole journey. I extend my sincere gratitude to all the professors who have contributed to my academic development. Your profound knowledge, rigorous teachings, and invaluable feedback have broadened my perspectives and enhanced my understanding of my field of study. Moreover, I am deeply thankful to my colleagues and faculty members in the Chemical Engineering department for their camaraderie, insightful discussions, and willingness to collaborate. Your presence has not only made the research environment vibrant but also fostered a sense of community that I will cherish for a lifetime.

I am forever grateful to my family, especially my twin sister *Bingqing Wu*, for her unwavering belief in my abilities, constant encouragement, and unconditional love. Your understanding, patience, and devotion have provided me with the necessary support to overcome obstacles and pursue my passion.

Completing this Ph.D. thesis would not have been possible without the collective efforts, support, and inspiration of all these individuals. It was not an easy journey, I am deeply honored to have had such incredible mentors, colleagues, friends, and family members by my side.



## ABSTRACT

The rapid growth of industrial technologies has resulted in extended pollutant emissions and an energy shortage. In view of long-term development, it is essential to seek an economical, green, and effective method to remove existing pollutants and investigate substitute new energies to reduce hazardous emissions at their source. Photocatalysis is a promising approach to achieving solar energy conversion. Maximizing the utilization of solar irradiation and advancing photocatalytic efficiency are hot issues. The basic mechanism of photocatalysis can be summarized as follows: under solar irradiation, the excited electrons in the valence band (VB) of photocatalysts transfer to the conductive band (CB), leaving holes in the VB. Electrons and holes participate in redox reactions and generate free radicals such as  $\bullet\text{OH}$  and  $\text{O}_2^{\bullet-}$ . These powerful radicals further degrade organic pollutants into  $\text{H}_2\text{O}$ ,  $\text{CO}_2$ , and other organic residues, or participate in the water-splitting process for hydrogen evolution. However, most semiconductor photocatalysts face the obstacle of limited surface area and rapid recombination rate of photoinduced electron-hole pairs. Various methods such as element doping, morphology modulation, and heterostructure designing have been proven effective in resolving these problems. However, the requirement of strong acids, toxic chemicals, and harsh conditions in these processes might raise other environmental concerns. Inspired by nature, biomineralization and biomimetic modifications of photocatalysts have drawn attention due to their mild conditions and morphology direction. Additionally, the rich content of inorganic materials (such as carbon, nitrogen, and phosphorus) can provide in-situ element doping, which has been confirmed to narrow down the band gap and increase the separation rate of photoexcited charge carriers, thereby enhancing photocatalytic performance.

Lysozyme has been confirmed as a promising biotemplate for the mineralization of  $\text{TiO}_2$ . It is also an ideal candidate for incorporating negatively charged molecules such as polystyrene (PS) beads to form a reliable protein-polymer biotemplate with enriched organic components under ambient conditions. This protein-polymer template not only acts as the core to induce the nucleation of  $\text{TiO}_2$  but also introduces extra nitrogen as a dopant into the  $\text{TiO}_2$  lattice. Additionally, this protein-polymer template constructs a porous structure after the

calcination process, which enlarges the surface area of TiO<sub>2</sub>. Therefore, the lysozyme-polystyrene templated N-doped TiO<sub>2</sub> with increased surface area presents great photocatalytic degradation performance of Rhodamine B, a widely discharged organic dye pollutant, under simulated solar irradiation.

Graphitic carbon nitride (g-C<sub>3</sub>N<sub>4</sub>) is a promising metal-free semiconductor with non-toxic properties and abundant availability in nature. Its moderate band gap (2.7-2.8 eV) and remarkable thermal and chemical stability make it suitable for various applications, particularly in solar water splitting. However, the 3D structure of bulk g-C<sub>3</sub>N<sub>4</sub>, characterized by  $\pi$ - $\pi$  stacking and van der Waals forces between interlayers, poses a challenge in effectively separating photogenerated electron-hole pairs, thereby negatively impacting H<sub>2</sub> generation performance. To address this limitation and improve both solar light absorption and the recombination rate of photogenerated carriers, a simple and environmentally friendly approach has been proposed. In this study, a deformed g-C<sub>3</sub>N<sub>4</sub> structure was successfully modified with biological molecules by decorating a 14-mer peptide onto the porous g-C<sub>3</sub>N<sub>4</sub> (CN). The modified CN exhibited a modified morphology and improved visible-light absorption, resulting in superior photocatalytic H<sub>2</sub> production. It achieved a generation rate of 2018.4  $\mu\text{mol g}^{-1} \text{h}^{-1}$  without the need for a co-catalyst (such as Pt), which is approximately 14 times higher than that of pristine CN (140.8  $\mu\text{mol g}^{-1} \text{h}^{-1}$ ). Experimental along with theoretical computations have identified the deformation of CN structure caused by the electrostatic interaction between the positive-charge amine groups and the negative-charge edge N atoms. This interaction contributed to electron redistribution and delocalization, leading to the establishment of an electrical field and electronic modulation. Consequently, it enhanced charge separation and optimized the free energy of the reaction intermediates. This work presents a new approach for designing excellent bio-based, metal-free g-C<sub>3</sub>N<sub>4</sub>-based catalysts for visible-light photocatalytic H<sub>2</sub> generation.



# Table of Contents

<b>ACKNOWLEDGEMENT</b> .....	<b>I</b>
<b>ABSTRACT</b> .....	<b>II</b>
<b>Table of Contents</b> .....	<b>IV</b>
<b>List of Figures</b> .....	<b>VI</b>
<b>List of Tables</b> .....	<b>VIII</b>
<b>CHAPTER 1. Introduction</b> .....	<b>- 1 -</b>
1.1. Brief introduction of TiO <sub>2</sub> photocatalyst.....	- 2 -
1.1.1. Recent development of TiO <sub>2</sub> photocatalyst.....	- 3 -
1.1.2. Bioinspired strategies of TiO <sub>2</sub> fabrication .....	- 6 -
1.1.3. Photocatalytic applications of bioinspired TiO <sub>2</sub> .....	- 12 -
1.2. Brief introduction of g-C <sub>3</sub> N <sub>4</sub> photocatalyst.....	- 14 -
1.2.1. Traditional morphology-control fabrications of g-C <sub>3</sub> N <sub>4</sub> .....	- 16 -
1.2.2. Bioinspired modification of g-C <sub>3</sub> N <sub>4</sub> .....	- 19 -
1.2.3. Photocatalytic applications of bioinspired g-C <sub>3</sub> N <sub>4</sub> .....	- 24 -
Reference.....	- 29 -
<b>CHAPTER 2. Biom mineralization of TiO<sub>2</sub> by Lysozyme–Polystyrene Template for Enhanced Photocatalytic Activity</b> .....	<b>- 36 -</b>
2.1. Introduction .....	- 36 -
2.2. Experimental .....	- 38 -
2.2.1. Materials .....	- 38 -
2.2.2. Synthesis of template from LYZ and PS beads .....	- 38 -
2.2.3. Biom mineralization of TiO <sub>2</sub> .....	- 39 -
2.2.4. Characterization .....	- 40 -
2.2.5. Photocatalytic activity.....	- 40 -
2.3. Results and discussion.....	- 41 -
2.3.1. Adsorption of LYZ onto PS beads .....	- 41 -
2.3.2. Characteristics of synthesized TiO <sub>2</sub> .....	- 46 -

2.3.3. Photodegradation of RhB.....	- 54 -
2.4. Summary .....	- 57 -
Reference.....	- 59 -
<b>CHAPTER 3. Metal-free g-C<sub>3</sub>N<sub>4</sub> Modification via Peptide for Enhanced Photocatalytic Hydrogen Generation .....</b>	<b>- 63 -</b>
3.1. Introduction .....	- 63 -
3.2. Experimental .....	- 65 -
3.2.1. Materials .....	- 65 -
3.2.2. Synthesis of g-C <sub>3</sub> N <sub>4</sub> nanosheet .....	- 65 -
3.2.3. Synthesis of peptide-modified g-C <sub>3</sub> N <sub>4</sub> nanosheet .....	- 66 -
3.2.4. Photocatalytic hydrogen generation .....	- 66 -
3.2.5. Characterizations.....	- 66 -
3.2.6. Photoelectrochemical measurements .....	- 67 -
3.2.7. Molecular Dynamic (MD) computation.....	- 68 -
3.2.8. Density Functional Theory (DFT) computation.....	- 68 -
3.3. Results and discussion.....	- 70 -
3.3.1. Characteristics .....	- 71 -
3.3.2. Optical and photoelectrochemical properties.....	- 79 -
3.3.3. Photocatalytic H <sub>2</sub> generation.....	- 82 -
3.3.4. Plausible mechanisms .....	- 85 -
3.4. Summary .....	- 90 -
Reference.....	- 91 -
<b>CHAPTER 4. Conclusion .....</b>	<b>- 96 -</b>

## List of Figures

<b>Fig. 1.1.</b> The advantages and challenges of bioinspired fabrication of g-C <sub>3</sub> N <sub>4</sub> compared to traditional designs.....	- 21 -
<b>Fig. 2.1.</b> Schematic of TiO <sub>2</sub> mineralization using the lysozyme (LYZ)–polystyrene (PS) template. ....	- 39 -
<b>Fig. 2.3.</b> Zeta potential of ▲ lysozyme (LYZ), ● polystyrene (PS), and ■ LYZ–PS composites.....	- 44 -
<b>Fig. 2.4.</b> Field-emission scanning electron microscopy (FE-SEM) images of lysozyme (LYZ)–polystyrene (PS)–TiO <sub>2</sub> (LPT) particles calcined under different temperatures..	- 46 -
<b>Fig. 2.5.</b> FE-SEM images of the (a) bare TiO <sub>2</sub> , (b) bare TiO <sub>2</sub> -700, (c) LT, and (d) LT-700 particles. ...	- 47 -
<b>Fig. 2.6.</b> TEM images of the uncalcined LPT (a, b) and LPT-700 (c, d).....	- 48 -
<b>Fig. 2.7.</b> (a) TGA of pure polystyrene (PS), pure lysozyme (LYZ), LT, and LPT synthesized using the biotemplates at pH levels of 5.0, 8.5, and 10.0, respectively. (b) Fourier transform infrared (FTIR) spectra of the bare TiO <sub>2</sub> , PS, LPT, and LPT-500. ....	- 49 -
<b>Fig. 2.8.</b> XRD analysis of the bare TiO <sub>2</sub> , LPT, and LT particles (A, anatase; R, rutile).....	- 50 -
<b>Fig. 2.9.</b> Raman analysis of the (a) LPT and (b) LT particles (A, anatase; R, rutile).....	- 52 -
<b>Fig. 2.10.</b> (a) X-ray photoelectron spectroscopy (XPS) survey spectra of the bare TiO <sub>2</sub> -700, LT-700, and LPT-700. High-resolution spectra of (b) Ti 2p, (c) N 1s, and (d) O 1s. ....	- 52 -
<b>Fig. 2.11.</b> (a) Ultraviolet–visible (UV–VIS) absorption spectra and (b) Tauc plots for TiO <sub>2</sub> particles. (1) LPT-700, (2) LPT-800, (3) LT-700, (4) LT-800, (5) bare TiO <sub>2</sub> -700, and (6) bare TiO <sub>2</sub> -800.....	- 55 -
<b>FFig. 2.12.</b> Rhodamine B degradation under visible light by the calcined bare TiO <sub>2</sub> -700, LPT-700, and LP-700 particles (a, C/C <sub>0</sub> vs. t; b, ln (C/C <sub>0</sub> ) vs. t).....	- 55 -
<b>FFig. 2.13.</b> Rhodamine B degradation under visible light by LPT and LP at different calcination temperatures (a, C/C <sub>0</sub> vs. t; b, ln (C/C <sub>0</sub> ) vs. t).....	- 56 -
<b>Fig. 2.14.</b> Schematic of the photocatalytic mechanism of the mixed anatase/rutile phase TiO <sub>2</sub> . ....	- 57 -
<b>Fig. 3.1.</b> Illustration of sample preparation for electrochemistry analysis. ....	- 68 -
<b>Fig. 3.2.</b> Illustration of the synthesis of RSTB1 modified g-C <sub>3</sub> N <sub>4</sub> nanosheets. ....	- 71 -
<b>Fig. 3.3.</b> FE-SEM images (a), (b) and (c) peptide sequence of RSTB1. ....	- 71 -
<b>Fig. 3.4.</b> (a) FE-SEM image of CN, (b) TEM image of 10R-CN, and AFM images of (c) CN and (d) 10R-CN. (The inserted is the height profile of the peptide).....	- 72 -
<b>Fig. 3.5.</b> Nitrogen adsorption-desorption isotherms of (a) CN and 10R-CN, (b) bulk g-C <sub>3</sub> N <sub>4</sub> , and corresponding pore-size distribution of (c) CN and 10R-CN, (d) bulk g-C <sub>3</sub> N <sub>4</sub> . ....	- 73 -
<b>Fig. 3.6.</b> (a) TGA and (b) DTGA of RSTB1, CN, 2R-CN, 10R-CN and 15R-CN; (c) FTIR spectra and (d) Enlarged FTIR of RSTB1, CN, 2R-CN, 10R-CN and 15R-CN.....	- 74 -
<b>Fig. 3.7.</b> (a) Zeta potential at pH 7.5, (b) XRD patterns of CN, 2R-CN, 10R-CN and 15R-CN. (The inset is the enlarged XRD in the range of 25-30°).....	- 76 -

<b>Fig. 3.8.</b> XPS (a) survey spectra, High-resolution XPS spectra of (b) O 1s, (c) C 1s and (d) N 1s of CN and 10R-CN. ....	<b>76</b> -
<b>Fig. 3.9.</b> (a) MD snapshot of interaction event between RSTB1 and CN plane at 21. 8 ns. (b) The time-dependence centre of mass (COM) distance between CN and peptide. (c) Van der Waals and electrostatic interaction energies between components as the function of simulation.....	<b>78</b> -
<b>Fig. 3.10.</b> Optimal geometry of P-CN and D-CN. Top view (left) and side view (right).....	<b>78</b> -
<b>Fig. 3.11.</b> DFT computation of charge difference of (a) P-CN, (b) D-CN. QE-HSE calculated electronic band structure of (c) P-CN, (d) D-CN, and DOS of (e) P-CN and (f) D-CN.....	<b>79</b> -
<b>Fig. 3.12.</b> (a) UV-Vis absorption spectra and (b) Tauc plots, (c) PL emission spectra, (d) EIS Nyquist plots, (e) The transient photocurrent response curves, and (f) Time-resolved PL spectra of CN, 2R-CN, 10R-CN and 15R-CN. ....	<b>81</b> -
<b>Fig. 3.13.</b> (a) The amount of hydrogen generation vs. time and (b) hydrogen generation rate of CN, 2R-CN, 10R-CN and 15R-CN under visible-light irradiation. (c) Stability cycle runs for H <sub>2</sub> generation and (d) corresponding rate of 10R-CN in recycling runs. (e) Electrochemical HER LSV curves of CN and RSTB1-CN composites. (f) Hydrogen and oxygen photocatalytic generation performance of 10R-CN during continuous three cycling.....	<b>83</b> -
<b>Fig. 3.14.</b> (a) Hydrogen photocatalytic generation performance of 10R-CN, and CN with peptide [RFAAKAA] and peptide [VHLTPE]. (b) Illustration of peptide structures.....	<b>83</b> -
<b>Fig. 3.15.</b> CN and 10R-CN analysis of (a) Mott-Schottky plot, (b) band diagram, (c-d) UPS and DFT calculation of (e) P-CN, (f) 10R-CN. ....	<b>85</b> -
<b>Fig. 3.16.</b> Illustration of a plausible mechanism of peptide modified CN. ....	<b>87</b> -
<b>Fig. 3.17.</b> (a) EPR, (b) Water adsorption energy of bulk g-C <sub>3</sub> N <sub>4</sub> , P-CN and D-CN. (c) Gibbs Free energy reaction pathway of water splitting, (d) electrostatic potential map of P-CN and D-CN.....	<b>89</b> -
<b>Fig. 3.18.</b> (a) Optimized geometry of D-CN. DFT computed water adsorption models of (b) P-CN and (c) D-CN. And (d) illustration of water splitting on D-CN.....	<b>89</b> -

## List of Tables

<b>Table 2.1.</b> Langmuir and Freundlich parameters for lysozyme on PS beads.....	<b>45 -</b>
<b>Table 2.2.</b> Separation factor ( $R_L$ ) of polystyrene at various lysozyme concentrations at pH levels of 5.0, 8.5, and 10.0. ....	<b>45 -</b>
<b>Table 2.3.</b> Properties of LT and LPT particles in the mixed crystal phase. ....	<b>51 -</b>
<b>Table 2.4.</b> Kinetic data for rhodamine B photodegradation of the as-prepared $TiO_2$ photocatalysts.....	<b>56 -</b>
<b>Table 3.1.</b> TGA results of RSTB1-CN. ....	<b>75 -</b>
<b>Table 3.2.</b> Summary of the fluorescence decay lifetime parameters.....	<b>81 -</b>
<b>Table 3.3.</b> Summary of peptide properties. ....	<b>84 -</b>
<b>Table 3.4.</b> Biomaterial-based metal-free $g-C_3N_4$ for photocatalytic $H_2$ evolution. ....	<b>84 -</b>

## CHAPTER 1. Introduction

The global population reached 8 billion on November 2022 [1], and it is predicted that the worldwide energy demand will require two times its current supply by 2050 [2]. The energy shortage and environmental deterioration have never become severer hindering the long-term sustainable development of humanity. The technology of green energy such as solar-energy-conversion is promising for substituting traditional fossil fuels and reducing pollution thus stepping closer to the achievement of carbon neutrality [3]. Photocatalysis is a green process that can convert solar energy into chemical energy. In the past decades, due to its wide-ranging applications mostly in the field of degradation of pollutants and energy regeneration issues, a number of scientific papers on photocatalysis technology and its eco-friendly properties have been published. Traditional semiconductor metal oxides as photocatalysts such as CdS [4], Fe<sub>2</sub>O<sub>3</sub> [5], TiO<sub>2</sub> [6], ZnO<sub>2</sub> [7], and g-C<sub>3</sub>N<sub>4</sub> [8] have been widely used because of their stability, low-cost, non-toxicity, strong ability of pollutant degradation and high efficiency of hydrogen generation. For the maximum utilization of solar light, the modification for the photocatalyst with a larger surface area, appropriate redox potential, and moderate bandgap is the core. Many efforts have been made to promote photocatalytic activities via morphology design [8, 9], metal/non-metal-doping [10], and heterostructure construction [11, 12] in order to narrow down the band gap and suppress the recombination rater of photogenerated electron-hole pairs. However, the traditional synthesis and modification routes normally involved harsh experimental conditions like high temperature and high pressure, as well as toxic solvents and strong acid-based catalysts. Thus, it is crucial to develop facile, less toxic and environmental-friendly approaches for the synthesis and modification of photocatalyst.

Biom mineralization is not far away from our lives. In nature, living organisms can synthesize various inorganic minerals (i.e., skeletons, shells, teeth, etc.) through biom mineralization [13]. It is surprising that almost all the biom mineralization and biomimetic means in nature occur under ambient environments. The biological template not only endows mineralized tissues with better resilience compared with pure minerals but also regulates the

mineralization process, including nucleation, growth, phase transformation, orientation, and assembly [14]. Herein,  $\text{TiO}_2$  and  $\text{g-C}_3\text{N}_4$  as the most popular photocatalysts, that were modified via bioinspired strategies for the enhancement of photocatalytic efficiency are introduced.

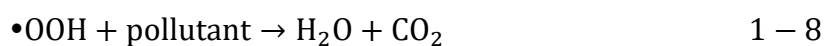
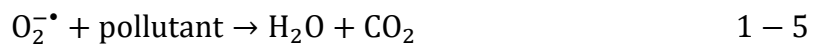
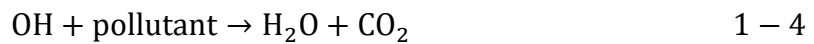
## **1.1. Brief introduction of $\text{TiO}_2$ photocatalyst**

Photocatalysis, the process of using light to drive chemical reactions, has garnered significant attention due to its potential for sustainable energy production and environmental remediation. Titanium dioxide ( $\text{TiO}_2$ ) is widely used as a photocatalyst due to its excellent stability, non-toxicity, and low cost.  $\text{TiO}_2$  photocatalyst is a highly studied and versatile material known for its ability to harness light energy and catalyze various chemical reactions. It is particularly renowned for its photocatalytic properties, which enable it to initiate and facilitate the decomposition of organic compounds, the removal of pollutants, and the generation of reactive oxygen species under light irradiation.  $\text{TiO}_2$  photocatalysis is widely applied in environmental remediation, water purification, air pollution control, self-cleaning surfaces, and solar energy conversion. Ongoing research aims to further enhance the photocatalytic efficiency, extend the light absorption range, and explore new methods for synthesizing  $\text{TiO}_2$  photocatalysts with improved performance.

However,  $\text{TiO}_2$  also exhibits limitations such as a wide bandgap and rapid electron-hole recombination, which hinder its photocatalytic efficiency. Overcoming these challenges requires innovative approaches, and bioinspiration provides valuable insights for improvement. Recent research focuses on refining design strategies, exploring novel bioinspired concepts, and developing scalable synthesis methods to enhance performance and broaden the scope of applications for  $\text{TiO}_2$  photocatalysis. Lately, bioinspired approaches have emerged as promising strategies to enhance the performance of photocatalytic materials. This involves leveraging insights from nature to optimize efficiency, selectivity, and practical applications of photocatalysts, including  $\text{TiO}_2$ . In this section, the background and recent development of  $\text{TiO}_2$  are summarized, and the bioinspired synthesis strategies and applications of  $\text{TiO}_2$  are briefly introduced.

### 1.1.1. Recent development of TiO<sub>2</sub> photocatalyst

Titanium dioxide (TiO<sub>2</sub>) is an n-type semiconductor with UV adsorption of  $\lambda < 400$  nm. TiO<sub>2</sub> is a highly promising solution for addressing water contamination issues due to its affordability, non-toxicity, and long-term stability. TiO<sub>2</sub> offers a diverse range of applications, including self-cleaning surfaces, photocatalytic water treatment, and air purification. It exists in three crystalline structures: rutile, anatase, and brookite, each with different band gaps. The band gaps for these structures are approximately 3.0 eV, 3.2 eV, and 3.4 eV, respectively [15]. Among the different crystalline structures, anatase exhibits a longer carrier lifetime and lower recombination rate. Typically, semiconductor oxide-based photocatalysts absorb solar radiation, with the energy of incident photons matching the band gap energy of the semiconductors. Upon exposure to solar radiation, the catalyst surface becomes activated, causing electrons to transition from the valence band (VB) to the conduction band (CB). Meanwhile, the holes remain in the VB and participate in oxidation reactions, generating hydroxyl ( $\bullet\text{OH}$ ) radicals. These powerful oxidants can then oxidize the pollutant species present in contaminated water. Concurrently, electrons in the CB undergo a reduction process and react with oxygen in the air to produce superoxide ( $\text{O}_2^{\bullet-}$ ) radicals. Additionally,  $\text{O}_2^{\bullet-}$  reacts with hydrogen ions ( $\text{H}^+$ ) to generate hydroperoxyl ( $\bullet\text{OOH}$ ) radicals. The hydroperoxyl radicals subsequently undergo reduction to form hydrogen peroxide ( $\text{H}_2\text{O}_2$ ), an active oxygen species that further degrade organic compounds, ultimately producing water ( $\text{H}_2\text{O}$ ) and carbon dioxide ( $\text{CO}_2$ ). The detailed photocatalytic activity of TiO<sub>2</sub> is presented in the equations below:



As mentioned above, the photocatalytic performance of TiO<sub>2</sub> is determined by the



generation of charge carriers, including electrons and holes, which occurs upon absorption of UV light corresponding to specific band gaps [16, 17]. The design principles to enhance photocatalysis efficiency can be summarized into three categories: increase the utilization of light, optimize surface reactions, and improve the migration of photogenerated carriers [18]. Morphology adjustment is one of the valid ways to achieve it. It has been widely reported that TiO<sub>2</sub> exhibits a variety of micro and nanostructures with unique properties and intriguing morphologies. For instance, zero-dimensional (0D) nanospheres possess a high specific surface area, making them well-suited for applications such as the rapid degradation of organic pollutants that occur on the photocatalyst's surface [17]. In contrast, one-dimensional (1D) fibers [19] and tubes [20] demonstrate higher photocatalytic efficiency due to reduced charge carrier recombination resulting from shorter diffusion distances for charge carriers [21, 22]. On the other hand, two-dimensional (2D) sheets exhibit a very smooth surface structure and higher adhesion power, which can further enhance photocatalytic activity [23, 24]. Moreover, three-dimensional (3D) titania structures offer several advantages due to their combination of high accessible surface areas and an interconnected network within the bulk titania phase. The spatial arrangement of solid and empty components in these structures provides opportunities to develop unique functionalities, including tunable anisotropy in transport properties, size-selective properties, and the ability to control interactions with light through photonic effects [25]. These different morphologies enable tailored design and optimization of TiO<sub>2</sub> photocatalysts for specific applications. By manipulating the morphology, it becomes possible to optimize parameters such as surface area, surface reactivity, and charge carrier dynamics, ultimately leading to improved photocatalytic performance.

Doped TiO<sub>2</sub> plays a crucial role in photocatalytic applications by modifying the optical response of the semiconductor photocatalyst, which including noble metals like Pt, Pd, Rh, Se, and Ag [26], non-metals such as S [27], N [28, 29], C [30], B [31], and P [32] are also used as dopants for TiO<sub>2</sub> photocatalysis. In general, doping can introduce impurity energy levels either below the conduction band minimum or above the valence band maximum can effectively narrow the bandgap, leading to enhanced light absorption. For example, Suwannaruang et al. [33] developed a nitrogen-doped TiO<sub>2</sub> for the photocatalytic degradation of ciprofloxacin. The hydrothermal technique was employed to prepare the N-TiO<sub>2</sub>

photocatalyst, utilizing urea as the nitrogen source. The incorporation of nitrogen dopants in N-TiO<sub>2</sub> resulted in a slightly lower bandgap energy compared to standard anatase TiO<sub>2</sub>. This nitrogen doping influenced the optical absorption behavior of TiO<sub>2</sub>. Within the lattice of anatase TiO<sub>2</sub>, the introduction of nitrogen led to the formation of structures such as Ti-N-O (substitutional N) and/or Ti-O-N (interstitial N) linkages. The photocatalysis results indicate that an increase in nitrogen content leads to a higher production of OH radicals, which can react more effectively with organic pollutants. The sample with the highest nitrogen content demonstrated approximately 66% removal of pollutants after 4 hours of reaction time, indicating significant decontamination capability. Gao's group [6] introduced a carbon doped TiO<sub>2</sub> via using butterfly wings as biotemplate. The final product not only inherited the hierarchical structure, but also obtained the carbon dopant originated from the wings. The presence of biomass carbon can inhibit grain growth and prevent TiO<sub>2</sub> particles from agglomerating. The C/TiO<sub>2</sub> presented advanced gas sensing properties at 300 °C and enhanced photocatalytic degradation efficiency of benzene and dimethylbenzene vapor in the comparison to Ag doped TiO<sub>2</sub>. Therefore, doping TiO<sub>2</sub> with biomass carbon offers a promising and cost-effective alternative to the expensive doping of metal Ag.

Additionally, the construction of heterostructure is another important method to improve TiO<sub>2</sub> photocatalytic performances. Du et al. [34] constructed a 3D CdS/TiO<sub>2</sub> heterostructure in the absence of a template. The large surface area and mesoporous morphology improved light harvesting so that boosted the photodegradation of antibiotics under visible light compared to pure TiO<sub>2</sub>. Karaolia et al. [35] fabricated a TiO<sub>2</sub>-rGO system applied in wastewater treatment plants. The synthesized photocatalysts demonstrated effective removal of target antibiotics in real wastewater effluents under simulated solar radiation. This study highlights the significant role that the composition of heterogeneous photocatalytic materials can play in the decontamination of wastewater containing a mixture of antibiotic compounds, as well as the disinfection of such matrices from pathogenic bacteria. TiO<sub>2</sub> has been combined with another semiconductor metal oxide that possesses a suitable band gap. This approach aims to enhance the charge separation efficiency and reduce the recombination of electron-hole pairs, ultimately improving the photocatalytic activity of TiO<sub>2</sub>. El-Yazeed's group [36] synthesized mesoporous WO<sub>3</sub>/TiO<sub>2</sub>. The 10 wt% loading of WO<sub>3</sub> on TiO<sub>2</sub> dramatically

boosted the photodegradation of methylene blue. The observed improvements in photodegradation activity can be attributed to the synergistic effects of interfacial heterojunctions.

This section explores improvement and modification strategies for designing high-performance photocatalysts aimed at pollutant removal in water. It acknowledges the challenge of effectively treating pollutants using a single technology and suggests that integrating photocatalysis with photo-electrocatalysis or electrocatalysis could be a promising alternative for efficient removal. The summary provides fresh insights into the design of highly efficient photocatalysts for degrading antibiotic residues, and dye pollutants, thereby advancing the application of photocatalysis in water treatment and other fields.

### **1.1.2. Bioinspired strategies of TiO<sub>2</sub> fabrication**

Nature provides a plethora of examples that inspire the design of TiO<sub>2</sub> photocatalysts. For instance, the process of photosynthesis, where natural systems efficiently harness solar energy, inspires the development of light-harvesting strategies for TiO<sub>2</sub>. By incorporating dyes or pigments or hybridizing TiO<sub>2</sub> with light-absorbing materials, researchers aim to enhance light absorption and utilization, leading to improved photocatalytic performance. Furthermore, natural systems with specialized surface structures offer inspiration for enhancing TiO<sub>2</sub> photocatalyst efficiency. By emulating bio-inspired nanostructures and coatings, researchers can optimize surface area, light scattering, and charge separation, leading to increased photocatalytic activity. In this section, the inspired synthesis strategies of TiO<sub>2</sub> are simply summarized into the “bottom-up” route, the bioinspired design of TiO<sub>2</sub>-based heterostructures, and the mechanisms.

#### **1.1.1.1. “Bottom-up” biomineralization of TiO<sub>2</sub>**

Since the initial discovery of titania through biomimetic mineralization [37], a wide range of titania and titania-based materials have been successfully synthesized. Biomaterial-based inducers have the ability to control the shape, composition, and arrangement of titania by acting as catalysts and/or structure-directing agents. Up to now, two types of

proteins/peptides have been utilized in the biomimetic method as catalysts and/or templates to facilitate the generation of inorganic nanomaterials.

First, natural proteins that extracted from organisms [38-40]. The remarkable ability of proteins to self-assemble nanostructures with superior properties compared to synthetic systems was initially observed in biomineralization studies of abalone shells. These shells consist of a multi-lamellar hierarchical structure, where highly oriented calcium carbonate crystals are interwoven with thin organic lamellae. The unique nano- and micro-architecture of abalone shells impart them with an extraordinary tensile fracture toughness that is approximately 3000 times greater than that of artificially produced calcium carbonate crystals. This natural example highlights the potential for harnessing protein-based self-assembly mechanisms to create advanced materials with exceptional mechanical properties and opens avenues for biomimetic design in materials science and engineering. Kharlampieva et al. [41] demonstrated that by tethering recombinant silaffins onto the surface of polyelectrolyte multilayers, a monolayer consisting of 4 nm titania nanoparticles could be formed after adding TiBALDH. The surface-bound silaffin molecules formed nanoscale domains that acted as templates for titania nanoparticle formation and prevented their aggregation. This process could be repeated to create thick, multifunctional nanoparticle composites. Jiang et al. [42] reported a novel approach for the preparation of protamine-titania hybrid microcapsules by combining layer-by-layer assembly with biomimetic mineralization. Protamine is a globular protein composed of 32 amino acid residues, with a notable feature of having 20-22 cationic arginine residues. This gives it a remarkably high isoelectric point (pI) of around 12, making it ideal for biomimetic synthesis of titania materials. When protamine was added to the Ti-BALDH solution, a white precipitate formed within a few minutes at room temperature, confirming its catalytic function in the titania formation process. The titania precipitates induced by protamine were found to be amorphous and exhibited a fused-particle morphology with a size of 50 nm. Importantly, this morphology was observed to be more regular than that achieved when using ammonium hydroxide as a catalyst for titania synthesis. Similarly, lysozyme is an optimal candidate for the incorporation of negatively charged molecules due to its high isoelectric point (pI ~ 10.7), enabling it to maintain a net positive charge across a wide pH range. Previous research has validated lysozyme's potential as a biotemplate for the

mineralization of inorganic materials. Luckarift et al. successfully synthesized amorphous titania particles in spherical form with sizes ranging from 10 to 50 nm using lysozyme as the inducer [39]. Additionally, Salman et al. achieved the production of TiO<sub>2</sub> hollow spheres with exceptional electrochemical properties as an anode material for lithium batteries using lysozyme templates in the presence of phosphate ions [43].

Second, artificially selected or designed proteins/peptides. Peptides found in nature have evolved to fulfill specific roles within living systems, but their ability to nucleate crystal formations is limited to certain morphologies and compositions. Many synthetic nanomaterials that have significant technological applications, such as semiconductors, are not naturally produced in biological systems. Therefore, the development of peptide-based organic templating systems for nanoparticle synthesis relies on the design of novel peptide sequences that possess functionalities beyond those found in nature. Phage display, a powerful combinatorial technique, enables the evolution of peptides by screening vast libraries of sequences. This approach facilitates the identification of molecular recognition peptides with high binding affinities for nanocrystals or crystal precursors, opening up possibilities for the creation of tailored peptide sequences for specific nanomaterial synthesis. Taking R5 peptide as an example, originating from the silaffin-1A protein of *Cylindrotheca fusiformis*, this peptide demonstrates the ability to promote and regulate the formation of silica, titanium phosphate, and TiO<sub>2</sub> in the ambient aqueous environment. In a study reported by Wright et al.[44], they conducted detailed investigations on the synthesis of titania nanoparticles using the R5 peptide as an inducer. Their findings revealed that the R5 peptide was capable of rapidly inducing the formation of titania within a few seconds, resulting in a relatively high yield. This effect was attributed to the peptide's high content of arginine and lysine residues. Selected by phage display technique, STB1 peptide was identified with high affinity to TiO<sub>2</sub>. Choi et al. [45] investigated the effects of peptide sequence and its local structure on TiO<sub>2</sub> biomineralization. While the affinity of a peptide to TiO<sub>2</sub> is important, it is not the sole factor determining its ability to mediate TiO<sub>2</sub> mineralization. The effectiveness of biomineralization is influenced by the intricate interplay between electrostatic interactions and mineralization kinetics, which are highly influenced by the peptide's sequence, conformation, and rigidity. Currently, the widespread adoption of peptide induced TiO<sub>2</sub> formation on a large scale is

limited by the high cost associated with customized peptides.

### **1.1.2.2. Biomimetic fabrication of TiO<sub>2</sub>-based composites**

Biomolecules employed in biomimetic mineralization possess the ability to catalyze the hydrolysis and condensation of water-soluble titanium precursors under mild conditions. These reactions occur in aqueous solutions with neutral pH, ambient temperature, and pressure [46]. Additionally, one notable advantage of biomimetic mineralization is the precise and intricate control exerted by biomolecules over the synthesis of inorganic materials. This control extends to crucial factors such as size, shape, and crystal structure, enabling the fabrication of highly tailored and precisely engineered nanomaterials. The combination of bio-adhesion and biomimetic methods provided a new aspect for hierarchical TiO<sub>2</sub> structures. For example, Jiang et al. [47] focus on the utilization of protamine for biomineralization chemistries in the synthesis of TiO<sub>x</sub>-SiO<sub>x</sub> nanomaterials. The resulting mineralized material exhibits a substantial proteinaceous content, which can be manipulated for enhanced surface area and the introduction of undercoordinated metal centers. This modular approach offers a means of controlling catalytic sites, allowing for customizable and tunable properties of the nanomaterials. Xu et al. [48] reported that two-dimensional hierarchically porous carbon composites have been successfully prepared using corn stalks as precursors, exhibiting exceptional performance as battery anodes and cathodes. In this process, the corn stalks undergo chemical activation to produce 2D carbon-based materials with hierarchical pores and high specific surface areas. Subsequently, TiO<sub>2</sub> particles are incorporated into the porous carbon sheets via infusion, followed by calcination in an inert atmosphere. The resulting TiO<sub>2</sub>/carbon composite demonstrates excellent cycling stability, high specific capacity, and remarkable rate capability, making it a highly efficient anode material for lithium-ion batteries. Liu et al. [49] designed a tertiary system of TiO<sub>2</sub>-SiO<sub>2</sub>-Ag nanocomposite induced by lysozyme. Lysozyme is employed as a catalyst to induce the fabrication of TiO<sub>2</sub> nanoparticles with an average size of approximately 280 nm. Following this, SiO<sub>2</sub> layers are generated via a sol-gel process, forming "pancake-like" structures protruding from the surface of the TiO<sub>2</sub> nanoparticles. The resulting nanocomposites exhibit a significant enhancement in

photocatalytic activity when exposed to visible light, particularly in the degradation of Rhodamine B. This improvement can be attributed to the combined effects of enhanced photon absorption facilitated by the surface plasma resonance of Ag nanocrystals and the increased adsorption capacity for Rhodamine B resulting from the high specific surface area of SiO<sub>2</sub>. These synergistic factors contribute to the superior photocatalytic performance observed in the nanocomposites.

Significant advancements have been made in the multidisciplinary fields of biology, chemistry, physics, and engineering, contributing to a comprehensive understanding of biomimetic titania and titania-based materials. The synthesis of these materials through biomimetic and bioinspired approaches has evolved into a powerful and versatile platform technology, offering inherent and potential advantages. Through the fusion of exploratory biomimetics and developmental bioinspiration, the future holds immense potential for the large-scale production of titania materials with enhanced energy efficiency, environmental sustainability, and precise control attributes. This convergence of scientific disciplines promises the realization of advanced titania materials that surpass conventional synthetic methods, enabling transformative applications in various sectors, ranging from energy production to environmental remediation.

### **1.1.2.3. Mechanism of biomimetic mineralization of titania**

Biom mineralization is a complex process in nature, involving a combination of physicochemical and biological mechanisms operating at various length scales. At its core, biom mineralization is initiated by organic scaffolds that exert precise control over the spatial localization of mineral nucleation and growth [50]. Therefore, to develop a rational framework for designing inorganic nanostructures using biomimetic templates, it is essential to comprehend the fundamental principles of crystal nucleation and growth. A profound understanding of the underlying physicochemical processes governing biom mineralization can offer valuable insights into the bottom-up assembly of nanostructured materials, enabling the design of advanced nanostructures. Gaining a comprehensive understanding of the mechanisms behind nucleation and growth in biom mineralization is not only of fundamental

interest but also holds the potential to guide the rational design of novel synthetic nanomaterials. Recent research suggests that a mechanistically informed biomimetic approach has the capacity to engineer nanostructures with superior structural control compared to conventional materials chemistry. For instance, in a simplified model system involving self-assembled organic thiol monolayers as templates, the cooperative reorganization of the underlying organic template was found to be strongly linked to its ability to guide the growth of crystals with preferred crystal orientation [14]. This highlights the potential for leveraging biomimetic principles to achieve precise control over the formation and properties of nanomaterials.

As for  $\text{TiO}_2$ , the initial proposal of the biomimetic synthesis mechanism of titania was put forward by Sumerel [37]. In their work, it was observed that hydrogen bonding between the hydroxyl groups of a specific serine-histidine pair in silicatein resulted in enhanced nucleophilicity of the serine oxygen. This facilitated an attack on the titanium in TiBALDH, leading to the formation of a temporary Ti-O bond with the protein. Ultimately, this interaction initiated the hydrolysis of TiBALDH at neutral pH. Later, Durupthy's group [51] demonstrated that in the biomimetic synthesis of titania, the hydroxyl group of serine acts as a nucleophile and attacks the titanium atom in TiBALDH. Concurrently, a pair of electrons on the nitrogen of histidine accepts the hydrogen from the hydroxyl group of serine. The exact mechanism of  $\text{TiO}_2$  biomineralization can vary depending on the specific biomolecule and experimental conditions, but overall, the biomolecules serve as templates and regulators of the nucleation, growth, and organization of  $\text{TiO}_2$ , ultimately leading to the formation of unique and controlled structures with desired properties. The  $\text{TiO}_2$  biomineralization thus can be summarized into several key steps. Biomolecules, such as proteins or peptides, with specific binding affinity for  $\text{TiO}_2$  act as templates for the mineralization process. These templates recognize  $\text{TiO}_2$  precursors and initiate nucleation, leading to the formation of small  $\text{TiO}_2$  nuclei on their surfaces. As the mineralization progresses, the  $\text{TiO}_2$  nuclei grow through the deposition of additional precursor molecules, guided by the template molecules. The template molecules also play a crucial role in controlling the morphology, crystal structure, and orientation of the growing  $\text{TiO}_2$  particles, acting as structure-directing agents. During maturation, the crystal structure of the  $\text{TiO}_2$  particles becomes more stable and ordered.



Additionally, the mineralized TiO<sub>2</sub> particles may aggregate or self-assemble, resulting in the formation of larger structures or hierarchical architectures.

### **1.1.3. Photocatalytic applications of bioinspired TiO<sub>2</sub>**

Bioinspired design strategies have successfully improved TiO<sub>2</sub> photocatalyst performance. It has emerged as a promising field with diverse applications. Drawing inspiration from natural systems, researchers have developed innovative approaches to enhance the performance of TiO<sub>2</sub> photocatalysts. These bioinspired TiO<sub>2</sub> materials exhibit unique properties and functionalities, making them suitable for a wide range of applications in various fields. As a result, bioinspired TiO<sub>2</sub> exhibits enhanced photocatalytic activities, offering a wide range of applications in environmental remediation, solar energy conversion, self-cleaning technologies, and biomedical fields.

One of the key applications of bioinspired TiO<sub>2</sub> is in environmental remediation. These photocatalysts have shown remarkable efficiency in the degradation of organic pollutants present in air, water, and soil. Organic dyes, widely used in industries and produced on a large scale, have become a significant component of industrial wastewater due to their extensive application [52]. Organic dyes characterize an important source of environmental contamination since they are toxic and mostly non-biodegradable. There are many different conventional treatment methods for the removal of these organic compounds from industrial wastewaters, such as adsorption, flocculation coagulation, electro-coagulation, and conventional chemical oxidation [53-55], but they are not effective enough in achieving total removal of these organic compounds. By harnessing solar energy, bioinspired TiO<sub>2</sub> can initiate photocatalytic reactions, leading to the breakdown of pollutants into harmless byproducts. This capability has significant implications for improving the quality of air and water, addressing concerns related to pollution and contamination. For example, Erdogan et al. [56] built a buckyball-shaped TiO<sub>2</sub> using *Lycopodium Clavatum* (LC) spores as biotemplates. The photocatalytic functionality and catalytic reusability of micron-sized buckyball-like TiO<sub>2</sub> architectures were investigated for the degradation of Rhodamine B. The results demonstrated that the photocatalytic activity of the TiO<sub>2</sub> overlayer could be deliberately modified by

controlling the surface coverage of anatase and rutile domains. Polydopamine (PDA) was utilized as the linker and inducer in a g-C<sub>3</sub>N<sub>4</sub>/TiO<sub>2</sub> heterojunction system [57]. Inspired by mussels, PDA can be coated on different surfaces via bio-adhesion properties. PDA is favorable in photocatalyst systems because its photoconductivity, biocompatibility, and excellent light harvest ability. The PDA was first coated on g-C<sub>3</sub>N<sub>4</sub> nanosheets by its adhesion capability, then the -NH<sub>2</sub> and -OH residue on the surface allows the biomineralization of TiO<sub>2</sub> induced by TiBALDH. The photocatalytic performance was identified by testing the visible-light degradation of RhB. The bioinspired heterostructure exhibited accelerated charge transfer which leads to a 100% RhB degradation within 60 minutes.

Another important application of bioinspired TiO<sub>2</sub> is in the field of energy conversion. These materials have been explored for solar energy harvesting and conversion into clean electricity or fuel. By mimicking natural processes, bioinspired TiO<sub>2</sub> photocatalysts enable efficient light absorption, charge separation, and conversion of solar energy into usable forms. This holds great promise for renewable energy generation and reducing our dependence on fossil fuels. Kim et al. [58] reported a route of TiO<sub>2</sub> nanoparticles biomineralization using three different biomolecules, namely peptide, protein, and virus, enabling the in-situ nitrogen-doping and morphology modification of TiO<sub>2</sub>. This biomineralization process resulted in the formation of TiO<sub>2</sub> nanoparticles with exceptional photocatalytic activity on hydrogen production. The biotemplates direct the morphologies and also provide extra organic substances into TiO<sub>2</sub>, which decreased the bandgap and extended the light absorption. Additionally, Ping et al. inspired by the electrostatic interaction between protein and TiBALDH, successfully synthesized rod-shape TiO<sub>2</sub> via cell display method. The ice nucleation protein (INP) served as an anchor on the surface of Escherichia coli (E. coli) cells for the artificial protein nR5, which can induce the hydrolysis of TiBALDH and form TiO<sub>2</sub>. E. coli cells served as a framework for the transformation of titanium dioxide precursors into well-assembled anatase TiO<sub>2</sub> nanoparticles with a size of 5 nm. The size of the nanoparticles was controlled by adjusting the number of tandem repeated units in the R5 segments. The resulting nanostructured anode, consisting of nanosized anatase crystals, a mesoporous structure, and a carbon coating, exhibited superior specific capacity, rate capability, and cycling stability compared to conventional electrodes when used as an anode electrode.

Bioinspired TiO<sub>2</sub> has also found applications in self-cleaning surfaces. Inspired by the lotus leaf's ability to repel water and resist dirt, bioinspired TiO<sub>2</sub> coatings can create superhydrophobic and self-cleaning surfaces [59]. When exposed to light, these coatings can break down organic matter and repel water, leading to surfaces that stay clean for longer periods. This technology has been utilized in various industries, such as architecture, automotive, and healthcare, where cleanliness and durability are essential [60]. Furthermore, bioinspired TiO<sub>2</sub> has shown potential in biomedical applications [61]. These photocatalysts can be employed for disinfection and sterilization of medical instruments and surfaces. By utilizing their antimicrobial properties, bioinspired TiO<sub>2</sub> materials can effectively eliminate pathogenic bacteria, viruses, and fungi. This has significant implications for healthcare settings, where maintaining a sterile environment is crucial. In the field of materials science, bioinspired TiO<sub>2</sub> has opened up new avenues for the development of functional materials. By mimicking natural structures and processes, researchers have been able to fabricate materials with unique properties, such as enhanced mechanical strength, improved conductivity, and tailored surface chemistry. These materials find applications in areas such as electronics, catalysis, sensors, and coatings.

In conclusion, bioinspired TiO<sub>2</sub> has revolutionized the field of photocatalysis, offering exciting opportunities for various applications. Its ability to replicate and enhance natural processes has led to significant advancements in environmental remediation, energy conversion, self-cleaning surfaces, biomedical applications, and materials science. Future research and development in this field hold great promise for addressing pressing global challenges and advancing sustainable technologies.

## **1.2. Brief introduction of g-C<sub>3</sub>N<sub>4</sub> photocatalyst**

Graphitic carbon nitride (g-C<sub>3</sub>N<sub>4</sub>) is contemplated as a visible light responsive and robust photocatalyst among all organic semiconducting materials since the pioneering work by Wang et al. in 2009 [62] when they produced hydrogen gas through the splitting of water under visible light irradiation. This metal-free polymeric semiconductor has garnered a lot of interest in solar light-driven photocatalysis owing to its myriads of advantages like non-toxicity,

inexpensiveness, abundant availability, thermal stability (up to 600 °C in air), good chemical inertness (in organic solvents, acids and bases), facile fabrication, appealing electronic band arrangement and moderate band gap of 2.7–2.8 eV corresponding to wavelength 450–460 nm of solar spectrum [63-66]. It's more negative CB potential (−1.3 V vs NHE at pH 7.0) and positive VB potential (1.4 V vs NHE at pH 7.0) allow thermo-dynamically to carry out redox reactions for various photocatalytic reactions under solar irradiation [67].

The photocatalytic reaction starts with the generation of photoexcited electron-hole pairs, then the electrons and holes transfer to the surface of the photocatalyst, triggering the redox reaction. To take full advantage of visible light energy, it is highly demanded to extend the light absorption edge of g-C<sub>3</sub>N<sub>4</sub> to 760 nm (the wavelength of electromagnetic waves that can be perceived by human's eyes is between 400 to 760 nm) [68]. Over the past decade, researchers have paid great efforts in engineering band gap and charging transfer path of g-C<sub>3</sub>N<sub>4</sub> by morphology control [69-73], element doping [74, 75], surface modification [76, 77], and constructing heterojunction to enhance the ultimate solar-to-hydrogen efficiency. Among all the strategies, morphology manipulation has gained great interests because the morphology has great effects on photocatalytic activity. A proper morphological modification could overcome the disadvantages of g-C<sub>3</sub>N<sub>4</sub> through improving the light absorption, accelerating the charge transfer rate, and preventing the fast recombination of photogenerated charge carriers. Traditionally, morphologies can be structured to varies shapes from 0-dimension to 3-dimension. Recently, bioinspired tactics of g-C<sub>3</sub>N<sub>4</sub> fabrications have attracted researchers' attentions due to the fascinating structures and functions. This new strategy can be divided into biomimetic fabrication and organics incorporation. The former concept refers to the functional and architectural based biosynthesis, that is, aiming to mimic the “properties” and the “structures”. The latter includes organic molecule doping, organic polymers, and metal organic frameworks (MOFs), etc.

Therefore, aiming to better understand the structure-property relationships of g-C<sub>3</sub>N<sub>4</sub>-based systems, the traditional morphology-control synthesis and bioinspired structural modifications and potential photocatalytic applications were summarized.

### 1.2.1. Traditional morphology-control fabrications of g-C<sub>3</sub>N<sub>4</sub>

The morphology-control fabrication is a useful way to boost the photocatalytic performance of g-C<sub>3</sub>N<sub>4</sub>. The morphology control aims to enhance the crystallinity, light absorption capacity, specific surface area, and efficiency of charge separation and transfer in g-C<sub>3</sub>N<sub>4</sub>-based systems. Commonly, the structures of g-C<sub>3</sub>N<sub>4</sub> can be fabricated from zero-dimension to three-dimensions, for example, g-C<sub>3</sub>N<sub>4</sub> quantum dots, nanorods/nanotubes/nanowires, nanosheets, nanospheres, and other structures, etc.

When materials are scaled down to the nanometer range, such as in the form of quantum dots, their charge transport behavior exhibits distinct quantum mechanical features. Quantum dot structures, characterized by a high surface-to-volume ratio, abundant surface atoms, and unsaturated coordination states, possess remarkable photocatalytic activity. These materials undergo a blue shift in their absorption spectra and exhibit widened band gaps, which in turn affect their electronic band structures during photocatalysis. Harnessing the advantages of quantum dot structures, grafting 0D quantum dots onto g-C<sub>3</sub>N<sub>4</sub> offers a promising approach to create numerous reactive active sites and enhance the photoelectric conversion ability, thereby significantly boosting the photocatalytic activity of the system. For example, Wang et al. [78] reported a thermal-chemical etching process was utilized to transform bulk g-C<sub>3</sub>N<sub>4</sub> into graphitic carbon nitride quantum dots (CNQDs). These CNQDs exhibit strong blue emissions and demonstrate up-conversion behavior. As a result, they can serve as efficient energy-transfer components in metal-free photocatalytic systems driven by visible light. The author thus that CNQDs are outstanding alternatives for universal energy-transfer components in metal-free photocatalytic systems driven by visible light. Another work developed the composites of g-C<sub>3</sub>N<sub>4</sub>/B doped g-C<sub>3</sub>N<sub>4</sub> quantum dots system [79]. In this study, a facile molten salt method was used to prepare B-doped g-C<sub>3</sub>N<sub>4</sub> quantum dots (BCNQDs) with a dot-like distribution of approximately 1.7 nm in diameter. The g-C<sub>3</sub>N<sub>4</sub>/BCNQDs heterojunction exhibited enhanced hydrogen evolution performance under visible light irradiation. The improved photocatalytic activity is attributed to the formation of a heterojunction between g-C<sub>3</sub>N<sub>4</sub> and BCNQDs, characterized by a well-matched band structure.

The field of g-C<sub>3</sub>N<sub>4</sub>-based materials has seen significant advancements with the

introduction of 1D nanostructures such as nanotubes, nanorods, and nanowires. These nanostructures provide numerous benefits to g-C<sub>3</sub>N<sub>4</sub>-based materials, including a high surface-to-volume ratio and abundant active sites, resulting in superior photoconductivity and efficient phonon and electron transport properties. Moreover, the construction of 1D nanostructures improves the thermal, electrical, and mechanical properties of g-C<sub>3</sub>N<sub>4</sub>-based materials. The nanoscale dimensions of 1D g-C<sub>3</sub>N<sub>4</sub>-based materials reduce the diffusion distance of photoexcited charges, facilitating charge separation during photocatalytic reactions. Additionally, the transformation of 2D g-C<sub>3</sub>N<sub>4</sub> into 1D structures introduces polygonal defects, creating active sites and increasing the contact surface area for enhanced photocatalytic reactions. These advancements in g-C<sub>3</sub>N<sub>4</sub>-based materials with 1D nanostructures have opened up new possibilities in various fields, including microelectronics, optoelectronic devices, and photocatalysis. Fan et al. [80] successfully synthesized sulfur-doped g-C<sub>3</sub>N<sub>4</sub> porous rods through a one-pot method by heating a supramolecular complex of melamine-tri-thiocyanuric acid. It was observed that tri-thiocyanuric acid self-assembled with melamine to form rod-like complexes through strong  $\pi$ - $\pi$  stacking interactions. Additionally, the porous structure with S doping effect has contributed in the enhanced photodegradation performance of RhB under visible light than that of bulk g-C<sub>3</sub>N<sub>4</sub>. He et al. [81] prepared a hollow cone-shaped tubular nanostructure composite of polyacrylonitrile-based carbon (C-PAN)/g-C<sub>3</sub>N<sub>4</sub>. The photocatalytic water splitting efficiency exhibited 16.7 times higher than that of pristine g-C<sub>3</sub>N<sub>4</sub>. The incorporation of a hollow nanotubular structure in the composite enhances the specific surface area of g-C<sub>3</sub>N<sub>4</sub>, improves light absorption, and facilitates efficient separation and transfer of charge carriers. These combined effects synergistically enhance the photocatalytic activity of the material.

The 2D g-C<sub>3</sub>N<sub>4</sub> nanosheets might be the most studied topic in the past decade. Exfoliating bulk g-C<sub>3</sub>N<sub>4</sub> into 2D g-C<sub>3</sub>N<sub>4</sub> nanosheets with single or few layers significantly increases the surface area of g-C<sub>3</sub>N<sub>4</sub>, providing ample adsorption and reaction active sites to enhance the catalytic reactions. Specifically, the presence of an ultrathin nanosheet structure in g-C<sub>3</sub>N<sub>4</sub> creates shorter electron/hole migration paths, facilitating efficient charge transfer to the g-C<sub>3</sub>N<sub>4</sub> surface and accelerating the photocatalytic reaction process. Shi and coworkers [82] utilized a facile electrostatic self-assembly method to incorporate UiO-66, a zirconium-based

metal-organic framework (MOF), with nanosized carbon nitride nanosheets (CNNS). The hybrid structure formed by integrating CNNS with UiO-66 takes advantage of UiO-66's substantial surface area and exceptional CO<sub>2</sub> capture capability. When the CNNS are photoexcited, they transfer electrons to UiO-66, effectively reducing electron-hole recombination within the carbon nitride nanosheets. Additionally, UiO-66 facilitates the efficient reduction of CO<sub>2</sub> molecules adsorbed within its structure by utilizing the long-lived electrons it supplies. Zhou et al. [83] have successfully achieved a significant enhancement in the production of H<sub>2</sub>O<sub>2</sub> by g-C<sub>3</sub>N<sub>4</sub> through the incorporation of ultrathin nanosheets with hierarchical pores and favorable energy band alignment. Specifically, they synthesized phosphorus-modified macro-mesoporous carbon nitride nanosheets (P-mMCNNS) using a facile one-step calcination method. This synthesis approach resulted in a hierarchical macro-mesoporous structure of g-C<sub>3</sub>N<sub>4</sub>, which facilitates faster mass transfer and promotes the H<sub>2</sub>O<sub>2</sub> production reaction at the liquid-solid-gas interface.

Unique 3D architectures are beneficial due to their capability of multiple light scattering and reflecting, which leads to enhanced light absorption. Also, the three-dimensional structures endow the high surface area that increases the absorption of target pollutants and increase the contact possibilities. Moreover, some 3D network structures can fix the cocatalysts within, effectively enhancing the reusability of photocatalysts. Zheng et al. [84] achieved optimization of hollow g-C<sub>3</sub>N<sub>4</sub> by adjusting its shell. The modification expands the  $\pi$ -conjugation system, leading to a red-shift in optical absorption and enhanced charge separation within the shell, while preserving the distinctive hollow polymeric nanoarchitecture. This strategy enables the adjustment of the semiconductor properties of the shell material in hollow carbon nitride nanostructures, resulting in the generation of redox species and improved photocatalytic activity for hydrogen evolution using visible light. Lin et al. [85] reported 3D ordered g-C<sub>3</sub>N<sub>4</sub> nanosphere arrays synthesized via hard-template method. The product shows remarkable photocatalytic H<sub>2</sub> evolution due to the presence of abundant point defect cavities in the material, which leads to excellent water adsorption properties and reduced light absorption.

As briefly introduced above, morphology control plays a vital role in designing g-C<sub>3</sub>N<sub>4</sub> materials with enhanced photocatalytic performance. Various strategies have been explored to

manipulate the structure of g-C<sub>3</sub>N<sub>4</sub>, including the formation of quantum dots, nanotubes, nanorods, nanosheets, and 3D architectures. These morphological modifications influence the light absorption, charge separation and transfer, and active surface area of g-C<sub>3</sub>N<sub>4</sub>, ultimately impacting its photocatalytic activity. Such control over the morphology of g-C<sub>3</sub>N<sub>4</sub> provides a foundation for researchers to develop innovative and bio-inspired designs, leading to the fabrication of highly efficient g-C<sub>3</sub>N<sub>4</sub>-based systems for applications in solar energy conversion and environmental remediation.

### **1.2.2. Bioinspired modification of g-C<sub>3</sub>N<sub>4</sub>**

Bioinspired g-C<sub>3</sub>N<sub>4</sub> modifications are divided into biomimetic fabrication and organics incorporation in this study. Biomimetic fabrication focuses on the structural mimicking from nature while organics incorporation refers to the organic-molecule-based functionalization. The design principle, mainstream strategies, and basic yet unique photocatalytic mechanisms will be introduced in this section.

#### **1.2.2.1. The design of bioinspired g-C<sub>3</sub>N<sub>4</sub> modification**

The bioinspired modification of g-C<sub>3</sub>N<sub>4</sub> for improved photocatalytic activities is considered to accelerate the redox reaction on its surface, which includes extended surface area for boosting mass transfer, and thinner-thickness structure for shortening charge transfer routes. Considering overcoming the disadvantages of bulk g-C<sub>3</sub>N<sub>4</sub>, constructing a 2D-structured g-C<sub>3</sub>N<sub>4</sub> sheet with specific morphologies and functions in a biomaterial-based manner has been proved efficient. Bioinspired modification can be divided into two main categories. One is mimicking the structures from nature to endow g-C<sub>3</sub>N<sub>4</sub> enhanced photocatalytic activities, for example, honeycomb-like [86], flower-like [87], leaf-like [88] and fish-scale-like [89] structures fabricated via hydrothermal/solvothermal routes were reported to have enhanced performances for their open-up layered morphologies. Another is incorporating organic compounds with g-C<sub>3</sub>N<sub>4</sub> to achieve specific functionalization. It is reported that the optical, electronic, and other properties of g-C<sub>3</sub>N<sub>4</sub> can be tuned by doping with organic molecules like aliphatic chain [90], benzene ring [91], and heterocyclic



compounds [92].

When synthesizing bioinspired g-C<sub>3</sub>N<sub>4</sub> composites, the synthesis strategies must be able to fulfill the requirements of the aiming products. Thermal condensation is the most investigated route for its easiness, efficiency, and large-scale ability. But the lack of regularity of the products' morphologies makes it hard to avoid aggregations [86]. The soft-template method is commonly used to fabricate nanomaterials with special morphologies since the intramolecular interactions can drive the added precursors (like micelles and microemulsions, etc.) into aggregations with various spatial structures. Although the impurities are unavoidable in the final photocatalytic products. Meanwhile, the hard-template method by using silicon, metal, and zeolite as templates to obtain helical-like and porous structure were widely studied [93]. Compared to the soft-template method, the hard-template method owns higher stability and more precise control for modifications of g-C<sub>3</sub>N<sub>4</sub> composites. However, the structure is more easily to be compromised during the removal of hard templates. Additionally, the method of supramolecular assembly has drawn much attention for bioinspired g-C<sub>3</sub>N<sub>4</sub> fabrication because of its non-toxicity and uncomplicated process. The precursors of g-C<sub>3</sub>N<sub>4</sub> (i.e., melamine, urea, and dicyandiamide, etc.) are applied to form supramolecular complexes (with/without additive agents) for the final g-C<sub>3</sub>N<sub>4</sub> photocatalysts with distinguished performance by regulating the tri-s-triazine structure units, which can further modulate its  $\pi$ -conjugation and thus optimize the optical and electronic characteristics of photocatalysts [94].

Compared to the conventional design methods of g-C<sub>3</sub>N<sub>4</sub>, bioinspired fabrications present certain advantages and disadvantages (Fig. 1.1). Firstly, bioinspired modifications provide various morphologies that can be observed from nature, while traditional morphology-control can only provide limited structures. Secondly, bioinspired g-C<sub>3</sub>N<sub>4</sub> compounds have the potential of inheriting the natural functions for solar light utilization (such as chloroplast-inspired structures), which further promote photocatalytic activities. Moreover, normally bioinspired structures with unique morphologies like fish-scale and leaf, etc. would show novel characteristics on optical and physical activities, as well as abnormal electron transfer mechanisms. However, there are also several challenges of bioinspired g-C<sub>3</sub>N<sub>4</sub>. Because of the randomness of natural compounds, the regularity of modified g-C<sub>3</sub>N<sub>4</sub> architecture is inadequate. Furthermore, the mechanism between structure and photocatalytic

activity is still not clear. Lastly, even though numerous researchers have laid eyes on the bioinspired field, the design of g-C<sub>3</sub>N<sub>4</sub> as photocatalysts is still at its initial stage. Thus, developing a bioinspired route for photocatalysis enhancement is highly promising yet urgent.

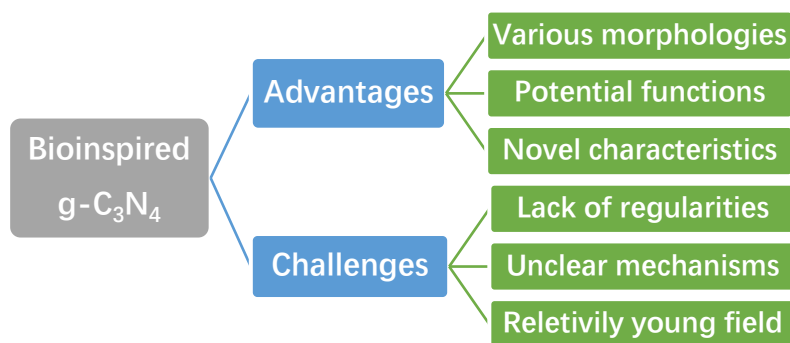


**Fig. 1.1.** The advantages and challenges of bioinspired fabrication of g-C<sub>3</sub>N<sub>4</sub> compared to traditional designs.

#### 1.2.2.2. Biomimetic fabrication for g-C<sub>3</sub>N<sub>4</sub>

Biomimetic fabrications of g-C<sub>3</sub>N<sub>4</sub> are referring to those structures which were artificially mimicked from nature. Taking beehives for example, the large surface area with the porous and heterogeneous structure makes honeycomb a promising photocatalyst material. By the thermal condensation method, Zhou et al. [86] reported a thin-shelled honeycomb-structured g-C<sub>3</sub>N<sub>4</sub>. After a simple co-calcination process of melamine/NH<sub>4</sub>Cl mixture, the g-C<sub>3</sub>N<sub>4</sub> product presented boosted photocatalytic hydrogen evolution efficiency with Pt as a co-catalyst. Huang et al.[95] designed a highly porous honeycomb g-C<sub>3</sub>N<sub>4</sub> via mixing cyanuric acid, urea, and melamine as the precursor, which optimized the honeycomb unit structure. This large-surface-area g-C<sub>3</sub>N<sub>4</sub> significantly increased the photocatalytic degradation efficiency on RhB compared to the bulk g-C<sub>3</sub>N<sub>4</sub>. Xiao et al. [96] synthesized a porous honeycomb-structured g-C<sub>3</sub>N<sub>4</sub> with a tunable structure through a one-pot template-free method. As-synthesized product (PGCN) exhibited enlarged surface area and proper defects on its surface, which is beneficial to the photocatalytic decomposition of p-hydroxybenzoic acid.

Aside from beehives, other fascinating structures of g-C<sub>3</sub>N<sub>4</sub> inspired by flowers and

leaves are also studied. Flowers with layers of pedals are the muses of multi-layered and hierarchical g-C<sub>3</sub>N<sub>4</sub> “designers”. Wu et al. [97] built a g-C<sub>3</sub>N<sub>4</sub>-based ternary flower-like heterojunctions for the photocatalytic reduction of Cr (VI). The layered structure of GO/g-C<sub>3</sub>N<sub>4</sub>/MoS<sub>2</sub> composite provides appropriate charge transfer channel and increased active sites for photocatalytic remediation of wasted water. By supramolecular self-assembly process of melamine-cyanuric acid aggregates, Duan et al. [98] prepared flower-like g-C<sub>3</sub>N<sub>4</sub> for NO oxidation under visible light irradiation. This flower-like g-C<sub>3</sub>N<sub>4</sub> with nitrogen vacancies shows an enhanced visible absorbance range and favorable suppression of photogenerated charge carriers. Thus, the photocatalytic oxidation efficiency of NO presents dramatic improvement compared to the bulk g-C<sub>3</sub>N<sub>4</sub>. Similarly, a leaf-shaped structure inspired by nature is also an interesting genre of g-C<sub>3</sub>N<sub>4</sub> architectures. Inspired by leaves, Zhao et al. [99] fabricated curly leaf-like g-C<sub>3</sub>N<sub>4</sub> nanosheets exfoliated from honeycomb-like porous g-C<sub>3</sub>N<sub>4</sub>. The leaf-shaped g-C<sub>3</sub>N<sub>4</sub> was improved to hold high efficiency on RhB photodegradation. Compared to traditional liquid exfoliation, this ultrasonic-assisted synthesis process is time-saving and easy scale-up. Also inspired by the leaf-mosaic structure, Zhang et al. [88] developed novel g-C<sub>3</sub>N<sub>4</sub> flakes via copolymerization of urea with dicyandiamide-formaldehyde resin. The sheet morphology was knitted along the polymer chain and assembled into a leaf-vein-like complex. This novel morphology with enlarged surface area shows enhanced light absorption, leading to a 38-time higher photocatalytic hydrogen evolution efficiency than pristine g-C<sub>3</sub>N<sub>4</sub>.

Similarly, a fish-scale structure was mimicked for the construction of porous g-C<sub>3</sub>N<sub>4</sub> sheets with high photocatalytic activities. Lin et al. developed a fish-scale-like g-C<sub>3</sub>N<sub>4</sub> with open-up sharp edges. The unique structure endows the photogenerated charge carriers to transfer along the large plane and gather at the edge of fish-scale slices. Such an unusual special charge transfer route significantly prompted the charge separation and prolonged the charge lifetime, which boosted the photocatalytic H<sub>2</sub> evolution efficiency. Other g-C<sub>3</sub>N<sub>4</sub>-based fish-scale like structures were reported to be beneficial for the photocatalytic performances on antibiotic degradation and oxygen evolution from its special charge transfer, strong interfacial reactions, and strong light utilization.[100, 101]

### 1.2.2.3. g-C<sub>3</sub>N<sub>4</sub>-based system with organics incorporation

Another important part of bioinspired g-C<sub>3</sub>N<sub>4</sub> fabrication is organics-incorporated systems. Mostly, g-C<sub>3</sub>N<sub>4</sub>-based photocatalyst systems involved toxic chemicals for fabrication, and metal ions as co-catalysts, which are costly and less environmental-friendly. However, the conjugation with organic materials shows a simple synthesis process and flexible structures of g-C<sub>3</sub>N<sub>4</sub>. Moreover, organic materials incorporation could improve the property of g-C<sub>3</sub>N<sub>4</sub> as well as reduces the processing cost in a greener means. The organic compounds' incorporation with g-C<sub>3</sub>N<sub>4</sub> can not only modify the molecular structures but also adjust the electronic structures of g-C<sub>3</sub>N<sub>4</sub>. Specifically, organic material with excellent semiconductor-like properties can be defined as organic semiconductors, which can be similarly divided into p-type and n-type semiconductors. The p-type semiconductor is when the main carriers are holes, and the ionization potential is relatively low while the highest occupied molecular orbital (HOMO) is high for the acceptance of holes. The n-type semiconductor, on the contrary, is when the main carriers are electrons. The high electron affinity and low lowest unoccupied molecular orbital (LUMO) are in ready for the acceptance of electrons. Organic semiconductors have been applied for organic light-emitting diode (OLED), solar cells, and photocatalysis fields. on a materials basis, organic semiconductors can be divided into macromolecules and small molecular compounds. The former mainly includes organic polymers while the latter refers to oligomers conjugations.

The organic polymers conjugated g-C<sub>3</sub>N<sub>4</sub> systems have the advantages of its stable, metal-free, pollutant-free, and favorable light adsorption, etc. Natural polymer like cellulose was used for g-C<sub>3</sub>N<sub>4</sub> modification. For example, Yang and coworkers [102] constructed mesoporous g-C<sub>3</sub>N<sub>4</sub> by using ethyl cellulose (EC) as a pore-forming agent during the pyrolysis process, also the obtained amorphous carbon was utilized for the modification of g-C<sub>3</sub>N<sub>4</sub> product. The optimized EC modified g-C<sub>3</sub>N<sub>4</sub> was then synthesized with ZnO, the resulting product shows about 8.5 times higher photocatalytic degradation on methylene blue than it on reference ZnO products. Yang et al. [103] synthesized highly efficient g-C<sub>3</sub>N<sub>4</sub>/CdS heterostructures by utilizing polydopamine (PDA) as an adhesion agent. PDA with enriched catechol and amine group make it a great adhesion material for g-C<sub>3</sub>N<sub>4</sub>. Also, the electrical

conductivity and the NIR region adsorption of the PDA layer assisted the charge migration between g-C<sub>3</sub>N<sub>4</sub> nanosheet and CdS, thus suppressing the photoelectron-hole recombination rate and promoting the photocatalytic activities on visible-light photodegradation of RhB. Yang's group [104] also reported a carbonized poly(tannic acid) (PTA) modified g-C<sub>3</sub>N<sub>4</sub> system. PTA nanorod was self-polymerized from tannic acid and applied as both template and adhesive for g-C<sub>3</sub>N<sub>4</sub>. Through bio-inspired adhesion, the final cPTA/g-C<sub>3</sub>N<sub>4</sub> porous nanorods exhibit enhanced photocatalytic activities towards RhB and tetracycline photodegradation by accelerated interfacial photoexcited charge transfer.

Besides, small organic materials can be catalyzed into three categories: aliphatic chain, benzene ring, and heterocyclic compounds.[105] For example, Zhao et al. [106] developed an amino group-rich g-C<sub>3</sub>N<sub>4</sub> via a simple oxalic acid-induced supramolecular self-assembly process. The amino group was introduced into tri-s-triazine structure units of g-C<sub>3</sub>N<sub>4</sub> with a fluffy and porous structure. The resulting product presents enhanced photocatalytic activities toward H<sub>2</sub> evolution. Liang et al. [107] developed benzene-modified GCN with a conjugated  $\pi$ - $\pi$  structure, resulting in improved photocatalytic performance due to enhanced charge separation and reduced bandgap. Zhang et al.[108] successfully introduced thiophene molecular into g-C<sub>3</sub>N<sub>4</sub> network. The incorporation adjusted the bandgap and modified electronic features by extending the aromatic  $\pi$ -conjugated system, leading to a promoted charge transfer and separation.

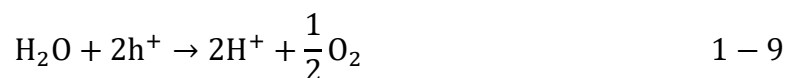
### **1.2.3. Photocatalytic applications of bioinspired g-C<sub>3</sub>N<sub>4</sub>**

Bioinspired g-C<sub>3</sub>N<sub>4</sub>, a metal-free, and visible light-responsive photocatalyst is highly regarded as a promising candidate for renewable energy development. Its desirable electronic band structure, electron-rich property, advanced surface functionality, excellent physical and chemical stability, and diverse properties contribute to its potential. In this thesis, we highlight the latest application possibilities of g-C<sub>3</sub>N<sub>4</sub>-based organic hybrid materials.

Hydrogen is a promising solar fuel due to its high energy density and non-polluting combustion product (water). Photocatalytic hydrogen evolution is a major focus of international research, with the design and modulation of semiconductor photocatalysts being

key. An ideal photocatalyst should have a suitable bandgap for efficient hydrogen evolution, flexible composition and structure for improved charge separation, and stability, low cost, and environmental friendliness for practical applications. The discovery of g-C<sub>3</sub>N<sub>4</sub> as a metal-free photocatalyst for H<sub>2</sub> evolution in 2009 has made graphitic carbon nitride a popular choice in photocatalysis. g-C<sub>3</sub>N<sub>4</sub> can be easily obtained from inexpensive N-rich precursors and its layered structure allows for various morphologies and structure adjustments. However, pristine g-C<sub>3</sub>N<sub>4</sub> has limitations in terms of visible-light absorption and charge recombination. Compared to metal oxide semiconductors, g-C<sub>3</sub>N<sub>4</sub>-based organic materials possess unique features including tunable nanostructures, improved electrical and thermal conductivities, enhanced stability, and abundant active sites. Thus, solar-driven water splitting over semiconductor photocatalysts under mild conditions is considered a promising strategy for the environmentally friendly production of H<sub>2</sub>. The basis of water splitting reactions is described below:

Oxidation:



Reduction:



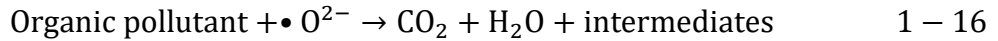
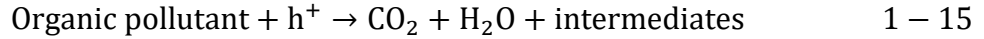
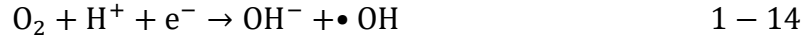
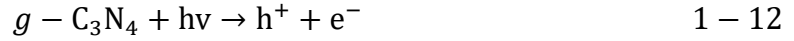
Overall:



As stated earlier, bioinspired designs for g-C<sub>3</sub>N<sub>4</sub> systems have novel morphologies, extend the light response, tunable band structures, and optimized charge migration properties, thus improving the photocatalytic activities. Chen et al. [105] applied pyrimidine-modified g-C<sub>3</sub>N<sub>4</sub> to photocatalytic hydrogen evolution. Pyrimidine has one less nitrogen atom than it of melamine, which created a deficiency in the supramolecular self-assembly process of the melamine-cyanuric mixture. This deficiency limited the expansion of g-C<sub>3</sub>N<sub>4</sub> and resulted in local structural distortion. The as-synthesized photocatalyst presents a slightly curled nanosheet morphology. The distorted planar triazine structure contributed to the generation of built-in electrical field. The local  $\pi$ - $\pi$  conjugation was enhanced because of the replacement

of nitrogen atom by carbon in the g-C<sub>3</sub>N<sub>4</sub> skeleton. Thus, the optical and electrical properties were promoted, further boosting the charge separation and advanced photocatalytic H<sub>2</sub> generation efficiency over 30 times over pristine g-C<sub>3</sub>N<sub>4</sub>. Zang et al. reported a copolymerization of g-C<sub>3</sub>N<sub>4</sub> with a pyrene-based polymer. A key benefit of copolymers is their ability to provide precise control over molecular-level structure and properties by continuously adjusting the ratio of monomers. Various pyrene-based polymers (PyP) that acts as an electron donor to enhance the transfer of charge carriers at the interface of g-C<sub>3</sub>N<sub>4</sub>. The hybridization of PyP/CN demonstrated  $\pi$ - $\pi$  stacking, which led to increased light absorption, improved charge carrier transfer, and the presence of more active sites on the surface. As a result, the hybrid exhibited enhanced activity compared to the individual components of parental CN and PyP. Notably, the boosted H<sub>2</sub> evolution didn't require Pt as a co-catalyst, which exhibited a new aspect of high efficiency, metal-free, green means of photocatalytic hydrogen evolution.

Environmental pollution has had a significant negative impact on human life and health. This is primarily due to the release of various pollutants that are challenging to eliminate or degrade naturally. Semiconductor photocatalysis is recognized as a highly efficient, cost-effective, and environmentally friendly method for addressing environmental pollution under mild conditions. In this regard, g-C<sub>3</sub>N<sub>4</sub>-based materials have emerged as promising candidates with excellent performance in photocatalytic degradation. Recently, g-C<sub>3</sub>N<sub>4</sub>-based materials are regarded as promising candidates due to their excellent photocatalytic degradation performance. As mentioned earlier, bio-inspired structured g-C<sub>3</sub>N<sub>4</sub>-based systems have gained popularity for their extensive use in the degradation of diverse pollutants. Due to the energy band position of g-C<sub>3</sub>N<sub>4</sub>, the photogenerated holes (h<sup>+</sup>) possess a high oxidation capacity. Furthermore, the photogenerated electrons (e<sup>-</sup>) effectively reduce O<sub>2</sub> to produce •O<sup>2-</sup>, while the photogenerated holes (h<sup>+</sup>) oxidize OH<sup>-</sup> to generate •OH. These active species (h<sup>+</sup>, •O<sup>2-</sup>, •OH) exhibit strong oxidation potential, enabling them to efficiently convert organic pollutants into CO<sub>2</sub> and H<sub>2</sub>O. The photoexcited pollutant degradation reactions are listed below:



Despite enhanced photocatalytic degradation efficiency of bioinspired g-C<sub>3</sub>N<sub>4</sub>, the systems are reported relatively lack stability. In order to enhance the mechanical strength, it is reasonable to incorporate bioinspired g-C<sub>3</sub>N<sub>4</sub> with sophisticated semiconductors such as TiO<sub>2</sub> to extend the application fields in an industrial aspect. Yang's group[67] constructed protamine-induced mineralization of amorphous titania (a-TiO<sub>2</sub>) on graphic carbon nitrate under room temperature in aqueous solution. The thickness of the a-TiO<sub>2</sub> nanoshell was regulated by changing the concentration of protamine and the mineralization cycles. The optimized resulting composite present the highest photocatalytic performance. The g-C<sub>3</sub>N<sub>4</sub> core absorbs visible light and creates electron-hole pairs. The a-TiO<sub>2</sub> nanoshell helps transfer the photogenerated electrons from g-C<sub>3</sub>N<sub>4</sub> to its surface, which regenerates NADH. This transfer also allows electron donor molecules (such as triethanolamine, TEOA) to move from the a-TiO<sub>2</sub> surface to g-C<sub>3</sub>N<sub>4</sub>, where they consume the holes left on g-C<sub>3</sub>N<sub>4</sub>. Tong et al. [46] developed a facile and efficient approach to prepare g-C<sub>3</sub>N<sub>4</sub>/TiO<sub>2</sub> nanocomposites. This method combines the biomimetic mineralization of TiO<sub>2</sub> using arginine with the thermal oxidation etching of bulk g-C<sub>3</sub>N<sub>4</sub>. The resulting g-C<sub>3</sub>N<sub>4</sub>/TiO<sub>2</sub> nanocomposites exhibit a well-defined morphology and structure. The enhanced RhB degradation performance was extended from visible light to the full solar light spectrum. Another bioinspired core-shell structured TiO<sub>2</sub>@g-C<sub>3</sub>N<sub>4</sub> was fabricated with glucose. Ma and coworkers [109]successfully coated g-C<sub>3</sub>N<sub>4</sub> onto TiO<sub>2</sub> hollow spheres obtained from glucose, through a two-step ultrasonic-assisted hydrothermal process. The TiO<sub>2</sub>@g-C<sub>3</sub>N<sub>4</sub> composite exhibited significantly enhanced photocatalytic activity compared to pure TiO<sub>2</sub> hollow microspheres. The photocatalytic activity on RhB degradation of the composite was nearly three times higher than that of the



reference TiO<sub>2</sub> hollow microspheres. Additionally, recycling tests confirmed the excellent stability of the TiO<sub>2</sub>@g-C<sub>3</sub>N<sub>4</sub> composite.

Apart from the aforementioned applications, bio-inspired structured g-C<sub>3</sub>N<sub>4</sub>-based systems have also been explored in other areas, including photocatalytic H<sub>2</sub>O<sub>2</sub> production, environmental disinfection, photocatalytic reduction of CO<sub>2</sub>, and the fixation of N<sub>2</sub>. Although these applications are still in their early research stages, they hold tremendous potential due to the unique advantages offered by bio-inspired g-C<sub>3</sub>N<sub>4</sub>-based systems. Other possibilities of applications such as utilizing various bio-inspired g-C<sub>3</sub>N<sub>4</sub>-based systems in solar cells are encouraged to be developed. By doing so, we can further advance the development of bio-inspired nanostructured g-C<sub>3</sub>N<sub>4</sub>-based photocatalysts and contribute to sustainable and innovative solutions in energy and environmental fields.

## Reference

- [1] World Population Prospects 2022: Summary of Results, United Nations Department of Economic and Social Affairs, 2022.
- [2] W.J. Ong, L.L. Tan, Y.H. Ng, S.T. Yong, S.P. Chai, Graphitic Carbon Nitride (g-C<sub>3</sub>N<sub>4</sub>)-Based Photocatalysts for Artificial Photosynthesis and Environmental Remediation: Are We a Step Closer To Achieving Sustainability?, *Chem Rev*, 116 (2016) 7159-7329.
- [3] U. Ulmer, T. Dingle, P.N. Duchesne, R.H. Morris, A. Tavasoli, T. Wood, G.A. Ozin, Fundamentals and applications of photocatalytic CO<sub>2</sub> methanation, *Nat Commun*, 10 (2019) 3169.
- [4] D.W. Wakerley, M.F. Kuehnel, K.L. Orchard, K.H. Ly, T.E. Rosser, E. Reisner, Solar-driven reforming of lignocellulose to H<sub>2</sub> with a CdS/CdOx photocatalyst, *Nature Energy*, 2 (2017).
- [5] C. Yavuz, S. Erten-Ela, Solar light-responsive α-Fe<sub>2</sub>O<sub>3</sub>/CdS/g-C<sub>3</sub>N<sub>4</sub> ternary photocatalyst for photocatalytic hydrogen production and photodegradation of methylene blue, *J Alloy Compd*, 908 (2022).
- [6] L. Gao, W. Gan, Z. Qiu, G. Cao, X. Zhan, T. Qiang, J. Li, Biomorphic Carbon-Doped TiO<sub>2</sub> for Photocatalytic Gas Sensing with Continuous Detection of Persistent Volatile Organic Compounds, *ACS Applied Nano Materials*, 1 (2018) 1766-1775.
- [7] Q.S. Guo, Q.H. Zhang, H.Z. Wang, Z. Zhao, ZnO<sub>2</sub>-promoted ZnO as an efficient photocatalyst for the photoreduction of carbon dioxide in the presence of water, *Catal Commun*, 103 (2018) 24-28.
- [8] L. Zhou, J. Feng, B. Qiu, Y. Zhou, J. Lei, M. Xing, L. Wang, Y. Zhou, Y. Liu, J. Zhang, Ultrathin g-C<sub>3</sub>N<sub>4</sub> nanosheet with hierarchical pores and desirable energy band for highly efficient H<sub>2</sub>O<sub>2</sub> production, *Appl. Catal. B: Environ.*, 267 (2020).
- [9] I. Papailias, N. Todorova, T. Giannakopoulou, N. Ioannidis, P. Dallas, D. Dimotikali, C. Trapalis, Novel torus shaped g-C<sub>3</sub>N<sub>4</sub> photocatalysts, *Appl. Catal. B: Environ.*, 268 (2020).
- [10] S. Weon, J. Kim, W. Choi, Dual-components modified TiO<sub>2</sub> with Pt and fluoride as deactivation-resistant photocatalyst for the degradation of volatile organic compound, *Appl. Catal. B: Environ.*, 220 (2018) 1-8.
- [11] Y. Wei, Y. Huang, Y. Fang, Y. Zhao, D. Luo, Q. Guo, L. Fan, J. Wu, Hollow mesoporous TiO<sub>2</sub>/WO<sub>3</sub> sphere heterojunction with high visible-light-driven photocatalytic activity, *Mater Res Bull*, 119 (2019) 110571.
- [12] E. Kusiak-Nejman, A. Wanag, J. Kapica-Kozar, Ł. Kowalczyk, M. Zgrzebnicki, B. Tryba, J. Przepiórski, A.W. Morawski, Methylene blue decomposition on TiO<sub>2</sub>/reduced graphene oxide hybrid photocatalysts obtained by a two-step hydrothermal and calcination synthesis, *Catalysis Today*, 357 (2020) 630-637.
- [13] H. Zeng, J. Xie, H. Xie, B.-L. Su, M. Wang, H. Ping, W. Wang, H. Wang, Z. Fu, Bioprocess-inspired synthesis of hierarchically porous nitrogen-doped TiO<sub>2</sub> with high visible-light photocatalytic activity, *Journal of Materials Chemistry A*, 3 (2015) 19588-19596.
- [14] C.-y. Wang, K. Jiao, J.-f. Yan, M.-c. Wan, Q.-q. Wan, L. Breschi, J.-h. Chen, F.R. Tay, L.-n. Niu, Biological and synthetic template-directed syntheses of mineralized hybrid and inorganic materials, *Progress in Materials Science*, 116 (2021).
- [15] C. Karthikeyan, P. Arunachalam, K. Ramachandran, A.M. Al-Mayouf, S. Karuppuchamy, Recent advances in semiconductor metal oxides with enhanced methods for solar photocatalytic applications, *J Alloy Compd*, 828 (2020).
- [16] A. Fujishima, X.T. Zhang, D.A. Tryk, TiO<sub>2</sub> photocatalysis and related surface phenomena, *Surf Sci Rep*, 63 (2008) 515-582.

- [17] K. Nakata, A. Fujishima, TiO<sub>2</sub> photocatalysis: Design and applications, *Journal of Photochemistry and Photobiology C: Photochemistry Reviews*, 13 (2012) 169-189.
- [18] X. Yang, Z. Chen, W. Zhao, C. Liu, X. Qian, M. Zhang, G. Wei, E. Khan, Y. Hau Ng, Y. Sik Ok, Recent advances in photodegradation of antibiotic residues in water, *Chem Eng J*, 405 (2021) 126806.
- [19] A.D.S. Montallana, B.Z. Lai, J.P. Chu, M.R. Vasquez, Enhancement of photodegradation efficiency of PVA/TiO<sub>2</sub> nanofiber composites via plasma treatment, *Mater Today Commun*, 24 (2020).
- [20] L. Thirugnanam, M. Palanisamy, S. Kaveri, S. Ramaprabhu, V.G. Pol, M. Dutta, TiO<sub>2</sub> nanoparticle embedded nitrogen doped electrospun helical carbon nanofiber-carbon nanotube hybrid anode for lithium-ion batteries, *Int J Hydrogen Energ*, 46 (2021) 2464-2478.
- [21] Y.Y. Li, S.Y. Liang, H.H. Sun, W. Hua, J.G. Wang, Defect Engineering and Surface Polarization of TiO<sub>2</sub> Nanorod Arrays toward Efficient Photoelectrochemical Oxygen Evolution, *Catalysts*, 12 (2022).
- [22] Y.M. Xu, X. Wang, M.L. Jin, K. Kempa, L.L. Shui, Water Splitting Performance Enhancement of the TiO<sub>2</sub> Nanorod Array Electrode with Ultrathin Black Phosphorus Nanosheets, *Chemelectrochem*, 7 (2020) 96-104.
- [23] Y. Aoyama, Y. Oaki, R. Ise, H. Imai, Mesocrystal nanosheet of rutile TiO<sub>2</sub> and its reaction selectivity as a photocatalyst, *Crystengcomm*, 14 (2012) 1405-1411.
- [24] Y.Y. Zhang, H. Liu, J.Y. Cui, X.S. Bai, D.Y. Yang, H.Y. Yuan, B.M. Wang, Research on the Thickness and Microstructure of Plate-like TiO<sub>2</sub> by the Nanosheet-Seeding Growth Technique, *Coatings*, 12 (2022).
- [25] D. Fattakhova-Rohlfing, A. Zaleska, T. Bein, Three-dimensional titanium dioxide nanomaterials, *Chem Rev*, 114 (2014) 9487-9558.
- [26] Y.Q. Lu, H. Deng, T.T. Pan, L. Wang, C.B. Zhang, H. He, Interaction between noble metals (Pt, Pd, Rh, Ir, Ag) and defect-enriched TiO<sub>2</sub> and its application in toluene and propene catalytic oxidation, *Applied Surface Science*, 606 (2022).
- [27] T.T. Ju, Y. Dai, H.L. Tang, M.L. Wang, M. Wang, Y.Q. Ma, G.H. Zheng, S-doped TiO<sub>2</sub> spindles wrapped by graphene with high exposed {001} faces and intimate contact, *Ceramics International*, 47 (2021) 24793-24801.
- [28] K. Dey, S. Vaidya, A. Gobetti, G. Ramorino, A.K. Ganguli, Facile synthesis of N-doped biphasic TiO<sub>2</sub> nanoparticles with enhanced visible light-driven photocatalytic performance, *Mater Today Commun*, 33 (2022).
- [29] Y.X. Wang, J.F. Chen, X.L. Zhang, Y.Q. Yang, Q.L. Yang, X.F. Liu, X.F. Tao, Y.X. Jin, G. Lu, X.D. Zhang, N-doped rutile TiO<sub>2</sub>/C hybrids with enhanced charge transfer capability derived from NH<sub>2</sub>-MIL-125(Ti) for the photocatalytic degradation of tetracycline, *Mater Res Bull*, 155 (2022).
- [30] A. Piatkowska, M. Janus, K. Szymanski, S. Mozia, C-,N- and S-Doped TiO<sub>2</sub> Photocatalysts: A Review, *Catalysts*, 11 (2021).
- [31] R.P. Cavalcante, R.F. Dantas, B. Bayarri, O. Gonzalez, J. Gimenez, S. Esplugas, A. Machulek, Synthesis and characterization of B-doped TiO<sub>2</sub> and their performance for the degradation of metoprolol, *Catalysis Today*, 252 (2015) 27-34.
- [32] K.D. Wang, J. Yu, L.J. Liu, L. Hou, F.Y. Jin, Hierarchical P-doped TiO<sub>2</sub> nanotubes array@Ti plate: Towards advanced CO<sub>2</sub> photocatalytic reduction catalysts, *Ceramics International*, 42 (2016) 16405-16411.
- [33] T. Suwannaruang, P. Kidkhunthod, N. Chanlek, S. Soontaranon, K. Wantala, High anatase purity of nitrogen-doped TiO<sub>2</sub> nanorice particles for the photocatalytic treatment activity of pharmaceutical wastewater, *Applied Surface Science*, 478 (2019) 1-14.

- [34] Y.B. Du, L. Zhang, M. Ruan, C.G. Niu, X.J. Wen, C. Liang, X.G. Zhang, G.M. Zeng, Template-free synthesis of three-dimensional porous CdS/TiO<sub>2</sub> with high stability and excellent visible photocatalytic activity, *Materials Chemistry and Physics*, 212 (2018) 69-77.
- [35] P. Karaolia, I. Michael-Kordatou, E. Hapeshi, C. Drosou, Y. Bertakis, D. Christofilos, G.S. Armatas, L. Sygellou, T. Schwartz, N.P. Xekoukoulotakis, D. Fatta-Kassinos, Removal of antibiotics, antibiotic-resistant bacteria and their associated genes by graphene-based TiO<sub>2</sub> composite photocatalysts under solar radiation in urban wastewaters, *Appl. Catal. B: Environ.*, 224 (2018) 810-824.
- [36] W.S.A. El-Yazeed, A.I. Ahmed, Photocatalytic activity of mesoporous WO<sub>3</sub>/TiO<sub>2</sub> nanocomposites for the photodegradation of methylene blue, *Inorg Chem Commun*, 105 (2019) 102-111.
- [37] J.L. Sumerel, W.J. Yang, D. Kisailus, J.C. Weaver, J.H. Choi, D.E. Morse, Biocatalytically templated synthesis of titanium dioxide, *Chem Mater*, 15 (2003) 4804-4809.
- [38] C. Liu, Z. Jiang, Z. Tong, Y. Li, D. Yang, Biomimetic synthesis of inorganic nanocomposites by a de novo designed peptide, *RSC Adv.*, 4 (2014) 434-441.
- [39] H.R. Luckarift, M.B. Dickerson, K.H. Sandhage, J.C. Spain, Rapid, room-temperature synthesis of antibacterial bionanocomposites of lysozyme with amorphous silica or titania, *Small*, 2 (2006) 640-643.
- [40] G. Chen, M. Li, F. Li, S.R. Sun, D.G. Xia, Protein-Mediated Synthesis of Nanostructured Titania with Different Polymorphs at Room Temperature, *Advanced Materials*, 22 (2010) 1258-1262.
- [41] E. Kharlampieva, T. Tsukruk, J.M. Slocik, H. Ko, N. Poulsen, R.R. Naik, N. Kroger, V.V. Tsukruk, Bioenabled surface-mediated growth of titania nanoparticles, *Advanced Materials*, 20 (2008) 3274-+.
- [42] Y.J. Jiang, D. Yang, L. Zhang, Q.Y. Sun, X.H. Sun, J. Li, Z.Y. Jiang, Preparation of Protamine-Titania Microcapsules Through Synergy Between Layer-by-Layer Assembly and Biomimetic Mineralization, *Advanced Functional Materials*, 19 (2009) 150-156.
- [43] M.S. Salman, A.R. Park, M.J. Cha, Y. Choi, S.K. Jang, L. Tan, P.J. Yoo, W.-S. Choe, Lysozyme-Templated Meso-Macroporous Hollow TiO<sub>2</sub> for Lithium Ion Battery Anode, *ACS Applied Nano Materials*, 1 (2018) 698-710.
- [44] S.L. Sewell, D.W. Wright, Biomimetic Synthesis of Titanium Dioxide Utilizing the R5 Peptide Derived from *Cylindrotheca fusiformis*, *Chem Mater*, 18 (2006) 3108-3113.
- [45] N. Choi, L. Tan, J.-r. Jang, Y. Um, P.J. Yoo, W.S. Choe, The interplay of peptide sequence and local structure in TiO<sub>2</sub> biomineralization, *J Inorg Biochem*, 115 (2012) 20-27.
- [46] Z. Tong, D. Yang, T. Xiao, Y. Tian, Z. Jiang, Biomimetic fabrication of g-C<sub>3</sub>N<sub>4</sub>/TiO<sub>2</sub> nanosheets with enhanced photocatalytic activity toward organic pollutant degradation, *Chem Eng J*, 260 (2015) 117-125.
- [47] J.J. Jiang, C. Tsounis, L.C. Gallington, Y.F. Hu, R.W.J. Scott, J.A. Scott, N.M. Bedford, Disordered TiO<sub>x</sub>-SiO<sub>x</sub> Nanocatalysts Using Bioinspired Synthetic Routes, *Acs Appl Energ Mater*, 4 (2021) 7691-7701.
- [48] H.T. Xu, H.J. Zhang, Y. Ouyang, L. Liu, Y. Wang, Two-dimensional hierarchical porous carbon composites derived from corn stalks for electrode materials with high performance, *Electrochimica Acta*, 214 (2016) 119-128.
- [49] C. Liu, D. Yang, Y. Jiao, Y. Tian, Y. Wang, Z. Jiang, Biomimetic synthesis of TiO<sub>2</sub>-SiO<sub>2</sub>-Ag nanocomposites with enhanced visible-light photocatalytic activity, *ACS Appl Mater Interfaces*, 5 (2013) 3824-3832.
- [50] B.A. Krajina, A.C. Proctor, A.P. Schoen, A.J. Spakowitz, S.C. Heilshorn, Biotemplated synthesis of inorganic materials: An emerging paradigm for nanomaterial synthesis inspired by nature, *Progress in Materials Science*, 91 (2018) 1-23.

- [51] O. Durupthy, L.P.H. Jeurgens, J. Bill, Biomimetic formation of Titania Thin Films: Effect of Amino Acids on the Deposition Process, *Acs Appl Mater Inter*, 3 (2011) 1624-1632.
- [52] J. Dou, Y. Li, F. Xie, X. Ding, M. Wei, Metal–Organic Framework Derived Hierarchical Porous Anatase TiO<sub>2</sub> as a Photoanode for Dye-Sensitized Solar Cell, *Crystal Growth & Design*, 16 (2015) 121-125.
- [53] S.M. Alardhi, T.M. Albayati, J.M. Alrubaye, A hybrid adsorption membrane process for removal of dye from synthetic and actual wastewater, *Chem Eng Process*, 157 (2020).
- [54] L. Goswami, A. Kushwaha, S.R. Kafle, B.S. Kim, Surface Modification of Biochar for Dye Removal from Wastewater, *Catalysts*, 12 (2022).
- [55] W.A. Shaikh, A. Kumar, S. Chakraborty, M. Naushad, R. Ul Islam, T. Bhattacharya, S. Datta, Removal of toxic dye from dye-laden wastewater using a new nanocomposite material: Isotherm, kinetics and adsorption mechanism (vol 308, 136413, 2022), *Chemosphere*, 308 (2022).
- [56] D.A. Erdogan, T. Solouki, E. Ozensoy, A versatile bio-inspired material platform for catalytic applications: micron-sized “buckyball-shaped” TiO<sub>2</sub> structures, *RSC Advances*, 5 (2015) 47174-47182.
- [57] D. Yang, X. Zhao, Y. Chen, W. Wang, Z. Zhou, Z. Zhao, Z. Jiang, Synthesis of g-C<sub>3</sub>N<sub>4</sub> Nanosheet/TiO<sub>2</sub> Heterojunctions Inspired by Bioadhesion and Biomineralization Mechanism, *Industrial & Engineering Chemistry Research*, 58 (2019) 5516-5525.
- [58] J.K. Kim, J.R. Jang, M.S. Salman, L.H. Tan, C.H. Nam, P.J. Yoo, W.S. Choe, Harnessing designer biotemplates for biomineralization of TiO<sub>2</sub> with tunable photocatalytic activity, *Ceramics International*, 45 (2019) 6467-6476.
- [59] K.S. Liu, M.Y. Cao, A. Fujishima, L. Jiang, Bio-Inspired Titanium Dioxide Materials with Special Wettability and Their Applications, *Chemical Reviews*, 114 (2014) 10044-10094.
- [60] Y.K. Lai, Y.X. Tang, J.Y. Huang, F. Pan, Z. Chen, K.Q. Zhang, H. Fuchs, L.F. Chi, Bioinspired TiO<sub>2</sub> Nanostructure Films with Special Wettability and Adhesion for Droplets Manipulation and Patterning, *Sci Rep-Uk*, 3 (2013).
- [61] S. Jafari, B. Mahyad, H. Hashemzadeh, S. Janfaza, T. Gholikhani, L. Tayebi, Biomedical Applications of TiO<sub>2</sub> Nanostructures: Recent Advances, *Int J Nanomed*, 15 (2020) 3447-3470.
- [62] X.C. Wang, K. Maeda, A. Thomas, K. Takanabe, G. Xin, J.M. Carlsson, K. Domen, M. Antonietti, A metal-free polymeric photocatalyst for hydrogen production from water under visible light, *Nat Mater*, 8 (2009) 76-80.
- [63] P. Niu, L. Zhang, G. Liu, H.-M. Cheng, Graphene-Like Carbon Nitride Nanosheets for Improved Photocatalytic Activities, *Advanced Functional Materials*, 22 (2012) 4763-4770.
- [64] S. Yang, Y. Gong, J. Zhang, L. Zhan, L. Ma, Z. Fang, R. Vajtai, X. Wang, P.M. Ajayan, Exfoliated graphitic carbon nitride nanosheets as efficient catalysts for hydrogen evolution under visible light, *Adv Mater*, 25 (2013) 2452-2456.
- [65] H.J. Li, B.W. Sun, L. Sui, D.J. Qian, M. Chen, Preparation of water-dispersible porous g-C<sub>3</sub>N<sub>4</sub> with improved photocatalytic activity by chemical oxidation, *Phys Chem Chem Phys*, 17 (2015) 3309-3315.
- [66] R. Acharya, K. Parida, A review on TiO<sub>2</sub>/g-C<sub>3</sub>N<sub>4</sub> visible-light- responsive photocatalysts for sustainable energy generation and environmental remediation, *Journal of Environmental Chemical Engineering*, 8 (2020).
- [67] D. Yang, Y. Zhang, S. Zhang, Y. Cheng, Y. Wu, Z. Cai, X. Wang, J. Shi, Z. Jiang, Coordination between Electron Transfer and Molecule Diffusion through a Bioinspired Amorphous Titania Nanoshell for Photocatalytic Nicotinamide Cofactor Regeneration, *ACS Catalysis*, 9 (2019) 11492-11501.
- [68] H. Zhang, J. Liu, L. Jiang, Photocatalytic hydrogen evolution based on carbon nitride and organic semiconductors, *Nanotechnology*, 33 (2022).

- [69] J.L. Li, X. Bai, X. Rao, Y.P. Zhang, Heterojunction of WO<sub>3</sub> Particle and g-C<sub>3</sub>N<sub>4</sub> Nanowire for Enhanced Photocatalytic Hydrogen Evolution, *Chemistryselect*, 6 (2021) 8182-8187.
- [70] B.B. Wang, H.T. Yu, X. Quan, S. Chen, Ultra-thin g-C<sub>3</sub>N<sub>4</sub> nanosheets wrapped silicon nanowire array for improved chemical stability and enhanced photoresponse, *Mater Res Bull*, 59 (2014) 179-184.
- [71] B. Yang, Z.W. Wang, J.J. Zhao, X.Y. Sun, R.J. Wang, G.F. Liao, X. Jia, 1D/2D carbon-doped nanowire/ultra-thin nanosheet g-C<sub>3</sub>N<sub>4</sub> isotype heterojunction for effective and durable photocatalytic H<sub>2</sub> evolution, *Int J Hydrogen Energ*, 46 (2021) 25436-25447.
- [72] H. Mohtasham, B. Gholipour, S. Rostamnia, A. Ghiasi-Moaser, M. Farajzadeh, N. Nouruzi, H.W. Jang, R.S. Varma, M. Shokouhimehr, Hydrothermally exfoliated P-doped g-C<sub>3</sub>N<sub>4</sub> decorated with gold nanorods for highly efficient reduction of 4-nitrophenol, *Colloid Surface A*, 614 (2021).
- [73] Y.H. Jiang, F. Li, Y. Liu, Y.Z. Hong, P.P. Liu, L. Ni, Construction of TiO<sub>2</sub> hollow nanosphere/g-C<sub>3</sub>N<sub>4</sub> composites with superior visible-light photocatalytic activity and mechanism insight, *J Ind Eng Chem*, 41 (2016) 130-140.
- [74] Y. Qian, H. Lai, J. Ma, G. Deng, B. Long, T. Song, L. Liu, X. Wang, Y. Tong, Molten salt synthesis of KCl-preintercalated C(3)N(4) nanosheets with abundant pyridinic-N as a superior anode with 10 K cycles in lithium ion battery, *J Colloid Interface Sci*, 606 (2022) 537-543.
- [75] Y. Wang, S. Shen, Progress and Prospects of Non-Metal Doped Graphitic Carbon Nitride for Improved Photocatalytic Performances, *Acta Physico-Chimica Sinica*, 36 (2020) 1905080-1905080.
- [76] Z.D. Wei, J.Y. Liu, W.J. Fang, W.Q. Guo, Y. Zhu, M.Q. Xu, Z. Jiang, W.F. Shangguan, Photocatalytic hydrogen energy evolution from antibiotic wastewater via metallic bi nanosphere doped g-C<sub>3</sub>N<sub>4</sub>: performances and mechanisms, *Catalysis Science & Technology*, 9 (2019) 5279-5291.
- [77] Z.Y. Zhou, D. Yang, W.J. Wang, Y. Chen, Z.F. Zhao, K. An, H.J. Ren, Z.Y. Jiang, Bioinspired Construction of g-C<sub>3</sub>N<sub>4</sub> Nanolayers on a Carbonized Polydopamine Nanosphere Surface with Excellent Photocatalytic Performance, *Industrial & Engineering Chemistry Research*, 59 (2020) 12389-12398.
- [78] W.J. Wang, J.C. Yu, Z.R. Shen, D.K.L. Chan, T. Gu, g-C<sub>3</sub>N<sub>4</sub> quantum dots: direct synthesis, upconversion properties and photocatalytic application, *Chem Commun*, 50 (2014) 10148-10150.
- [79] Y.P. Wang, Y.K. Li, J.L. Zhao, J.S. Wang, Z.J. Li, g-C<sub>3</sub>N<sub>4</sub>/B doped g-C<sub>3</sub>N<sub>4</sub> quantum dots heterojunction photocatalysts for hydrogen evolution under visible light, *Int J Hydrogen Energ*, 44 (2019) 618-628.
- [80] Q.J. Fan, J.J. Liu, Y.C. Yu, S.L. Zuo, B.S. Li, A simple fabrication for sulfur doped graphitic carbon nitride porous rods with excellent photocatalytic activity degrading RhB dye, *Applied Surface Science*, 391 (2017) 360-368.
- [81] F. He, G. Chen, J.W. Miao, Z.X. Wang, D.M. Su, S. Liu, W.Z. Cai, L.P. Zhang, S. Hao, B. Liu, Sulfur-Mediated Self-Templating Synthesis of Tapered C-PAN/g-C<sub>3</sub>N<sub>4</sub> Composite Nanotubes toward Efficient Photocatalytic H<sub>2</sub> Evolution, *Acs Energy Lett*, 1 (2016) 969-975.
- [82] L. Shi, T. Wang, H.B. Zhang, K. Chang, J.H. Ye, Electrostatic Self-Assembly of Nanosized Carbon Nitride Nanosheet onto a Zirconium Metal-Organic Framework for Enhanced Photocatalytic CO<sub>2</sub> Reduction, *Advanced Functional Materials*, 25 (2015) 5360-5367.
- [83] L. Zhou, J.R. Feng, B.C. Qiu, Y. Zhou, J.Y. Lei, M.Y. Xing, L.Z. Wang, Y.B. Zhou, Y.D. Liu, J.L. Zhang, Ultrathin g-C<sub>3</sub>N<sub>4</sub> nanosheet with hierarchical pores and desirable energy band for highly efficient H<sub>2</sub>O<sub>2</sub> production, *Appl Catal B-Environ*, 267 (2020).
- [84] D.D. Zheng, C.Y. Pang, Y.X. Liu, X.C. Wang, Shell-engineering of hollow g-C<sub>3</sub>N<sub>4</sub> nanospheres via copolymerization for photocatalytic hydrogen evolution, *Chem Commun*, 51 (2015) 9706-9709.
- [85] B. Lin, G.D. Yang, L.Z. Wang, Stacking-Layer-Number Dependence of Water Adsorption in 3D

- Ordered Close-Packed g-C<sub>3</sub>N<sub>4</sub> Nanosphere Arrays for Photocatalytic Hydrogen Evolution, *Angew Chem Int Edit*, 58 (2019) 4587-4591.
- [86] B. Zhou, M. Waqas, B. Yang, K. Xiao, S.Y. Wang, C.Z. Zhu, J.Y. Li, J.M. Zhang, Convenient one-step fabrication and morphology evolution of thin-shelled honeycomb-like structured g-C<sub>3</sub>N<sub>4</sub> to significantly enhance photocatalytic hydrogen evolution, *Applied Surface Science*, 506 (2020).
- [87] H.Y. Yang, Y.M. Zhou, Y.Y. Wang, S.C. Hu, B.B. Wang, Q. Liao, H.F. Li, J.H. Bao, G.Y. Ge, S.K. Jia, Three-dimensional flower-like phosphorus-doped g-C<sub>3</sub>N<sub>4</sub> with a high surface area for visible-light photocatalytic hydrogen evolution, *Journal of Materials Chemistry A*, 6 (2018) 16485-16494.
- [88] Y. Zhang, L.L. Wu, X.Y. Zhao, Y.N. Zhao, H.Q. Tan, X. Zhao, Y.Y. Ma, Z. Zhao, S.Y. Song, Y.H. Wang, Y.G. Li, Leaf-Mosaic-Inspired Vine-Like Graphitic Carbon Nitride Showing High Light Absorption and Efficient Photocatalytic Hydrogen Evolution, *Advanced Energy Materials*, 8 (2018).
- [89] B. Lin, H. An, X.Q. Yan, T.X. Zhang, J.J. Wei, G.D. Yang, Fish-scale structured g-C<sub>3</sub>N<sub>4</sub> nanosheet with unusual spatial electron transfer property for high-efficiency photocatalytic hydrogen evolution, *Appl Catal B-Environ*, 210 (2017) 173-183.
- [90] C.H. Choi, L.H. Lin, S. Gim, S. Lee, H. Kim, X.C. Wang, W. Choi, Polymeric Carbon Nitride with Localized Aluminum Coordination Sites as a Durable and Efficient Photocatalyst for Visible Light Utilization, *Acs Catalysis*, 8 (2018) 4241-4256.
- [91] Y. Ishida, L. Chabanne, M. Antonietti, M. Shalom, Morphology Control and Photocatalysis Enhancement by the One-Pot Synthesis of Carbon Nitride from Preorganized Hydrogen-Bonded Supramolecular Precursors, *Langmuir*, 30 (2014) 447-451.
- [92] D. Cruz, J.G. Cerrillo, B. Kumru, N. Li, J.D. Perea, B.V.K.J. Schmidt, I. Lauermaun, C.J. Brabec, M. Antonietti, Influence of Thiazole-Modified Carbon Nitride Nanosheets with Feasible Electronic Properties on Inverted Perovskite Solar Cells, *Journal of the American Chemical Society*, 141 (2019) 12322-12328.
- [93] Y. Zheng, L.H. Lin, X.J. Ye, F.S. Guo, X.C. Wang, Helical Graphitic Carbon Nitrides with Photocatalytic and Optical Activities, *Angew Chem Int Edit*, 53 (2014) 11926-11930.
- [94] H.L. Li, F.P. Li, Z.Y. Wang, Y.C. Jiao, Y.Y. Liu, P. Wang, X.Y. Zhang, X.Y. Qin, Y. Dai, B.B. Huang, Fabrication of carbon bridged g-C<sub>3</sub>N<sub>4</sub> through supramolecular self-assembly for enhanced photocatalytic hydrogen evolution, *Appl Catal B-Environ*, 229 (2018) 114-120.
- [95] J.H. Huang, W.J. Cheng, Y.H. Shi, G.M. Zeng, H.B. Yu, Y.L. Gu, L.X. Shi, K.X. Yi, Honeycomb-like carbon nitride through supramolecular preorganization of monomers for high photocatalytic performance under visible light irradiation, *Chemosphere*, 211 (2018) 324-334.
- [96] J.D. Xiao, Y.B. Xie, F. Nawaz, Y.X. Wang, P.H. Du, H.B. Cao, Dramatic coupling of visible light with ozone on honeycomb-like porous g-C<sub>3</sub>N<sub>4</sub> towards superior oxidation of water pollutants, *Appl Catal B-Environ*, 183 (2016) 417-425.
- [97] M.H. Wu, L. Li, Y.C. Xue, G. Xu, L. Tang, N. Liu, W.Y. Huang, Fabrication of ternary GO/g-C<sub>3</sub>N<sub>4</sub>/MoS<sub>2</sub> flower-like heterojunctions with enhanced photocatalytic activity for water remediation, *Appl Catal B-Environ*, 228 (2018) 103-112.
- [98] Y.Y. Duan, X.F. Li, K.L. Lv, L. Zhao, Y. Liu, Flower-like g-C<sub>3</sub>N<sub>4</sub> assembly from holy nanosheets with nitrogen vacancies for efficient NO abatement, *Applied Surface Science*, 492 (2019) 166-176.
- [99] Z.R. Zhao, K.B. Li, T. Muhmood, M.Z. Xia, F.Y. Wang, Facile approach to synthesis the curly leaf-like Nano-sheets of g-C<sub>3</sub>N<sub>4</sub> with enhanced photocatalytic ability, *Materials Research Express*, 5 (2018).
- [100] X.F. Yang, L. Tian, X.L. Zhao, H. Tang, Q.Q. Liu, G.S. Li, Interfacial optimization of g-C<sub>3</sub>N<sub>4</sub>-based Z-scheme heterojunction toward synergistic enhancement of solar-driven photocatalytic oxygen evolution,

- Appl Catal B-Environ, 244 (2019) 240-249.
- [101] Q.H. Liang, X.J. Liu, B.B. Shao, L. Tang, Z.F. Liu, W. Zhang, S.X. Gong, Y. Liu, Q.Y. He, T. Wu, Y. Pan, S.H. Tong, Construction of fish-scale tubular carbon nitride-based heterojunction with boosting charge separation in photocatalytic tetracycline degradation and H<sub>2</sub>O<sub>2</sub> production, *Chem Eng J*, 426 (2021).
- [102] P. Yang, J.C. Wang, G.Z. Yue, R.Z. Yang, P.X. Zhao, L.J. Yang, X.C. Zhao, D. Astruc, Constructing mesoporous g-C<sub>3</sub>N<sub>4</sub>/ZnO nanosheets catalyst for enhanced visible-light driven photocatalytic activity, *J Photoch Photobio A*, 388 (2020).
- [103] D. Yang, W.J. Wang, X.Y. Zhao, Z.Y. Zhou, H.J. Ren, Y. Chen, Z.F. Zhao, K. An, Z.Y. Jiang, Synthesis of high-efficient g-C<sub>3</sub>N<sub>4</sub>/polydopamine/CdS nanophotocatalyst based on bioinspired adhesion and chelation, *Mater Res Bull*, 131 (2020).
- [104] D. Yang, W.J. Wang, K. An, Y. Chen, Z.F. Zhao, Y.C. Gao, Z.Y. Jiang, Bioinspired construction of carbonized poly(tannic acid)/g-C<sub>3</sub>N<sub>4</sub> nanorod photocatalysts for organics degradation, *Applied Surface Science*, 562 (2021).
- [105] Y. Chen, X. Xin, D. Yang, H. Ren, Y. Gao, Z. Zhao, W. Wang, K. An, J. Tan, Z. Jiang, Pyrimidine-modified g-C<sub>3</sub>N<sub>4</sub> nanosheets for enhanced photocatalytic H<sub>2</sub> evolution, *Mater Res Bull*, 144 (2021).
- [106] B.B. Zhao, J.C. Xu, Y.P. Liu, J.J. Fan, H.G. Yu, Amino group-rich porous g-C<sub>3</sub>N<sub>4</sub> nanosheet photocatalyst: Facile oxalic acid-induced synthesis and improved H<sub>2</sub>-evolution activity, *Ceramics International*, 47 (2021) 18295-18303.
- [107] Y. Liang, N. Sun, C.J. Zang, F. Chen, 1,3,5-Benzenetriyl substituted g-C<sub>3</sub>N<sub>4</sub> for enhanced visible light photocatalytic activity, *Res Chem Intermediat*, 45 (2019) 3641-3654.
- [108] J.S. Zhang, M.W. Zhang, S. Lin, X.Z. Fu, X.C. Wang, Molecular doping of carbon nitride photocatalysts with tunable bandgap and enhanced activity, *J Catal*, 310 (2014) 24-30.
- [109] L. Ma, G. Wang, C. Jiang, H. Bao, Q. Xu, Synthesis of core-shell TiO<sub>2</sub>@g-C<sub>3</sub>N<sub>4</sub> hollow microspheres for efficient photocatalytic degradation of rhodamine B under visible light, *Applied Surface Science*, 430 (2018) 263-272.



## **CHAPTER 2. Biomineralization of TiO<sub>2</sub> by Lysozyme– Polystyrene Template for Enhanced Photocatalytic Activity**

### **2.1. Introduction**

Titania has been widely investigated because of its low cost, nontoxicity, high chemical and physical stability, and great potential for electrochemical and photocatalytic applications. The main polymorphs of TiO<sub>2</sub> are anatase, rutile, and brookite, with bandgap values ranging from 3.0 to 3.2 eV [1]. The bandgap results in only approximately 5% use of solar light for TiO<sub>2</sub> photocatalytic activation [2]. Hence, various modifications of TiO<sub>2</sub> have been studied to improve the efficiency of visible (VIS) light-driven photocatalytic performance [3]. Compared to pristine TiO<sub>2</sub>, titania doped using metal or nonmetal materials, or linking with other semiconductors have been reported to exhibit effective photocatalytic activities through improved absorbance in the VIS light range and a low recombination rate of electron–hole (e<sup>-</sup>-h<sup>+</sup>) pairs [4–10]. In addition, the photocatalytic activity of TiO<sub>2</sub> highly depends on its morphology [11–13], which can be affected by various synthesis methods, such as anodization [14], sol–gel [15,16], and hydrothermal methods [17,18]. However, conventional approaches to produce titania generally require harsh conditions and solvents, which are highly challenging from practical and environmental viewpoints.

Biomineralization is a process that is widely observed in nature, during the formation of skeletons, teeth, and shells. It can be simply described as the assembly process of inorganic minerals under the direction of organisms [19]. The use of biomaterials, such as peptides [20,21], proteins [22–24], and other biomolecules [25–28], as organic templates for the synthesis of inorganic materials is a “green” method that enables the precise design and adjustment of the morphology, crystallinity, and enhanced properties under mild conditions (i.e., neutral pH, room temperature, atmospheric pressure, and minimal addition of toxic chemicals) [29,30]. Lysozyme (LYZ) is an ideal candidate for incorporating negatively charged molecules because of its high isoelectric point (pI ~ 10.7), which allowed it to bear a

net positive charge over a broad pH range [31]. Previous studies have confirmed that LYZ is a promising biotemplate for the mineralization of inorganic materials. Luckarift *et al.* synthesized spherical amorphous-phased titania particles in the size range 10–50 nm induced by LYZ [32]. Salman *et al.* obtained TiO<sub>2</sub> hollow spheres, which exhibited excellent electrochemical properties as an anode material for lithium batteries, from LYZ templates in the presence of phosphate ions [33].

However, organic composites as templates can be undesirable because of their complex structures. For example, the linear-structured peptide hardly directs the formation of TiO<sub>2</sub>. Additionally, the *in situ* nitrogen doping content was relatively small because of the limited N content from the biotemplates [26,34]. Thus, the bioinspired crystallization process of inorganic materials with improved properties using organic templates was developed. It was reported that the cooperative interactions between inorganic and organic materials are used to control the nucleation and crystallization of inorganic substances [35]. Matsumura *et al.* demonstrated that zinc hydroxide carbonate precursors stabilized by poly(acrylic acid) (PAA) regulated the crystallization of the synthesis of a ZnO thin film, which exhibited a superior crystallographic orientation [36]. Karabacak *et al.* prepared core/shell-structured anatase templated by polystyrene (PS) colloidal particles through a sol–gel process, which exhibited high photooxidation activity [37]. Kondo *et al.* synthesized hollow TiO<sub>2</sub> with enhanced photovoltaic performance by applying PS spheres as rigid templates, followed by the pyrolysis of PS cores [38]. Hence, a protein–polymer template is promising and reliable for possible *in situ* nitrogen doping and the development of particle morphology. To synthesize the protein–polymer template, a sufficient amount of protein must be effectively adsorbed onto the surface of a polymer, according to various factors (pH, ionic strength, and protein characteristics) affecting the protein adsorption [39]. Several interactions, such as electrostatic, hydrogen bonding, and hydrophobic interactions, exist between protein and the surface of the polymer [40,41]. Thus, as the first step to synthesize the biotemplate, the protein adsorption onto the polymer surface must be optimized.

Here, we developed a novel green strategy to mineralize TiO<sub>2</sub> nanoparticles using an LYZ–PS template, where the template was formed by the passive adsorption of proteins onto PS beads. The electrostatic interaction between PS and LYZ rendered PS a promising

adsorbent for LYZ [42]. TiO<sub>2</sub> particles were successfully mineralized using the LYZ–PS template in an ambient environment. Certain variables, such as the pH and calcination temperature, were investigated during the mineralization process and compared with those for bare LYZ-induced TiO<sub>2</sub> particles. The photocatalytic activity of the TiO<sub>2</sub> particles was compared with the photodegradation of rhodamine B (RhB) under simulated solar light irradiation.

## **2.2. Experimental**

### **2.2.1. Materials**

LYZ from chicken egg white, RhB, titanium (IV) bis (ammonium lactato) dihydroxide (Ti-BALDH, a 50 wt% aqueous solution), glycine, and 4-morpholineethanesulfonic acid (MES) were purchased from Sigma-Aldrich (Kyounggi, South Korea). Tris–acetate–ethylenediaminetetraacetic acid (EDTA) (TAE) buffer (50 ×) was purchased from T&I Biotechnology (Gangwon, South Korea), and sodium hydroxide was purchased from DC Chemical Co., Ltd. (Seoul, South Korea). Plain PS beads (a 5.0% w/v aqueous suspension) with a diameter of 0.08 μm were purchased from Spherotech, Inc. (Illinois, USA). A Pierce™ BCA protein assay kit was purchased from ThermoFisher (Seoul, South Korea). All chemicals were used as received without further purification. Deionized water was used throughout the procedure.

### **2.2.2. Synthesis of template from LYZ and PS beads**

To synthesize the LYZ–PS template, the adsorption of LYZ onto the PS surface was conducted at various pH levels (5.0, 8.5, and 10.0). First, 0.2 mL of PS (5% w/v) was washed with the MES (25 mM, pH 5.0), TAE (1 ×, pH 8.5), and glycine–sodium hydroxide buffers (25 mM, pH 10.0) and resuspended in 9 mL of each buffer by vortex, followed by 30 min of sonication to achieve optimal particle suspension. LYZ solutions were prepared in the three aforementioned buffers to obtain a series concentration within a range of 50–600 mg L<sup>-1</sup>. Thereafter, each PS suspension was added into 1 mL of each LYZ solution at respective pH

levels. The mixtures of LYZ and PS were gently rotated on a mixer (SLRM-3 Intelli-Mixer, Seoulin Bioscience, Seongnam, South Korea) at 45°C for 24 h in an incubator. The LYZ–PS was collected by centrifugation (1736MGR, Gyrozen Co., Ltd., Gimpo, South Korea) at 8000 g for 30 min, and supernatants were carefully extracted. The amount of LYZ before and after adsorption was determined using the BCA protein assay kit.

### 2.2.3. Biomineralization of TiO<sub>2</sub>

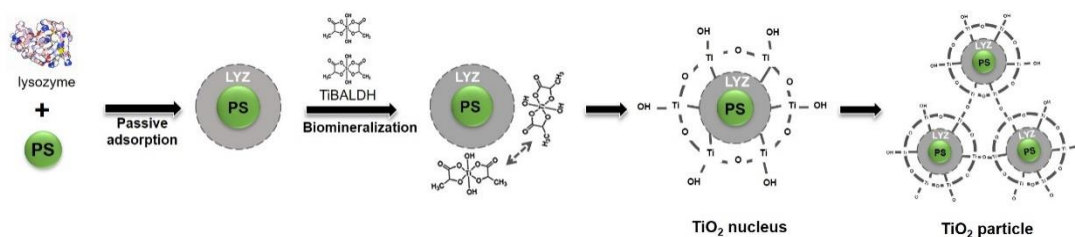


**Fig. 2.1.** Schematic of TiO<sub>2</sub> mineralization using the lysozyme (LYZ)–polystyrene (PS) template.

The LYZ–PS templates prepared at various pH levels were resuspended in water and incubated with the TiBALDH precursor using the mass ratio of 1:10 (LYZ:TiBALDH) [43]. The total volume was topped up to 10 mL using deionized water and mineralized for 24 h at room temperature. Fig. 2.1 shows the schematic of the TiO<sub>2</sub> mineralization using the LYZ–PS template. LYZ–PS–TiO<sub>2</sub> particles were collected by centrifugation at 8000 g for 15 min and were consecutively washed with ethanol and water several times. The samples were freeze-dried (FDU-2200, EYELA, Tokyo, Japan) overnight. Calcination was conducted within a range of 500°C–800°C at a ramping rate of 5°C/min for 2 h in a muffle furnace with argon flow. The LYZ–PS–TiO<sub>2</sub> particles collected were denoted as “LPT”. In comparison, LYZ-induced TiO<sub>2</sub> particles were synthesized using the same method. LYZ–TiO<sub>2</sub> was denoted as “LT”. Bare TiO<sub>2</sub> was synthesized following the same process without using PS or LYZ as the control.

#### 2.2.4. Characterization

Here, the morphologies of the samples were analyzed by field-emission scanning electron microscopy (FE-SEM; JSM-6500F, JEOL, Tokyo, Japan) and high-resolution transmission electron microscopy (TEM; JEM-2100F, JEOL). X-ray diffraction (XRD; D/MAZX 2500V/PC high-power diffractometer, Rigaku, Tokyo, Japan), conducted at a scan rate of  $2^\circ/\text{min}$ , Cu  $K\alpha$ ,  $\lambda = 1.5415 \text{ \AA}$ , was applied to analyze the crystalline structures. Raman spectra (DXR Raman spectrometer, Thermo Scientific, Seoul, South Korea) were recorded with a 532-nm excitation source. Chemical structures were verified by X-ray photoelectron spectrometry (XPS; K-Alpha, Thermo Scientific), and Fourier transform infrared (FT-IR) spectra were recorded to identify the functional groups (Thermo Scientific). The content of  $\text{TiO}_2$  on the LYZ-PS template was obtained by thermogravimetric analysis (TGA) between 25 and  $800^\circ\text{C}$  at a heating rate of  $10^\circ\text{C}/\text{min}$  (TGA Q50, TA Instruments, New Castle, DE, USA). Optical properties were verified using a photoluminescence (PL) spectrometer with an excitation wavelength of 300 nm (Agilent Technologies, Santa Clara, CA, USA), and ultraviolet (UV)-VIS diffuse reflectance (SPECORD 210 PLUS spectroscope, AnalytikJena, Jena, Germany). Zeta potential measurements were performed using a zeta potential analyzer (Zetasizer Nano ZS, Malvern Panalytical, Malvern, UK) to examine the surface charge during passive adsorption between LYZ and PS.

#### 2.2.5. Photocatalytic activity

The photocatalytic activity of the biomineralized  $\text{TiO}_2$  was compared with the degradation of RhB. First, 10 mg of the as-prepared particles was mixed with 50 mL of RhB solution (10 ppm) on a magnetic stirrer. Adsorption/desorption equilibrium was attained after stirring the mixture in the dark for 120 min. The mixture was irradiated under a solar simulator with a 140-W xenon lamp and UV cut-off/correction filter (Oriel Sol1A™ Class ABB system) for 180 min. Thereafter, 1 mL of the solution was extracted at 20-min intervals, and the supernatant was obtained using a polytetrafluoroethylene (PTFE) syringe filter (Whatman™, GmbH, Dassel, Germany). The concentration of RhB before and after irradiation was determined at 553 nm by UV-VIS spectroscopy.

## 2.3. Results and discussion

### 2.3.1. Adsorption of LYZ onto PS beads

The LYZ from chicken egg white is a globular-shaped cationic polypeptide with an average diameter of 4 nm in the native structure [43]. The PS beads applied in this study were negatively charged nonfunctionalized microbeads with a diameter of 0.08  $\mu\text{m}$ . The amount of LYZ adsorbed per gram of the PS beads was calculated and plotted against the LYZ concentration and adsorption time. As shown in Fig. 2.2a, the LYZ adsorption capacity reached a plateau at a specific point despite the increase in the initial concentration. Although the maximum adsorption capacities were 4.35 and 3.96  $\text{mg}/\text{m}^2$  at pH levels of 8.5 and 10.0, respectively, the capacity decreased to 1.26  $\text{mg}/\text{m}^2$  at a pH of 5.0. The adsorption was rapid in the first hour and gradually increased until it reached the maximum capacity after 24 h (Fig. 2.2b).

To characterize the adsorption behavior, isotherm models such as Langmuir and Freundlich were employed. The Langmuir isotherm assumed the monolayered adsorption of molecules onto the adsorbent, owing to the limited number of active sites and the inadequate interaction between adsorbed molecules. The linear form of the Langmuir isotherm is expressed in Equation (2-1) as follows:

$$\frac{C_e}{q_e} = \frac{C_e}{q_{\max}} + \frac{1}{q_{\max}K_L} \quad 2 - 1$$

Where  $q_e$  ( $\text{mg g}^{-1}$ ) is the amount of LYZ adsorbed onto the PS,  $C_e$  ( $\text{mg L}^{-1}$ ) is the equilibrium concentration of LYZ after adsorption,  $q_{\max}$  ( $\text{mg g}^{-1}$ ) is the maximum specific uptake of LYZ, and  $K_L$  ( $\text{L mg}^{-1}$ ) is the Langmuir isotherm constant (ratio of adsorption/desorption rates). In addition,  $q_{\max}$  and  $K_L$  were calculated from the linear fitting plot.

The Freundlich isotherm model assumed that the concentration of adsorbed molecules increased with an increase in the concentration of the initial molecules. We observed an interaction between the adsorbed molecules [34]. The Freundlich linear model is given as

Equation (2-2):

$$\ln q_e = \ln K_f + \frac{1}{n} \ln C_e \quad 2 - 2$$

where  $K_f$  and  $n$  are the Freundlich constants that affect the adsorption capacity and intensity in the adsorption process, respectively. The values of  $K_f$  and  $n$  were calculated from the intercept and slope of the plot. Large values of  $K_f$  and  $n$  refer to the high adsorption capacity [44].

The linear Langmuir and Freundlich isotherms for the LYZ and PS adsorption at different pH levels were plotted (Fig. 2.2c–d). The fitting parameters were calculated and are listed in Table 2.1. The correlation coefficient values ( $R^2$ ) showed that the adsorption of LYZ on PS fit better with the Langmuir model, and its observed correlation coefficients were 0.99755, 0.99702, and 0.99853 at pH levels of 5.0, 8.5, and 10.0, respectively. The critical characteristic called the separation factor ( $R_L$ ) of the Langmuir isotherm can be defined as follows:

$$R_L = \frac{1}{1 + C_0 K_L} \quad 2 - 3$$

Where  $K_L$  ( $L \text{ mg}^{-1}$ ) is the Langmuir constant and  $C_0$  ( $\text{mg L}^{-1}$ ) is the initial concentration of lysozyme (LYZ). The  $R_L$  value is studied as a reliable indicator for different types of adsorptions: irreversible ( $R_L = 0$ ), linear ( $R_L = 1$ ), favorable ( $0 < R_L < 1$ ), or unfavorable ( $R_L > 1$ ).

The separation factor values ( $R_L$ ) were between 0 and 1 for all the samples (Table 2.2). Therefore, the adsorption of LYZ onto PS was practically a favorable monolayered distribution. The maximum amount of LYZ occupying the surface of 10 mg PS ( $d = 0.08 \mu\text{m}$ ) was  $313.5 \text{ mg g}^{-1}$  at a pH of 8.5, which virtually correlated with the theoretical calculation provided by the bead manufacturer. (Equation 2-4,  $S = 285.7 \text{ mg g}^{-1}$ ). The amount of LYZ adsorbed was minimally reduced at a pH of 10.0 ( $284.1 \text{ mg g}^{-1}$ ); however, it significantly decreased at a pH of 5.0 ( $101.0 \text{ mg g}^{-1}$ ).

$$S = \left(\frac{6}{\rho D}\right) (C) \quad 2 - 4$$

Where,

$S$  = amount of protein required to achieve surface saturation (mg protein/g of microspheres).

$C$  = capacity of the microsphere surface for a given protein (varied depending on the size and molecule to be coupled, mg protein/m<sup>2</sup> polymer surface. For the LYZ in this study,  $C$  was estimated as 4 mg/m<sup>2</sup>).

$\frac{6}{\rho D}$  = surface area/mass (m<sup>2</sup>/g) for microspheres of a given diameter ( $\rho$  = density of microspheres, which was 1.05 g/cm<sup>3</sup> for polystyrene (PS)).

$D$  = diameter of microspheres (in microns).

To explain this, the zeta potentials of the bare PS, LYZ, and LYZ-PS templates were analyzed (Fig. 2.3). The bare PS particles remained negatively charged throughout the entire pH range. The zeta potential of LYZ became negative above a pH corresponding to the pI (9.8) of LYZ. Thus, below a pH of 9.8, the negatively charged PS particles can attract positively charged LYZ by electrostatic complexation [31]. However, the significant decrease in adsorption at a pH of 5.0 could have originated from the electrostatic repulsion between each positively charged LYZ molecule. The high zeta potential of LYZ at a low pH indicates good stability, whereas the water bulk layer and electrical double layer around the protein molecules will be disrupted at a pH level around the pI of the protein [45]. Thus, at a pH = pI, small conformations of protein molecules could be packed onto the polymer surface with a high density. This could be why the maximum adsorption was observed near the pI values of the protein [41,46,47]. Thus, the mineralization experiment used in this study was conducted at a pH of 8.5.



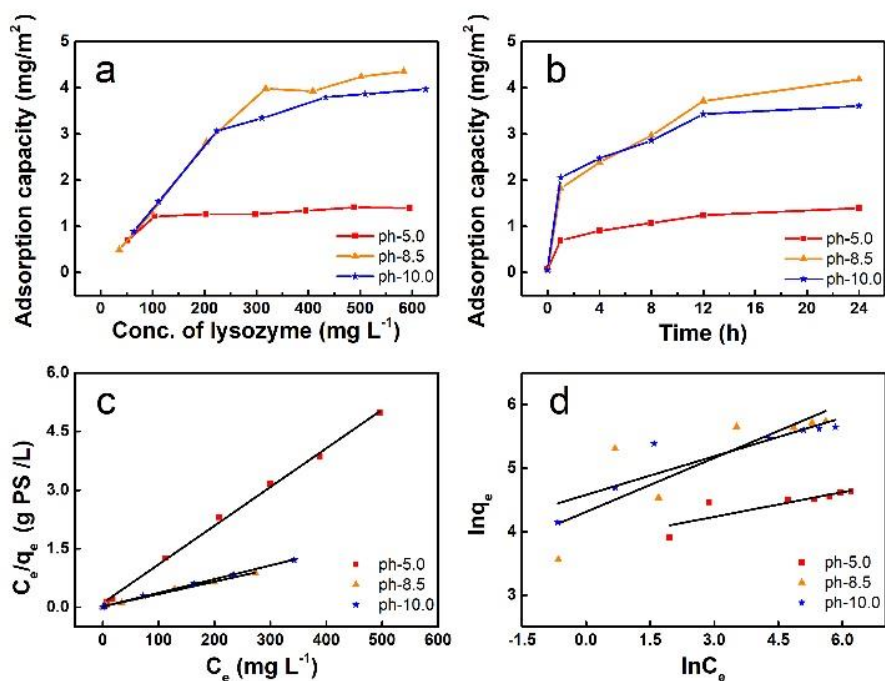


**Fig. 2.2.** Characteristics of lysozyme (LYZ) adsorption onto polystyrene (PS) beads during the synthesis of the LYZ–PS template. (a) Effect of initial LYZ dose on the adsorption capacity of PS at different pH levels and (b) effect of adsorption time at different pH levels (LYZ concentration = 300 mg L<sup>-1</sup>). (c) Linear Langmuir isotherm and (d) linear Freundlich isotherm.

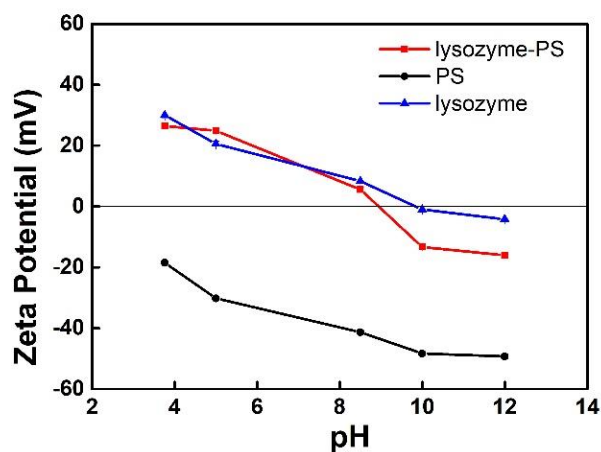


**Fig. 2.3.** Zeta potential analysis of ▲ lysozyme (LYZ), ● polystyrene (PS), and ■ LYZ–PS composites.

**Table 2.1.** Langmuir and Freundlich parameters for lysozyme on PS beads.

pH	Langmuir			Freundlich		
	$q_{\max}$ (mg g <sup>-1</sup> )	$K_L$ (L mg <sup>-1</sup> )	$R^2$	n	$K_f$	$R^2$
5.0	101.01010	0.09151	0.99755	7.71605	46.76196	0.67466
8.5	313.47962	0.14914	0.99702	3.53082	74.56491	0.65094
10.0	284.09091	0.19513	0.99853	4.93535	97.48319	0.79438

**Table 2.2.** Separation factor ( $R_L$ ) of polystyrene at various lysozyme concentrations at pH levels of 5.0, 8.5, and 10.0.

Initial concentration $C_0$ (mg/L)	$R_L$		
	pH 5.0	pH 8.5	pH 10.0
500	0.02139	0.01323	0.01015
1000	0.01081	0.00666	0.00510
2000	0.00543	0.00334	0.00256
3000	0.00363	0.00223	0.00171
4000	0.00272	0.00167	0.00128
5000	0.00218	0.00134	0.00102
6000	0.00182	0.00112	0.00085

### 2.3.2. Characteristics of synthesized TiO<sub>2</sub>

The TiO<sub>2</sub> particles obtained using the LYZ–PS template, as described in the experimental section, were characterized. The morphology of the as-prepared TiO<sub>2</sub> was analyzed by FE-SEM and TEM within a calcination temperature range of 500–800°C. As shown in Fig. 2.4a, the LPT particles were in a range of 66–80 nm prior to calcination, which was relevant to the size of the PS beads ( $d = 0.08 \mu\text{m}$ ). The LYZ layer was observed on the LYZ–PS surface, compared with the bare PS, indicating the uniform adsorption of LYZ. After the pyrolysis of PS, LPT-500 exhibited a porous structure comprising nanodonor-shaped TiO<sub>2</sub> with an internal diameter of 30 nm (Fig. 2.4b). LPT-600 and LPT-700 aggregated into clusters comprising small particles (Fig. 2. 4c–d). This might be because the donut-like TiO<sub>2</sub> shrank further into small spheres at a high calcination temperature. LPT-800 exhibited a severe aggregation with large particles (Fig. 2.4e). In contrast, the bare TiO<sub>2</sub> was amorphous, and crystallized TiO<sub>2</sub> particles with rigid edges were observed after calcination at 700°C.

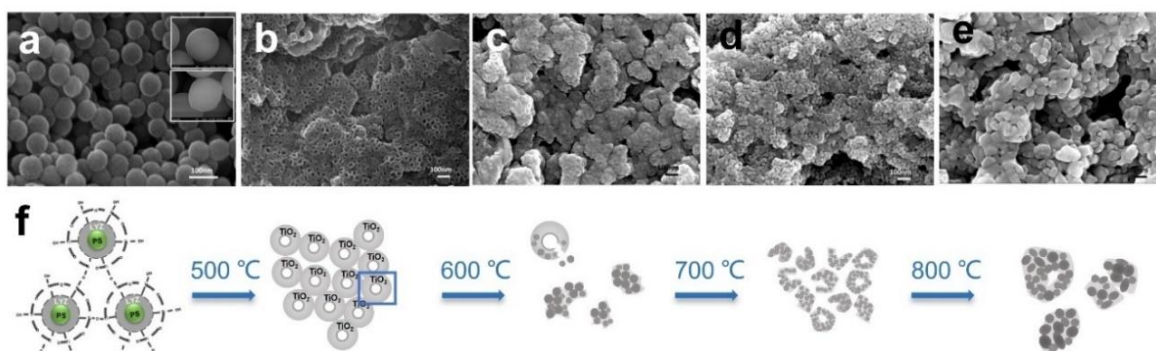


**Fig. 2.4.** Field-emission scanning electron microscopy (FE-SEM) images of lysozyme (LYZ)–polystyrene (PS)–TiO<sub>2</sub> (LPT) particles calcined under different temperatures. (a) Prior to calcination at (b) 500°C, (c) 600°C, (d) 700°C, and (e) 800°C. The insets in (a) are the bare PS (top) and LYZ–PS (bottom). (f) Corresponding illustration of the morphologies of the as-prepared TiO<sub>2</sub> differentiated by the calcination temperatures.

LT, directed only by LYZ, exhibited a network interconnected structure with a particle size range of 132–206 nm before calcination, and the network structure was broken after calcination at 700°C (Fig. 2.5). TEM images of LPT and LPT-700 were obtained for further

investigation. Fig. 2.6a–b show that the amorphous  $\text{TiO}_2$  was evenly covered on the PS surface, whereas Fig. 2.6c shows the crystallized  $\text{TiO}_2$  after calcination at  $700^\circ\text{C}$ . As illustrated in Fig. 2.4f, calcination at temperatures over  $700^\circ\text{C}$  would break down the donut-like structure into 20-nm particles with clear lattice fringes of ca. 0.35 nm for anatase (101) planes and ca. 0.32 nm for rutile (110) planes (Fig. 2.6d).

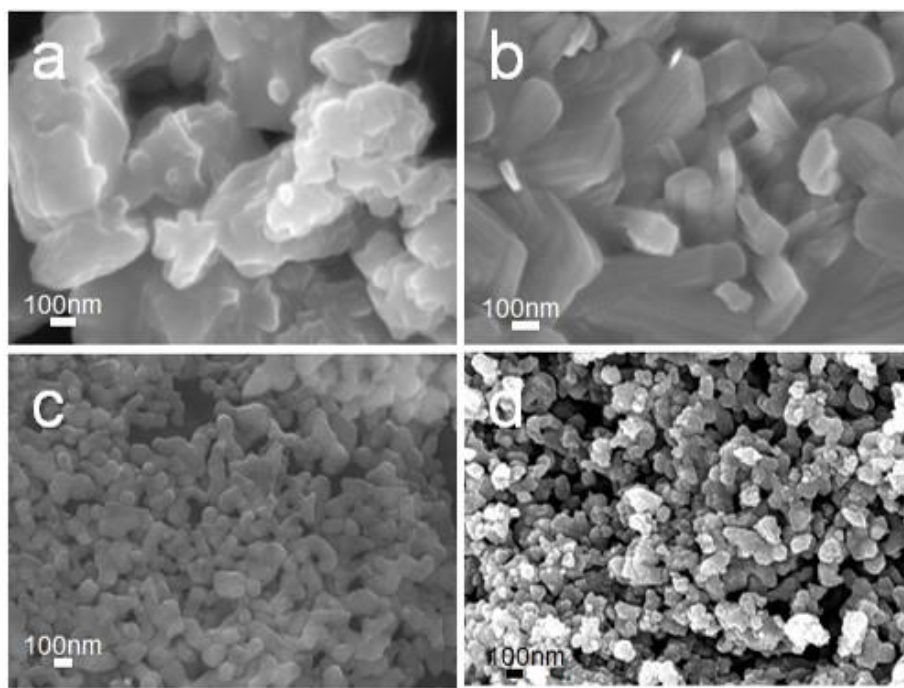


**Fig. 2.5.** Field-emission scanning electron microscopy (FE-SEM) images of the (a) bare  $\text{TiO}_2$ , (b) bare  $\text{TiO}_2$ -700, (c) LT, and (d) LT-700 particles.

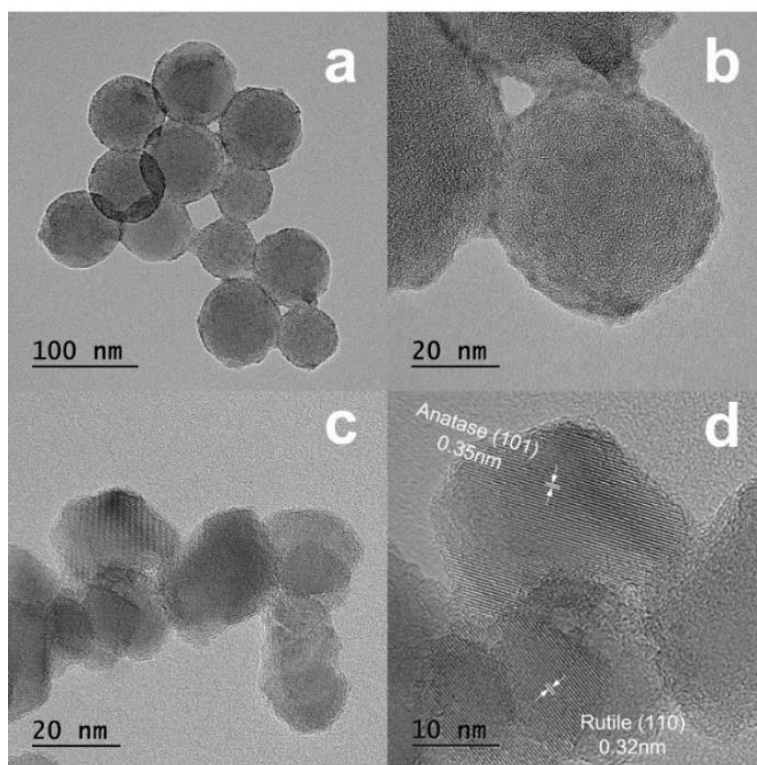


**Fig. 2.6.** Transmission electron microscopy (TEM) images of the uncalcined LPT (a, b) and LPT-700 (c, d).

The relative content of the organic template in the particles (LT, LPT) was characterized by TGA. As shown in Fig. 2.7a, the LPT samples were denoted as LPT-5.0, LPT-8.5, and LPT-10.0, according to pH levels during passive adsorption (pH 5.0, 8.5, and 10.0). Similarly, LT samples were denoted as LT-5.0, LT-8.5, and LT-10.0. The weight losses occurred within the range of 310–550 °C, indicating the decomposition of LYZ and other organic matter, including carbon and nitrogen species, of 41.6%, 55.1%, and 56.9% for LT-5.0, LT-8.5, and LT-10.0, respectively. The interaction between LYZ and TiBALDH is considered to be mainly driven by electrostatic force [49]. Thus, the amount of cationic LYZ bound to the anionic TiBALDH at a pH of 5.0 exhibited a high inorganic content (residue). Considering that LYZ carried no net charge and became unstable at its pI value, the white gel with a high degree of aggregation was observed at pH levels of 8.5 and 10.0. Hence, a small surface area of LYZ interacted with the TiBALDH precursor, explaining the extra loss of organic contents in LT-8.5 and LT-10.0. The total weight losses of the LPT samples were 99.2%, 87.0%, and 90.3% for LPT-5.0, LPT-8.5, and LPT-10.0, respectively. The lowest weight loss referred to the highest TiO<sub>2</sub> yield in

LPT-8.5, LPT-10.0 produced a slightly less amount, and LPT-5.0 produced the lowest amount. This result correlated with the passive adsorption capacity in the following order: ( $q_{\max}$  (pH 8.5) >  $q_{\max}$  (pH 10.0) >  $q_{\max}$  (pH 5.0)). Summarily, although the yield for the LYZ-induced  $\text{TiO}_2$  was the highest at a pH of 5.0, the amount of  $\text{TiO}_2$  synthesized using the LYZ–PS template (LPT) was closely related to the adsorption capacity of PS for LYZ. In addition, the bare PS and LYZ were analyzed as a control. LYZ shows weight losses occurred between 310°C and 550°C. This indicated the decomposition of LYZ and other organic matter, including carbon and nitrogen species, of 55.1% and 87.0% for LT and LPT, respectively, at a pH of 8.5. The TGA curve shows that PS was pyrolyzed at approximately 313°C in air.

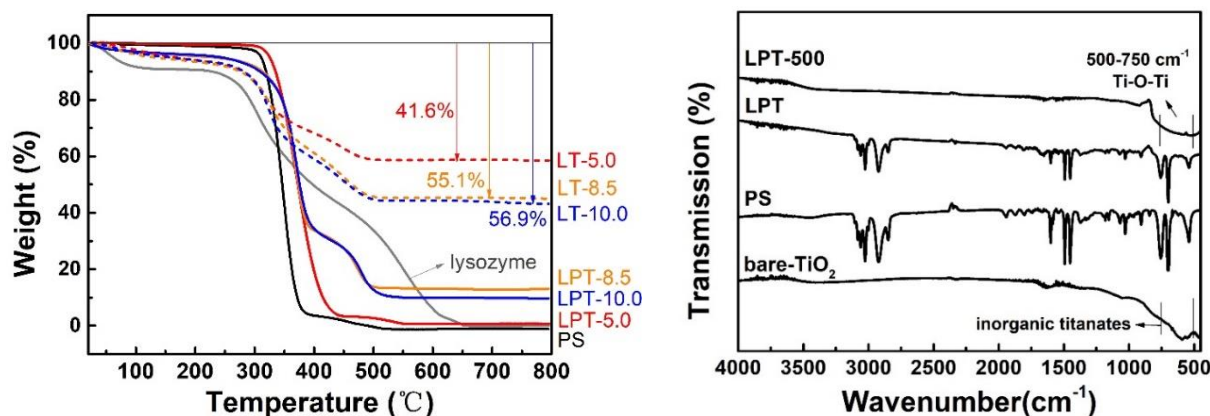


**Fig. 2.7.** (a) Thermogravimetric analysis (TGA) of pure polystyrene (PS), pure lysozyme (LYZ), LT, and LPT synthesized using the biotemplates at pH levels of 5.0, 8.5, and 10.0, respectively. (b) Fourier transform infrared (FTIR) spectra of the bare  $\text{TiO}_2$ , PS, LPT, and LPT-500.

As shown in Fig. 2.7b, typical PS bands of FTIR were observed at 1443, 1491, 1601, 2920, and 3020  $\text{cm}^{-1}$  for LPT. The absence of PS peaks after calcination confirmed the complete pyrolysis of PS. A band ranging from 500 to 750  $\text{cm}^{-1}$  for Ti–O–Ti was observed for the bare  $\text{TiO}_2$ , LPT (overlaid by PS peaks), and LPT-500. As described, the higher percentage of organic composites in LPT than in LP originated from the addition of the PS templates. The amount of LPT produced was closely related to the adsorption capacity of PS for LYZ; hence, the amount of LYZ adsorbed onto PS must be developed to further increase LPT production.



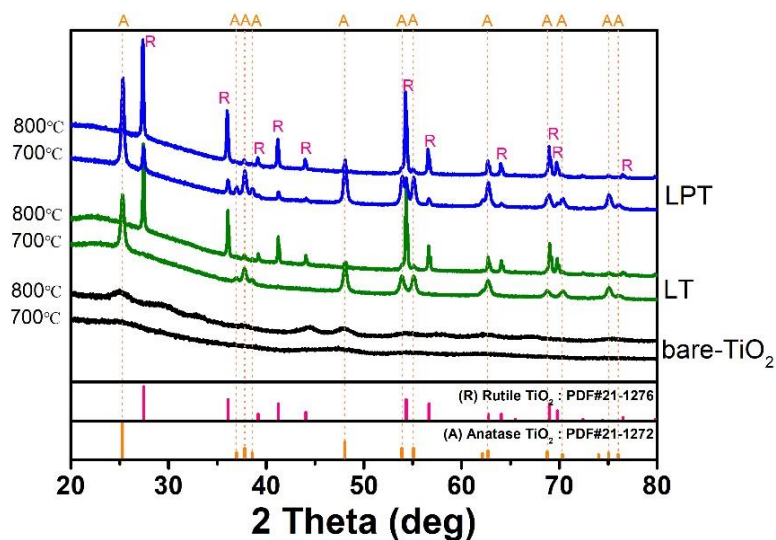


**Fig. 2.8.** X-ray diffraction (XRD) analysis of the bare TiO<sub>2</sub>, LPT, and LT particles (A, anatase; R, rutile).

The crystalline phases of TiO<sub>2</sub> calcined at different temperatures were characterized by XRD. Previous studies have reported that the transition in crystalline phases occurred with an increase in temperature. Generally, biomaterialized titania is amorphous at room temperature. The anatase phase was formed at approximately 500°C and tended to be transformed into the rutile phase at 700°C [32,33]. Here, the amorphous phase was observed in the uncalcined LPT and LT (not shown). As shown in Fig. 2.8, the mixed anatase/rutile phase was observed at 700°C and 800°C for LPT and LT, respectively. Anatase peaks were observed at 25.3° (101), 37.7° (004), 48.1° (200), 53.9° (105), 54.9° (211), 62.7° (204), 68.8° (116), 70.4° (220), and 75.1° (215) for the TiO<sub>2</sub> samples. Representative peaks of rutile were observed at 27.5° (110), 36.1° (101), 41.3° (111), 54.4° (211), and 56.7° (220) for LPT at 700°C. Only a small fraction of rutile was observed at 27.5 and 41.3° for LT at 700°C. Rutile peaks became dominant, whereas anatase peaks became weak for LPT and LT at 800°C. However, the mixed anatase/rutile phase was not observed in the bare TiO<sub>2</sub>. At 700°C, the bare TiO<sub>2</sub> was dominated by anatase, whereas at 800°C, typical peaks of titanium nitride oxide at 43.8° (311) and 67.1° (422) (TiN<sub>0.6</sub>O<sub>0.4</sub>, PDF#49-1325) appeared. This was because the TiBALDH in an aqueous solution generated TiO<sub>2</sub> with NH<sub>3</sub> and Ti(lactate)<sub>3</sub> composites, and the calcination process

resulted in the formation of titanium nitride oxide [48].

The mixed-phase TiO<sub>2</sub> has been reported to improve the efficiency of charge dissociation and transformation during the photocatalytic process by the different bandgap states between anatase and rutile [49]. The grain sizes of the mixed-phase TiO<sub>2</sub> particles were calculated using the Scherrer equation and are summarized in Table 2.3. The grain sizes for anatase (101) were LT-700 (3.5 nm), LT-800 (8.2 nm), LPT-700 (4.5 nm), and LPT-800 (6.9 nm). According to the Spurr equation, LT-700 and LT-800 had ca. 99.0% and 17.3%, respectively, of the anatase phase in the mixed anatase/rutile phase. For the LPT-700 and LPT-800 particles, anatase took up 68.3% and 16.9%, respectively. Large grain growth in the 800°C samples may have resulted from particle aggregation at the high calcination temperature. Compared with LT-700, the larger grain size of LPT-700 can be explained by its slow crystallization [50]. Among the mixed-phased samples, LPT-700 had a favorable anatase/rutile ratio and a relatively small grain size with less degree of aggregation.

**Table 2.3.** Properties of LT and LPT particles in the mixed crystal phase.

Sample	Particle size (FE-SEM) (nm)	Phase and grain size (nm) <sup>a</sup>	Anatase/rutile <sup>b</sup>
LT-700	109–170	Anatase (3.5)/rutile (N/A)	99.0/1.0
LT-800	70–187	Anatase (8.2)/rutile (30.2)	17.3/82.7
LPT-700	23–38	Anatase (4.5)/rutile (16.6)	68.3/31.7
LPT-800	56–135	Anatase (6.9)/rutile (21.3)	16.9/83.1

Calculated using the Scherrer equation.

<sup>b</sup> Calculated using the Spurr equation.

Raman spectroscopy was utilized for the TiO<sub>2</sub> structural analysis (Fig. 2.9). There are six characteristic modes for anatase in the Raman spectra ( $A_{1g} + 2B_{1g} + 3E_g$ ) and five for the rutile phase ( $B_{1g} + \text{multiproton process} + E_g + A_{1g} + B_{2g}$ ) [51]. Owing to the overlap effect, only four dominant peaks of anatase were observed at 152 cm<sup>-1</sup> ( $E_g$ ), 403 cm<sup>-1</sup> ( $B_{1g}$ ), 524 cm<sup>-1</sup> ( $A_{1g}$ ), and 645 cm<sup>-1</sup> ( $E_g$ ), and two main peaks of rutile were observed at 455 cm<sup>-1</sup> ( $E_g$ ) and 618 cm<sup>-1</sup> ( $A_{1g}$ ) in the mixed-phase LPT and LT particles after calcination at 800°C. As



observed from the peak intensity, the content of the rutile phase increased with an increase in the calcination temperature. The Raman spectra correlated with the XRD results.

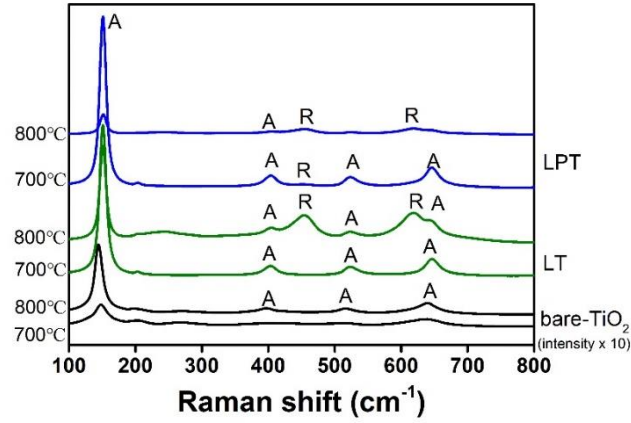


**Fig. 2.9.** Raman analysis of the (a) LPT and (b) LT particles (A, anatase; R, rutile).

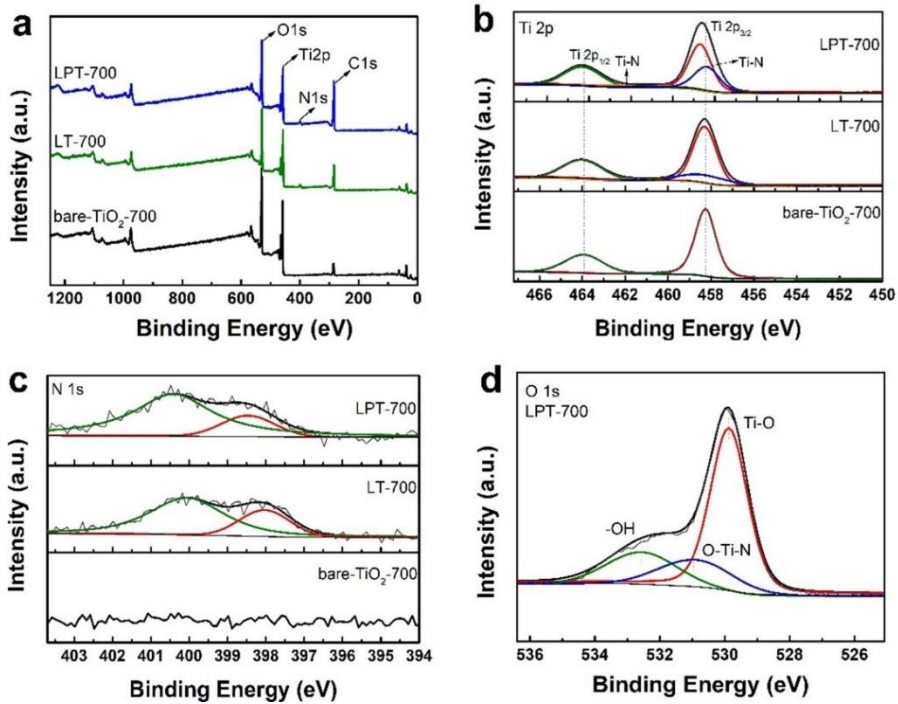


**Fig. 2.10.** (a) X-ray photoelectron spectroscopy (XPS) survey spectra of the bare TiO<sub>2</sub>-700, LT-700, and LPT-700. High-resolution spectra of (b) Ti 2p, (c) N 1s, and (d) O 1s.

The XPS survey spectra of the LPT-700, LT-700, and bare TiO<sub>2</sub>-700 (Fig. 2.10a) show that the particles comprised C, N, Ti, and O. Compared to the bare TiO<sub>2</sub>, nitrogen was observed for the LT and LPT samples. LPT had the highest component of N 1s and C 1s, which belong to the LYZ-PS biotemplate. HR Ti 2p XPS spectra (Fig. 2.10b) reveal slight shifts in the Ti 2p<sub>3/2</sub> and Ti 2p<sub>1/2</sub> peaks for the LT and LPT particles to high energy. This was because the titanium oxidation states shifted to + 4 from + 3, indicating the formation of TiO<sub>2</sub>. The additional shift in LPT might have been caused by the stronger formation of Ti-N bonding, owing to the relatively higher N% in the LPT particles (5%) than in the LT particles (3%) [52]. The Ti-N peaks were obtained at 458.4 and 460.8 eV, which illustrated that nitrogen was successfully introduced into TiO<sub>2</sub>. In addition, the N 1s spectra of LPT and LT at 700°C (Fig. 2.10c) were deconvoluted into two peaks near 398.3 and 400.1 eV that referred to substitutional (O-Ti-N) and interstitial nitrogen (Ti-O-N) doping, respectively [53]. An O-Ti-N bond was observed in the O 1s spectra of LPT-700, which confirmed the existence of nitrogen (Fig. 2.10d). The LYZ and PS from the biotemplate might accelerate the crystalline transition and preserve N in the LPT lattice at a high calcination temperature. Additionally, N dopants could act as nucleating centers in TiO<sub>2</sub> biomineralization [54]. Summarily, nitrogen from organic templates can be introduced into biomineralized TiO<sub>2</sub> and stabilize the lattice structure away from structural collapse at high temperatures.

The investigation of the absorption edge and bandgap of mixed-phase particles was conducted by UV-VIS spectroscopy. The LPT particles exhibited a broad absorption region expanded to the VIS region, compared with the bare TiO<sub>2</sub> and LT (Fig. 2.11a). Tauc plots were created to estimate the bandgap values of the photocatalysts. Fig. 2.11b shows the bandgap values of indirect energies, which were observed as approximately 2.83 and 3.11, 3.36 and 3.49, and 3.79 and 3.82 eV for the LPT, LT, and bare TiO<sub>2</sub>, respectively. Compared to the LT and bare TiO<sub>2</sub> particles, the lower bandgap values of the LPT particles resulted from the smaller particle size and nitrogen doping. In particular, the mixed anatase/rutile phase of LPT-700 is beneficial for the proficient dissociation and transportation of charges.

### 2.3.3. Photodegradation of RhB

The photocatalytic degradation of RhB using the bare TiO<sub>2</sub>, LT, and LPT particles calcined at 700°C was tested under simulated VIS irradiation (Fig. 2.13). LPT-700 exhibited the best photocatalytic activity among the samples. The results were fitted to the pseudo first-order reaction model,  $\ln \frac{C}{C_0} = -k_{app}t$ , where  $C_0$  is the concentration of RhB at adsorption-desorption equilibrium,  $C$  is the RhB concentration at reaction time ( $t$ ), and  $k_{app}$  is the apparent reaction rate constant. Table 2.4 summarizes the  $k_{app}$  and determination coefficients ( $R^2$ ) of RhB obtained from the linear plots of  $\ln(C/C_0)$  vs  $t$ . The  $k_{app}$  values increased with an increase in the calcination temperature from 500 to 700°C for the LPT particles ( $4.75\text{--}29.22 \times 10^{-3} \text{ min}^{-1}$ ) and LT particles ( $1.71\text{--}5.91 \times 10^{-3} \text{ min}^{-1}$ ). Notably, the  $k_{app}$  values of the LPT particles were significantly higher than those of the LT particles. Considering the phase transition and nitrogen content, it was reasonable for the photocatalysts of the N-doped anatase/rutile phase to exhibit better RhB degradation activities. However, the  $k_{app}$  values sharply reduced for the aggregated LPT-800 and LT-800 because the adsorption capacity of the photocatalyst for RhB dye was as important as the rate of charge transfer. Expectedly, LPT-700 exhibited the best performance of au. 98% RhB degradation within 80 min under solar light irradiation, owing to its low electron-hole pair recombination. Its  $k_{app}$  value reached  $44.80 \times 10^{-3} \text{ min}^{-1}$  resulting from a fast charge transfer that benefited from the mixed anatase/rutile phase, which exhibited a narrow bandgap of 2.83 eV. The presence of PS appeared to increase the RhB adsorption (PS and uncalcined LPT); however, their photodegradation efficiency was not high (Fig. 2.13).

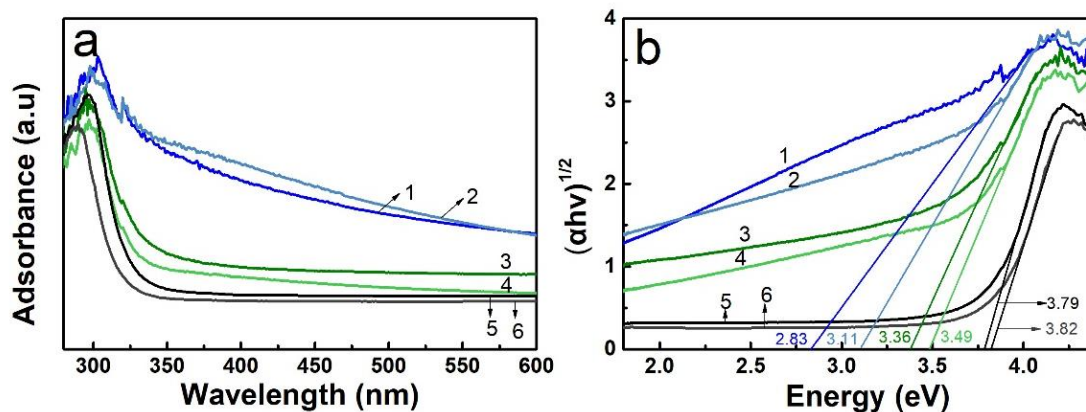


**Fig. 2.11.** (a) Ultraviolet–visible (UV–VIS) absorption spectra and (b) Tauc plots for TiO<sub>2</sub> particles. (1) LPT-700, (2) LPT-800, (3) LT-700, (4) LT-800, (5) bare TiO<sub>2</sub>-700, and (6) bare TiO<sub>2</sub>-800.

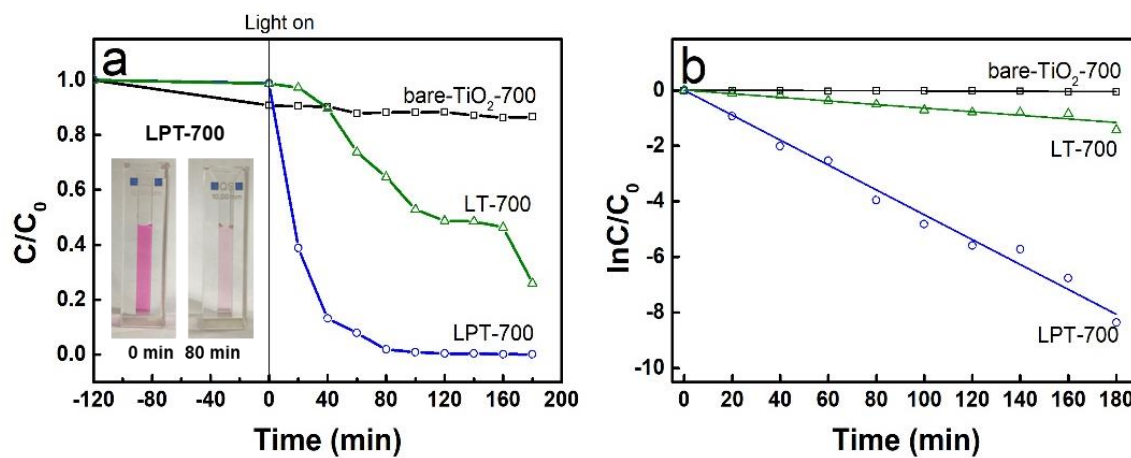


**Fig. 2.12.** Rhodamine B degradation under visible light by the calcined bare TiO<sub>2</sub>-700, LPT-700, and LP-700 particles (a,  $C/C_0$  vs.  $t$ ; b,  $\ln(C/C_0)$  vs.  $t$ ).

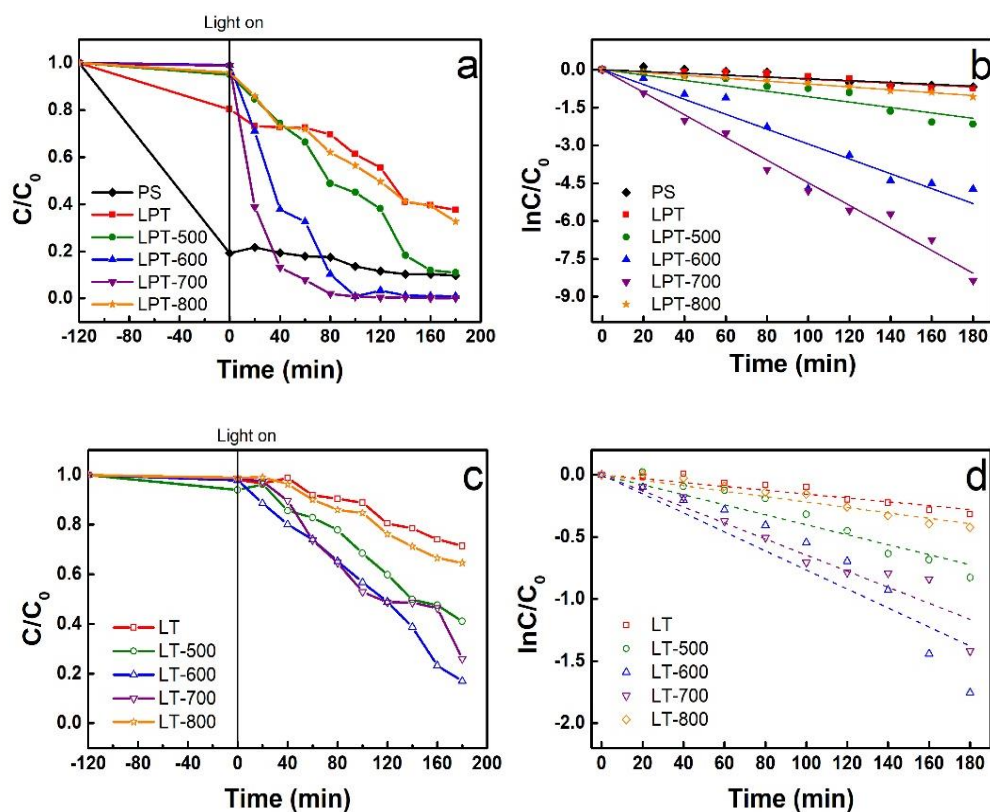


**Fig. 2.13.** Rhodamine B degradation under visible light by LPT and LP at different calcination temperatures (**a**,  $C/C_0$  vs.  $t$ ; **b**,  $\ln(C/C_0)$  vs.  $t$ ).

**Table 2.4.** Kinetic data for rhodamine B photodegradation of the as-prepared  $\text{TiO}_2$  photocatalysts.

Sample	$k_{app}$ ( $\times 10^{-3} \text{ min}^{-1}$ )	$R^2$
LT	1.55	0.94726
LT-500	4.03	0.95840
LT-600	7.66	0.93807
LT-700	6.47	0.97105
LT-800	2.19	0.96475
LPT	3.85	0.93762
LPT-500	10.73	0.95036
LPT-600	29.47	0.95516
LPT-700	44.80	0.99550
LPT-800	5.72	0.99613
PS	3.63	0.90306
Bare $\text{TiO}_2$ -700	0.29	0.95350

For the LT particles, the calcination temperature was not a crucial factor affecting the adsorption efficiencies in the dark because the morphologies of the as-prepared LT photocatalysts did not considerably change. Summarily, for an enhanced photocatalytic performance, various parameters need to be considered. First, the LYZ–PS template was beneficial because it provided more organic content, such as nitrogen, into TiO<sub>2</sub>. A high calcination temperature accelerated the transition in the mixed crystalline phase. Finally, for the particle morphologies, the photocatalyst calcined at 700°C (LPT-700) was the best candidate as a photocatalyst functioning under the VIS light range.

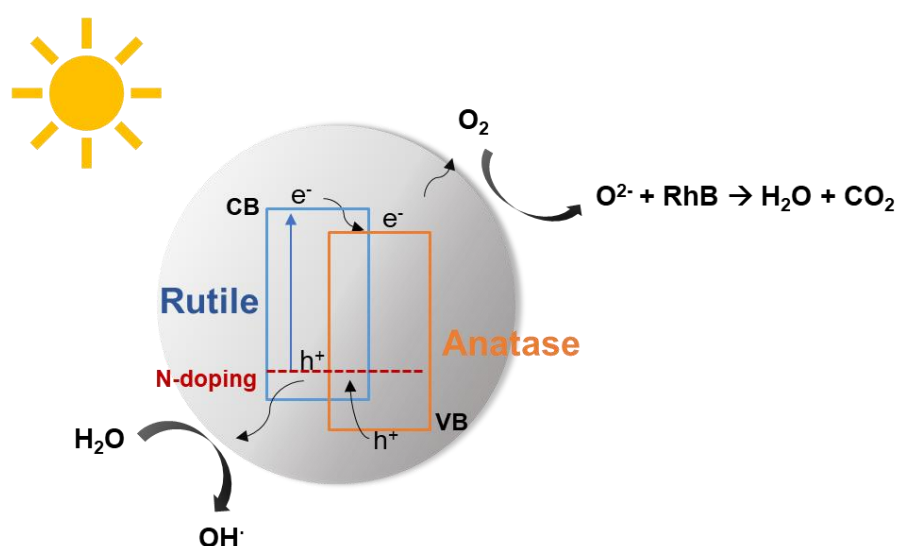


**Fig. 2.14.** Schematic illustration of the possible photocatalytic mechanism of the mixed anatase/rutile phase TiO<sub>2</sub>.

## 2.4. Summary

LYZ–PS templated TiO<sub>2</sub> (LPT) was synthesized using a simple mild-conditioned biomineralization process. Compared with the bare TiO<sub>2</sub> and LYZ-templated TiO<sub>2</sub> (LT), the presence of the LYZ–PS biotemplate tailored the particle morphologies and increased the *in situ* nitrogen dopant. Therefore, the LPT particles exhibited an improved performance in RhB photodegradation of au. 98% within 80 min under simulated solar irradiation. Summarily, the nitrogen-doped LPT nanoparticles in a mixed crystalline phase render it an enhanced

photocatalyst because of the narrow bandgap and slow recombination rate of electron–hole pairs. This study provides an insight into protein immobilization and biomineralization applications.

## Reference

- [1] Z. Jiang, X. Lv, D. Jiang, J. Xie, D. Mao, Natural leaves-assisted synthesis of nitrogen-doped, carbon-rich nanodots-sensitized, Ag-loaded anatase TiO<sub>2</sub> square nanosheets with dominant (001) facets and their enhanced catalytic applications, *J. Mater. Chem. A*. 1 (2013) 14963. <https://doi.org/10.1039/c3ta13248j>.
- [2] O. Sacco, V. Vaiano, L. Rizzo, D. Sannino, Photocatalytic activity of a visible light active structured photocatalyst developed for municipal wastewater treatment, *J. Clean. Prod.* 175 (2018) 38–49. <https://doi.org/10.1016/j.jclepro.2017.11.088>.
- [3] F. Meng, F. Lu, Z. Sun, J. Lü, A mechanism for enhanced photocatalytic activity of nano-size silver particle modified titanium dioxide thin films, *Sci. China Technol. Sci.* 53 (2010) 3027–3032. <https://doi.org/10.1007/s11431-010-4116-z>.
- [4] G. Li, C. Liao, G. Jiang, Hollow TiO<sub>2</sub> spheres with improved visible light photocatalytic activity synergistically enhanced by multi-stimulative: Morphology advantage, carbonate-doping and the induced Ti<sup>3+</sup>, *J. Environ. Sci.* 72 (2018) 153–165. <https://doi.org/10.1016/j.jes.2018.01.001>.
- [5] E.M. Rockafellow, L.K. Stewart, W.S. Jenks, Is sulfur-doped TiO<sub>2</sub> an effective visible light photocatalyst for remediation?, *Appl. Catal. B Environ.* 91 (2009) 554–562. <https://doi.org/10.1016/j.apcatb.2009.06.027>.
- [6] Y. Niu, M. Xing, J. Zhang, B. Tian, Visible light activated sulfur and iron co-doped TiO<sub>2</sub> photocatalyst for the photocatalytic degradation of phenol, *Catal. Today.* (2013). <https://doi.org/10.1016/j.cattod.2012.04.035>.
- [7] F. Wei, L. Ni, P. Cui, Preparation and characterization of N-S-codoped TiO<sub>2</sub> photocatalyst and its photocatalytic activity, *J. Hazard. Mater.* (2008). <https://doi.org/10.1016/j.jhazmat.2007.12.018>.
- [8] P.S. Basavarajappa, S.B. Patil, N. Ganganagappa, K.R. Reddy, A. V. Raghu, C.V. Reddy, Recent progress in metal-doped TiO<sub>2</sub>, non-metal doped/codoped TiO<sub>2</sub> and TiO<sub>2</sub> nanostructured hybrids for enhanced photocatalysis, *Int. J. Hydrogen Energy.* (2020). <https://doi.org/10.1016/j.ijhydene.2019.07.241>.
- [9] G. Yang, Z. Jiang, H. Shi, T. Xiao, Z. Yan, Preparation of highly visible-light active N-doped TiO<sub>2</sub> photocatalyst, *J. Mater. Chem.* (2010). <https://doi.org/10.1039/c0jm00376j>.
- [10] F. Meng, Z. Sun, A mechanism for enhanced hydrophilicity of silver nanoparticles modified TiO<sub>2</sub> thin films deposited by RF magnetron sputtering, *Appl. Surf. Sci.* 255 (2009) 6715–6720. <https://doi.org/10.1016/j.apsusc.2009.02.076>.
- [11] L. Ma, G. Wang, C. Jiang, H. Bao, Q. Xu, Synthesis of core-shell TiO<sub>2</sub>@g-C<sub>3</sub>N<sub>4</sub> hollow microspheres for efficient photocatalytic degradation of rhodamine B under visible light, *Appl. Surf. Sci.* 430 (2018) 263–272. <https://doi.org/10.1016/j.apsusc.2017.07.282>.
- [12] D.K. Hwang, J.H. Kim, K.P. Kim, S.J. Sung, Mesoporous TiO<sub>2</sub> hierarchical structures: Preparation and efficacy in solar cells, *RSC Adv.* 7 (2017) 49057–49065. <https://doi.org/10.1039/c7ra09425f>.
- [13] Z. Fan, F. Meng, M. Zhang, Z. Wu, Z. Sun, A. Li, Solvothermal synthesis of hierarchical TiO<sub>2</sub> nanostructures with tunable morphology and enhanced photocatalytic activity, *Appl. Surf. Sci.* 360 (2016) 298–305. <https://doi.org/10.1016/j.apsusc.2015.11.021>.
- [14] K. Nakata, B. Liu, Y. Ishikawa, M. Sakai, H. Saito, T. Ochiai, H. Sakai, T. Murakami, M. Abe, K. Takagi, A. Fujishima, Fabrication and photocatalytic properties of TiO<sub>2</sub> nanotube arrays modified with phosphate, *Chem. Lett.* (2011). <https://doi.org/10.1246/cl.2011.1107>.
- [15] Z. Liu, Y. Wang, W. Chu, Z. Li, C. Ge, Characteristics of doped TiO<sub>2</sub> photocatalysts for the degradation of methylene blue waste water under visible light, *J. Alloys Compd.* 501 (2010) 54–59.



- <https://doi.org/10.1016/j.jallcom.2010.04.027>.
- [16] Z. Fan, T. Wu, X. Xu, Synthesis of Reduced Grapheme Oxide as A Platform for loading  $\beta$ -NaYF<sub>4</sub>:Ho<sup>3+</sup>@TiO<sub>2</sub>Based on An Advanced Visible Light-Driven Photocatalyst, *Sci. Rep.* 7 (2017) 1–15. <https://doi.org/10.1038/s41598-017-14018-3>.
- [17] A.M. Bakhshayesh, M.R. Mohammadi, D.J. Fray, Controlling electron transport rate and recombination process of TiO<sub>2</sub> dye-sensitized solar cells by design of double-layer films with different arrangement modes, *Electrochim. Acta.* 78 (2012) 384–391. <https://doi.org/10.1016/j.electacta.2012.06.087>.
- [18] Z. Fan, F. Meng, J. Gong, H. Li, Y. Hu, D. Liu, Enhanced photocatalytic activity of hierarchical flower-like CeO<sub>2</sub>/TiO<sub>2</sub> heterostructures, *Mater. Lett.* 175 (2016) 36–39. <https://doi.org/10.1016/j.matlet.2016.03.136>.
- [19] A.L. Boskey, Biomineralization : Conflicts , Challenges , and Opportunities, *J. Cell. Biochem. Suppl.* 91 (1998) 83–91. [https://doi.org/https://doi.org/10.1002/\(SICI\)1097-4644\(1998\)72:30/31+<83::AID-JCB12>3.0.CO;2-F](https://doi.org/https://doi.org/10.1002/(SICI)1097-4644(1998)72:30/31+<83::AID-JCB12>3.0.CO;2-F).
- [20] T. Nonoyama, T. Kinoshita, M. Higuchi, K. Nagata, M. Tanaka, K. Sato, K. Kato, TiO<sub>2</sub> synthesis inspired by biomineralization: Control of morphology, crystal phase, and light-use efficiency in a single process, *J. Am. Chem. Soc.* 134 (2012) 8841–8847. <https://doi.org/10.1021/ja211347n>.
- [21] N. Choi, L. Tan, J. Jang, Y.M. Um, P.J. Yoo, W.-S. Choe, The interplay of peptide sequence and local structure in TiO<sub>2</sub> biomineralization, *J. Inorg. Biochem.* 115 (2012) 20–27.
- [22] B.A. Krajina, A.C. Proctor, A.P. Schoen, A.J. Spakowitz, S.C. Heilshorn, Biotemplated synthesis of inorganic materials: An emerging paradigm for nanomaterial synthesis inspired by nature, *Prog. Mater. Sci.* 91 (2018) 1–23. <https://doi.org/10.1016/j.pmatsci.2017.08.001>.
- [23] J. Shi, D. Yang, Z. Jiang, Y. Jiang, Y. Liang, Y. Zhu, X. Wang, H. Wang, Simultaneous size control and surface functionalization of titania nanoparticles through bioadhesion-assisted bio-inspired mineralization, *J. Nanoparticle Res.* 14 (2012) 1–13. <https://doi.org/10.1007/s11051-012-1120-1>.
- [24] H. Zeng, J. Xie, H. Xie, B.L. Su, M. Wang, H. Ping, W. Wang, H. Wang, Z. Fu, Bioprocess-inspired synthesis of hierarchically porous nitrogen-doped TiO<sub>2</sub> with high visible-light photocatalytic activity, *J. Mater. Chem. A.* 3 (2015) 19588–19596. <https://doi.org/10.1039/c5ta04649a>.
- [25] S.H. Xue, H. Xie, H. Ping, X.M. Xu, J. Li, X.Y. Yang, Z.Y. Fu, B.L. Su, Controlled synthesis of mesoporous nanostructured anatase TiO<sub>2</sub> on a genetically modified Escherichia coli surface for high reversible capacity and long-life lithium-ion batteries, *RSC Adv.* 6 (2016) 59422–59428. <https://doi.org/10.1039/c6ra09974b>.
- [26] J.K. Kim, J. ryang Jang, M.S. Salman, L. Tan, C.H. Nam, P.J. Yoo, W.S. Choe, Harnessing designer biotemplates for biomineralization of TiO<sub>2</sub> with tunable photocatalytic activity, *Ceram. Int.* 45 (2019) 6467–6476. <https://doi.org/10.1016/j.ceramint.2018.12.134>.
- [27] H. Ping, H. Xie, M. Xiang, B.-L. Su, Y. Wang, J. Zhang, F. Zhang, Z. Fu, Confined-space synthesis of nanostructured anatase, directed by genetically engineered living organisms for lithium-ion batteries, *Chem. Sci.* 7 (2016) 6330–6336. <https://doi.org/10.1039/C6SC02311H>.
- [28] L. Gao, W. Gan, Z. Qiu, G. Cao, X. Zhan, T. Qiang, J. Li, Biomorphic Carbon-Doped TiO<sub>2</sub> for Photocatalytic Gas Sensing with Continuous Detection of Persistent Volatile Organic Compounds, *ACS Appl. Nano Mater.* 1 (2018) 1766–1775. <https://doi.org/10.1021/acsanm.8b00209>.
- [29] S.K. Das, E. Marsili, A green chemical approach for the synthesis of gold nanoparticles: Characterization and mechanistic aspect, *Rev. Environ. Sci. Biotechnol.* (2010). <https://doi.org/10.1007/s11157-010-9188-5>.
- [30] J.A. Dahl, B.L.S. Maddux, J.E. Hutchison, Toward greener nanosynthesis, *Chem. Rev.* (2007).

- <https://doi.org/10.1021/cr050943k>.
- [31] T. Wu, N. Kummer, K.J. De France, S. Campioni, Z. Zeng, G. Siqueira, J. Dong, G. Nyström, Nanocellulose-lysozyme colloidal gels via electrostatic complexation, *Carbohydr. Polym.* 251 (2021) 1–9. <https://doi.org/10.1016/j.carbpol.2020.117021>.
- [32] H.R. Luckarift, M.B. Dickerson, K.H. Sandhage, J.C. Spain, Rapid, room-temperature synthesis of antibacterial bionanocomposites of lysozyme with amorphous silica or titania, *Small.* 2 (2006) 640–643. <https://doi.org/10.1002/sml.200500376>.
- [33] M.S. Salman, A.R. Park, M.J. Cha, Y. Choi, S.K. Jang, L. Tan, P.J. Yoo, W.-S. Choe, Lysozyme-Templated Meso-Macroporous Hollow TiO<sub>2</sub> for Lithium Ion Battery Anode, *ACS Appl. Nano Mater.* 1 (2018) 698–710. <https://doi.org/10.1021/acsanm.7b00164>.
- [34] Y. Xu, I.K. Yoo, Removal of lead from water solution by reusable magnetic adsorbent incorporating selective lead-binding peptide, *Appl. Sci.* 10 (2020). <https://doi.org/10.3390/APP10186418>.
- [35] A. Arakaki, K. Shimizu, M. Oda, T. Sakamoto, T. Nishimura, T. Kato, Biomineralization-inspired synthesis of functional organic/inorganic hybrid materials: Organic molecular control of self-organization of hybrids, *Org. Biomol. Chem.* 13 (2015) 974–989. <https://doi.org/10.1039/c4ob01796j>.
- [36] S. Matsumura, Y. Horiguchi, T. Nishimura, H. Sakai, T. Kato, Biomineralization-Inspired Preparation of Zinc Hydroxide Carbonate/Polymer Hybrids and Their Conversion into Zinc Oxide Thin-Film Photocatalysts, *Chem. - A Eur. J.* 22 (2016) 7094–7101. <https://doi.org/10.1002/chem.201600141>.
- [37] R.B. Karabacak, M. Erdem, S. Yurdakal, Y. Çimen, H. Türk, Facile two-step preparation of polystyrene/anatase TiO<sub>2</sub> core/shell colloidal particles and their potential use as an oxidation photocatalyst, *Mater. Chem. Phys.* 144 (2014) 498–504. <https://doi.org/10.1016/j.matchemphys.2014.01.026>.
- [38] Y. Kondo, H. Yoshikawa, K. Awaga, M. Murayama, T. Mori, K. Sunada, S. Bandow, S. Iijima, Preparation, photocatalytic activities, and dye-sensitized solar-cell performance of submicron-scale TiO<sub>2</sub> hollow spheres, *Langmuir.* 24 (2008) 547–550. <https://doi.org/10.1021/la702157r>.
- [39] M. Rabe, D. Verdes, S. Seeger, Understanding protein adsorption phenomena at solid surfaces, *Adv. Colloid Interface Sci.* 162 (2011) 87–106. <https://doi.org/10.1016/j.cis.2010.12.007>.
- [40] R.G. Chapman, E. Ostuni, S. Takayama, R.E. Holmlin, L. Yan, G.M. Whitesides, Surveying for surfaces that resist the adsorption of proteins, *J. Am. Chem. Soc.* (2000). <https://doi.org/10.1021/ja000774f>.
- [41] F. Wang, P. Liu, T. Nie, H. Wei, Z. Cui, Characterization of a polyamine microsphere and its adsorption for protein, *Int. J. Mol. Sci.* 14 (2013) 17–29. <https://doi.org/10.3390/ijms14010017>.
- [42] M. Van Der Veen, W. Norde, M.C. Stuart, Electrostatic interactions in protein adsorption probed by comparing lysozyme and succinylated lysozyme, *Colloids Surfaces B Biointerfaces.* 35 (2004) 33–40. <https://doi.org/10.1016/j.colsurfb.2004.02.005>.
- [43] J.K. Kim, J.R. Jang, N. Choi, D. Hong, C.-H.H. Nam, P.J. Yoo, J.H. Park, W.-S.S. Choe, Lysozyme-mediated biomineralization of titanium–tungsten oxide hybrid nanoparticles with high photocatalytic activity, *Chem. Commun.* 50 (2014) 12392–12395. <https://doi.org/10.1039/C4CC04820B>.
- [44] P.C. Mishra, R.K. Patel, Use of agricultural waste for the removal of nitrate-nitrogen from aqueous medium, *J. Environ. Manage.* 90 (2009) 519–522. <https://doi.org/10.1016/j.jenvman.2007.12.003>.
- [45] S.K. Pal, J. Peon, A.H. Zewail, Ultrafast surface hydration dynamics and expression of protein functionality:  $\alpha$ -chymotrypsin, *Proc. Natl. Acad. Sci. U. S. A.* 99 (2002) 15297–15302. <https://doi.org/10.1073/pnas.242600399>.
- [46] J. Hu, S. Li, B. Liu, Adsorption of BSA onto sulfonated microspheres, *Biochem. Eng. J.* 23 (2005) 259–263. <https://doi.org/10.1016/j.bej.2005.01.018>.

- [47] M. Tirado-Miranda, A. Schmitt, J. Callejas-Fernández, A. Fernández-Barbero, The aggregation behaviour of protein-coated particles: A light scattering study, *Eur. Biophys. J.* 32 (2003) 128–136. <https://doi.org/10.1007/s00249-002-0275-6>.
- [48] A. Hernández-Gordillo, A. Hernández-Arana, A. Campero-Celis, L.I. Vera-Robles, TiBALDH as a precursor for biomimetic TiO<sub>2</sub> synthesis: Stability aspects in aqueous media, *RSC Adv.* 9 (2019) 34559–34566. <https://doi.org/10.1039/c9ra05923g>.
- [49] Y. Zhang, J. Chen, X. Li, Preparation and photocatalytic performance of anatase/rutile mixed-phase TiO<sub>2</sub> nanotubes, *Catal. Letters.* 139 (2010) 129–133. <https://doi.org/10.1007/s10562-010-0425-x>.
- [50] H. Liu, J.B. Joo, M. Dahl, L. Fu, Z. Zeng, Y. Yin, Crystallinity control of TiO<sub>2</sub> hollow shells through resin-protected calcination for enhanced photocatalytic activity, *Energy Environ. Sci.* 8 (2015) 286–296. <https://doi.org/10.1039/c4ee02618g>.
- [51] D.A. Erdogan, T. Solouki, E. Ozensoy, A versatile bio-inspired material platform for catalytic applications: Micron-sized "buckyball-shaped" TiO<sub>2</sub> structures, *RSC Adv.* 5 (2015) 47174–47182. <https://doi.org/10.1039/c5ra04171f>.
- [52] J.B. Varley, A. Janotti, C.G. Van De Walle, Mechanism of visible-light photocatalysis in nitrogen-doped TiO<sub>2</sub>, *Adv. Mater.* 23 (2011) 2343–2347. <https://doi.org/10.1002/adma.201003603>.
- [53] V. Etacheri, M.K. Seery, S.J. Hinder, S.C. Pillai, Highly visible light active TiO<sub>2</sub>-xNx heterojunction photocatalysts, *Chem. Mater.* 22 (2010) 3843–3853. <https://doi.org/10.1021/cm903260f>.
- [54] W.J. Lee, J.M. Lee, S.T. Kochuveedu, T.H. Han, H.Y. Jeong, M. Park, J.M. Yun, J. Kwon, K. No, D.H. Kim, S.O. Kim, Biom mineralized N-doped CNT/TiO<sub>2</sub> core/shell nanowires for visible light photocatalysis, *ACS Nano.* 6 (2012) 935–943. <https://doi.org/10.1021/nn204504h>.

# CHAPTER 3. Metal-free g-C<sub>3</sub>N<sub>4</sub> Modification via Peptide for Enhanced Photocatalytic Hydrogen Generation

## 3.1. Introduction

Along with the exponential growth of the global population and the increase in affluence in the past decades, the extended resource demand and excessive pollution emissions have become a looming challenge worldwide. The pursuit of renewable energy as the replacement for fossil fuels has become urgent. Solar energy is the most enriched sustainable energy, and efficient transformation is of great importance to the solution of the energy crisis [1]. Hydrogen is considered alternative green energy due to its zero-carbon exhaust [2]. Particularly, solar-to-hydrogen conversion via photocatalytic water splitting has been widely investigated. A broad range of photocatalysts for solar water splitting has been studied. Most of them rely on materials containing metal such as metal oxides, metal sulfides, and complex metal semiconductors [3] which can cause environmental and human health issues due to their toxicity. Furthermore, noble metals such as Pt, Au, Ru, Ir, and Pd are widely used as cocatalysts in H<sub>2</sub>-generated photocatalysts because of their thermodynamic favorability for H<sub>2</sub> evolution and enhanced charge separation. Unfortunately, their large-scale application in industry is impeded due to their expensive cost, scarcity, and low stability. Given the above circumstance, searching for efficient sustainable metal-free photocatalysts for hydrogen production is in giant demand.

In comparison with commonly used visible-light metal oxide-based semiconductors, metal-free graphitic carbon nitride (g-C<sub>3</sub>N<sub>4</sub>) is a promising photocatalyst candidate to advance the solar energy harvest and conversion owing to its moderate bandgap (2.8 eV), high abundance in nature, non-toxicity, and high chemical stability [4]. However, bulk g-C<sub>3</sub>N<sub>4</sub> has low visible light absorption and rapid recombination of photo-generated carriers which still restrict its efficiency in real application. In general, the processes of photocatalytic hydrogen production by g-C<sub>3</sub>N<sub>4</sub> involve three steps: (1) light absorption, (2) charge separation, and (3)

surface reaction [3]. Abundant efforts have been made for exposing more active sites and improve the separation rate of electron-hole carriers of g-C<sub>3</sub>N<sub>4</sub>. The endeavors mostly focus on two aspects [5]. On one hand, obtaining porous g-C<sub>3</sub>N<sub>4</sub> nanostructure by texture control, for instance, precursors polycondensation [6], sonication [7], using strong acid as “chemical scissor” [8, 9], and the combination with other semiconductors or template [10-13]. On the other hand, the modification via chemical functionalization and element doping can not only narrow band gap [14, 15] but also generate a built-in electric field due to alternating tri-*s*-triazine structure unit of g-C<sub>3</sub>N<sub>4</sub> or inducing defects which can modulate the electronic structure and enhance photo-generated charge separation [16-18]. However, the as-mentioned methods normally require complicated synthesis processes, high temperatures, and toxic chemicals. There is a huge desire to seek green and simple routes of g-C<sub>3</sub>N<sub>4</sub> modification.

It is reported that biomaterials/ g-C<sub>3</sub>N<sub>4</sub> conjugations not only present great structural flexibilities and excellent stabilities but also expand sunlight harvest and enhance photocatalytic efficiency [19-21]. Recent studies have introduced the modification of g-C<sub>3</sub>N<sub>4</sub> with biomaterials as a valid route to overcome the shortcomings mentioned above and prompt photocatalytic activities with reduced impurities and pollutant emissions. Yang *et al.*[22] synthesized porous g-C<sub>3</sub>N<sub>4</sub> nanorods using carbonized poly (tannic acid) (cPTA). The abundant -NH<sub>2</sub> and -OH groups on g-C<sub>3</sub>N<sub>4</sub> make it feasible to form a strong adhesion with cPTA, resulting in the accelerated transfer of photo-induced carriers. Zhang *et al.*[23] modified g-C<sub>3</sub>N<sub>4</sub> by employing hydroxyethyl cellulose as a solid proton donor and a charge separation enhancer to increase photocatalytic efficiency. Zhao *et al.*[24] successfully induced amino groups into the tri-*s*-triazine structure unit of g-C<sub>3</sub>N<sub>4</sub> through the supramolecular assembly method, which significantly expanded the visible light absorption and intrinsic electronic properties compared to pristine g-C<sub>3</sub>N<sub>4</sub>, hence the H<sub>2</sub> generation was greatly enhanced. Chen *et al.* [25] prepared the pyrimidine-modified g-C<sub>3</sub>N<sub>4</sub> nanosheet with a curled morphology and accelerated the separation rate of charge carriers. By utilizing pyrimidine incorporation, the expansion of the graphite phase was hindered, and the local  $\pi - \pi$  conjugation was enhanced, so that it boosted the photocatalytic H<sub>2</sub> evolution performance.

In this study, a 14-mer peptide (RSTB1, LLLLLLLHRRPSRS) was incorporated with porous g-C<sub>3</sub>N<sub>4</sub> nanosheet via a simple process. It is predominantly confirmed based on

thermogravimetric analysis, zeta potential, atomic force spectroscopy, X-ray photoelectron spectrometry, Fourier transform infrared spectroscopy, Raman spectroscopy, molecular dynamic simulation, and DFT computation that the peptide has been successfully decorated on g-C<sub>3</sub>N<sub>4</sub> through electrostatic interaction between amine groups of the peptide and edge N atoms on the g-C<sub>3</sub>N<sub>4</sub> plane, resulting electron delocalization. Benefiting from the electronic structure altering, the increased UV-Vis absorbance, decreased band gap, and suppressed recombination rate of photogenerated charge carriers can be observed. Interestingly, the RSTB1 modified g-C<sub>3</sub>N<sub>4</sub> presented boosted hydrogen generation rate (2018  $\mu\text{mol g}^{-1} \text{h}^{-1}$ ) 14-fold to the pristine g-C<sub>3</sub>N<sub>4</sub> (140.8  $\mu\text{mol g}^{-1} \text{h}^{-1}$ ) under solar irradiation. It is worth noticing that no co-catalyst like Pt was employed in this system, which may provide a more economical approach to photocatalytic H<sub>2</sub> generation. The experiment and DFT results show that electron redistribution on the heptazine plane, deformed by interaction with the peptide, optimizes water adsorption energy and reduced the energy barrier for water splitting reaction.

## **3.2. Experimental**

### **3.2.1. Materials**

Melamine, potassium chloride (KCl), Na<sub>2</sub>SO<sub>4</sub>, and triethanolamine (TEOA) were obtained from Sigma-Aldrich Korea (Gyeonggi, South Korea), 14-mer peptide (RSTB1, sequence: LLLLLLL-HRRPSRS) was customized by Lugen Sci Co., Ltd. (Bucheon, Korea). Deionized water (D.I. water) was used throughout solution preparations and photocatalytic hydrogen evolution reactions.

### **3.2.2. Synthesis of g-C<sub>3</sub>N<sub>4</sub> nanosheet**

g-C<sub>3</sub>N<sub>4</sub> nanosheets (CN) were prepared via a one-step calcination process with KCl as pre-intercalator. 200 mg of melamine was mixed with 5 mL of KCl (2 mg L<sup>-1</sup>) under sonication for 1 h. After drying in an oven, the mixture was calcinated in a crucible at 550 °C for 4 h with a ramping rate of 10 °C min<sup>-1</sup>. The resulting mixture was washed with D.I. water and ethanol several times to remove the KCl and the product was collected by filtration and freeze-drying.

### 3.2.3. Synthesis of peptide-modified g-C<sub>3</sub>N<sub>4</sub> nanosheet

Peptide-modified g-C<sub>3</sub>N<sub>4</sub> nanosheet (RSTB1-CN) was synthesized by depicting as follows. 50 mg of CN was well dispersed into 25 mL D.I. water and sonication for 30 min. A certain amount of RSTB1 water suspension was added into CN dispersion dropwise and the total volume was kept at 40 mL. The mixture was vigorously stirred on a magnetic stirrer for 36 h under 25 °C. The final product was washed with D.I. water several times, then collected by centrifugation (6000 rpm, 5 min), and freeze-dried overnight. The serial samples with the different RSTB1 mass loading percentages of 2, 10, 15 % in the composite were denoted as 2R-CN, 10R-CN, and 15R-CN, respectively.

### 3.2.4. Photocatalytic hydrogen generation

The photocatalytic H<sub>2</sub> generation was conducted with a light source provided by a 300W Xenon lamp with a 400 nm cut-off filter (Solla, ORIEL). 20 mg catalyst was dispersed into 100 mL D.I water with 5 ml of triethanolamine (TEOA) as the sacrificial reagent. After 15 min sonication, the suspension was transferred to a Pyrex top-irradiation airtight glass reactor, which was connected to a closed-gas circulation system. The system was purged by high-purity N<sub>2</sub> gas and vacuumed five times to completely remove the impurity gases. The reactor was kept stirring and placed under the irradiation with a focused power density of 100 mW cm<sup>-2</sup> which is similar to 1 sun AM 1.5 G illumination. At certain irradiation intervals, the generated gas was extracted by a gas-tight syringe and injected into gas chromatography (6500 GC equipped with a thermal conductivity detector using ultrapure N<sub>2</sub> as carrier gas, YL instrument) to analyze the H<sub>2</sub> generation.

### 3.2.5. Characterizations

The field-emission scanning electron microscopy (FE-SEM; JSM-6500F, JEOL, Tokyo, Japan) and high-resolution transmission electron microscopy (TEM; JEM-2100F, JEOL) were applied to determine the morphologies of the samples. The specific surface area and relative porosity values were determined by the N<sub>2</sub> adsorption-desorption method using a

QUADRASORB™ SI Surface Area and Pore Size analyzer (Quantachrome Instruments, Boynton Beach, FL, USA). The X-ray diffraction (XRD; D/MAZX 2500V/PC high-power diffractometer, Rigaku, Tokyo, Japan), conducted at a scan rate of 2°C/min, Cu K $\alpha$ ,  $\lambda = 1.5415$  Å, was applied to analyze the crystalline structures. The content of peptide in the peptide-CN composite was collected by thermogravimetric analysis (TGA) between 30 and 800 °C at a heating rate of 10 °C/min (TGA Q50, TA Instruments, New Castle, DE, USA). Optical Chemical structures were investigated via X-ray photoelectron spectrometry and UPS (XPS; K-Alpha, Thermo Scientific), and Fourier transform infrared spectroscopy (FTIR; Nicolet 380, Thermo Scientific Nicolet iS5 with an iD1 transmission accessory, Waltham, MA, USA). Optical properties were analyzed using ultraviolet-visible (UV–Vis) diffuse reflectance (SPECORD 210 PLUS spectroscope, AnalytikJena, Jena, Germany) and photoluminescence (PL) spectrometer with an excitation wavelength of 380 nm (Agilent Technologies, Santa Clara, CA, USA). Atomic force microscopic (AFM) characterization was carried out by Bruker MM8 AFM to investigate surface morphology and height profile. Time-resolved fluorescence spectra were collected using emission decay profiles using an FS5 spectrofluorometer (Edinburgh Instruments Ltd, Livingston, UK) under 380 nm laser excitation; the spectra were fitted using triexponential functions for further confirmation of the photoexcited charge separation efficiency. The electron paramagnetic resonance (EPR) spectra were determined by JEOL JES-FA100 in a vacuum chamber.

### **3.2.6. Photoelectrochemical measurements**

The photoelectron chemical measurements were conducted on an electrochemical workstation (EC-Lab). A 0.05 M Na<sub>2</sub>SO<sub>4</sub> solution was applied as the electrolyte for the standard three-electrode system including a counter electrode (Pt sheet), a reference electrode (Ag/AgCl), and a working electrode prepared on indium tin oxide (ITO) glass. The working electrodes were prepared by a spray-coating method: 10 mg of photocatalyst and 1 mg of carbon black were dispersed in 3.8 ml of ethanol containing 0.2 mL of 5 % Nafion. The slurry was ultrasonicated for 30 min in an ice bath to obtain a homogeneous suspension. Then, the working electrode was made by spraying 4 mL of the slurry on an ITO glass (1 cm × 1 cm)



that was placed on a hot plate (90 °C) using a spray gun (Fig. 3.1). Electrochemical impedance spectroscopy (EIS) measurement was performed over a frequency range of 0.05 Hz to 100 kHz. A solar simulator with a 140 W xenon lamp and UV cut-off filter (Oriel Sol1A™ Class ABB system) was applied as the light source for transient photocurrent measurement.

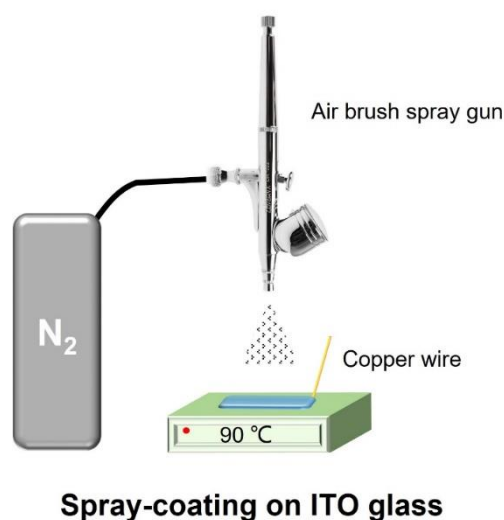


**Fig. 3.1.** Illustration of sample preparation for electrochemistry analysis.

### 3.2.7. Molecular Dynamic (MD) computation

To study the interaction between CN and peptide molecule, LAMMPS (large-scale Atomic/Molecular Massively Parallel Simulator) [26] was employed under a classical molecular dynamic. CHARMM forcefield was applied for both CN and the peptide to obtain structural minimization. The temperature was set at 300K during the whole computation using the velocity-rescale. The pressure was coupled at 1 atm using NVT (Langevin thermostat and production with Nose-Hoover) [27]. Visual Molecular Dynamics (VMD) and OVITO were used to observe the structural configuration of MD trajectories. The simulation was performed for 200 ns with the time step of 2.0 fs.

### 3.2.8. Density Functional Theory (DFT) computation

Density function theory (DFT) calculation was performed by using plane-wave Quantum-ESPRESSO packages [28, 29]. The generalized gradient approximation (GGA)

with Perdew-Burke-Ernzerhof exchange-correlation functional (PBE) [30, 31] was employed to accurately achieve chemisorption and absorption energy on the surface. The interaction between the valence electron and ions was described through ultrasoft pseudopotentials [32]. The Van der Waals (vdW) dispersive forces are modeled in form of the semiempirical Grimme-D3 approach [33]. The energy cutoff of the wavefunction and charge density were set in the range of 50 to 200 Ry, respectively. The convergence criteria for electronic structure iterations and force on each atom during structure relaxation were set to  $10^{-9}$  Ry and  $10^{-4}$  Ry/Bohr, respectively. For geometry optimization, all structure models are sampled by Brillouin zone with 12x12x1 Monkhorst-Pack k-point mesh to obtain convergence of total energy [34]. 15 Å vacuum in Z-direction was applied to avoid interlayer interaction. The (4x4) g-C<sub>3</sub>N<sub>4</sub> supercell was built. The g-C<sub>3</sub>N<sub>4</sub> structure with 3 heptazine units inclined 2.48 Å° was denoted as D-CN (distorted g-C<sub>3</sub>N<sub>4</sub>), whereas the normal single layer g-C<sub>3</sub>N<sub>4</sub> was denoted as P-CN (plane g-C<sub>3</sub>N<sub>4</sub>). All atoms were relaxed with converged force  $10^{-5}$  for geometry optimization and below  $10^{-2}$  eV/Å° for H<sub>2</sub>O dissociation. The steps of water dissociation were investigated by employing nudged elastic band method (CI-NEB) [35]. The adsorption energy of water on the catalyst surface is computed by the equation:

$$\Delta E_{\text{H}_2\text{O}} = E_{\text{slab}+\text{H}_2\text{O}} - E_{\text{slab}} - E_{\text{H}_2\text{O}} \quad (3 - 1)$$

Where  $E_{\text{slab}+\text{H}_2\text{O}}$  and  $E_{\text{slab}}$  are corresponding to total energy catalyst surfaces with and without water adsorption.  $E_{\text{H}_2\text{O}}$  is the total energy of one isolated H<sub>2</sub>O molecule in the gas phase.

The charge difference can be calculated by following equation [36]:

$$\Delta\rho = \rho_{\text{AB}} - \rho_{\text{A}} - \rho_{\text{B}} \quad (3 - 2)$$

Where  $\rho_{\text{AB}}$ ,  $\rho_{\text{A}}$ , and  $\rho_{\text{B}}$  are the charge density of the whole system and isolated A atoms and B atoms, respectively.

The Gibbs free energy of the catalyst was calculated by the following equations:

$$\Delta E_{\text{ads}} = E_{\text{catalyst-H}^*} - E_{\text{catalyst}} - \frac{1}{2} E_{\text{H}_2} \quad (3 - 3)$$

$$\Delta E_{\text{H}^*} = \Delta E_{\text{ads}} + \Delta E_{\text{ZPE}} - T\Delta S \quad (3 - 4)$$

Where  $E_{\text{catalyst-H}^*}$  donates the total energy of modeled catalyst with absorbed H state,  $E_{\text{catalyst}}$  stands for the energy of catalyst with bare surface, and  $E_{\text{H}_2}$  is the energy of hydrogen in the gas phase. The Gibbs free energy was calculated under conditions of zero-point energy (ZPE) and entropy corrections for the hydrogen evolution reaction.  $E_{\text{ZPE}}$  is the difference in zero-point energy.  $\Delta S$  is the entropy change between absorbed and gaseous hydrogen and  $T$  donates the temperature equal to 298K.  $\Delta E_{\text{ZPE}}$  is near 0.04 eV and  $\Delta S$  is around 0.2 eV. The reaction free energy is computed by the equation below:

$$\Delta E_{\text{H}^*} = \Delta E_{\text{ads}} + 0.24 \text{ eV} \quad (3 - 5)$$

### 3.3. Results and discussion

As illustrate in Fig. 3.2, the synthesis procedure of RSTB1-CN. Pristine CN nanosheets were prepared by a thermal polymerization process of melamine with KCl as the template for producing porosity structures via treating at 550 °C for 4 hours. The as-achieved CN was resuspended in D.I. water, and RSTB1 was added dropwise. After vigorously stirring for 36 hours in ambient environments, the final product was washed and collected by centrifugation and freeze-drying process.

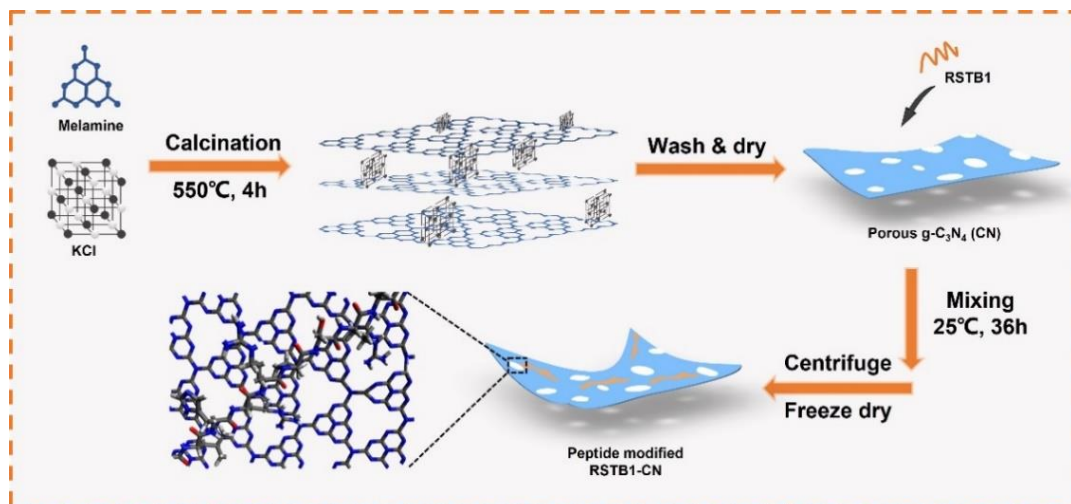


**Fig. 3.2.** Illustration of the synthesis of RSTB1 modified g-C<sub>3</sub>N<sub>4</sub> nanosheets.

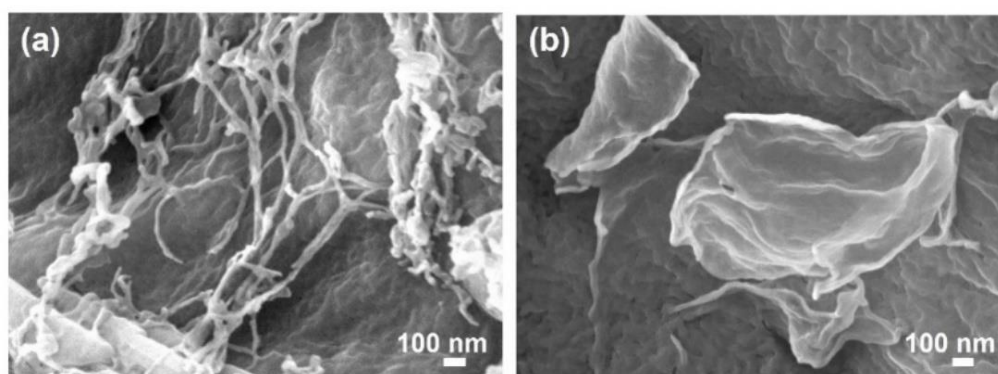


**Fig. 3.3.** FE-SEM images (a), (b) and (c) peptide sequence of RSTB1.

### 3.3.1. Characteristics

As shown in Fig. 3.4, the morphology of CN and 10R-CN were analyzed by FE-SEM, TEM and AFM. A typical nanosheet morphology of CN is observed, while 10R-CN presents a curled nanosheet with a porous structure (Fig. 3.4a-b). AFM images clearly reveal that the CN structure contains many pores with an average size of 2.5 nm, as depicted in Fig. 3.4c. It indicates the existence of both micro and macropores in the CN structure which can benefit mass transfer of reaction intermediates and gas release. In Fig. 3.4d, the uniformly dispersed peptide chains can be easily observed with a thickness of 2.58 nm (Pure peptide morphology

presented in Fig 3.3). BET analysis for porosity structures was conducted (Fig. 3.5). CN and 10R-CN exhibited Type IV isotherm curves with H3 hysteresis loop, suggesting the existence of mesopores. The pore structures were determined by BJH model for more explicit explanations. The specific surface area of CN and 10R-CN were 65.384 and 42.672 m<sup>2</sup> g<sup>-1</sup>, respectively, which were significantly improved compared to that of bulk g-C<sub>3</sub>N<sub>4</sub> (9.079 m<sup>2</sup> g<sup>-1</sup>). After the incorporation of RSTB1 into CN, the pore volume and surface area values of 10R-CN (0.338 cm<sup>3</sup>/g) were increased, indicating that the RSTB1 combination changes the structures of CN (0.236 cm<sup>3</sup>/g). TGA (Fig. 3.6a-b) confirms the existence of RSTB1 in the composites. Associating with the corresponding DTGA curves, the main weight loss between 300-380°C was observed in RSTB1. Consequently, the weight loss presents an increasing trend along with the higher RSTB1 percentage in the composites, in which CN has no significant weight loss. Besides, the major decomposition of CN and all composites occurred at 550-680°C, proving the great thermal stabilities (Table 3.1).

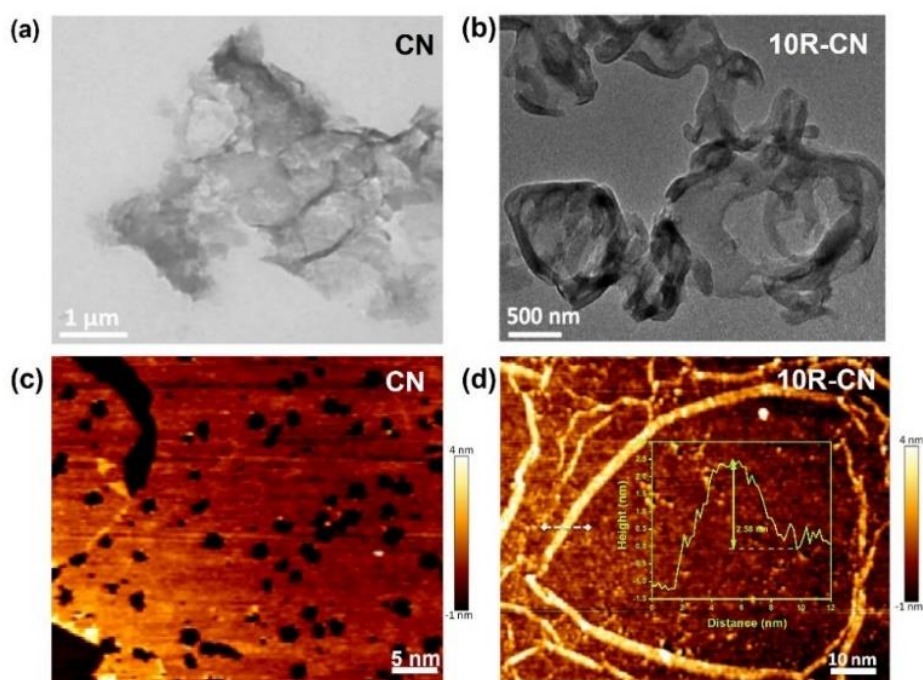


**Fig. 3.4.** (a) FE-SEM image of CN, (b) TEM image of 10R-CN, and AFM images of (c) CN and (d) 10R-CN. (The inserted is the height profile of the peptide)

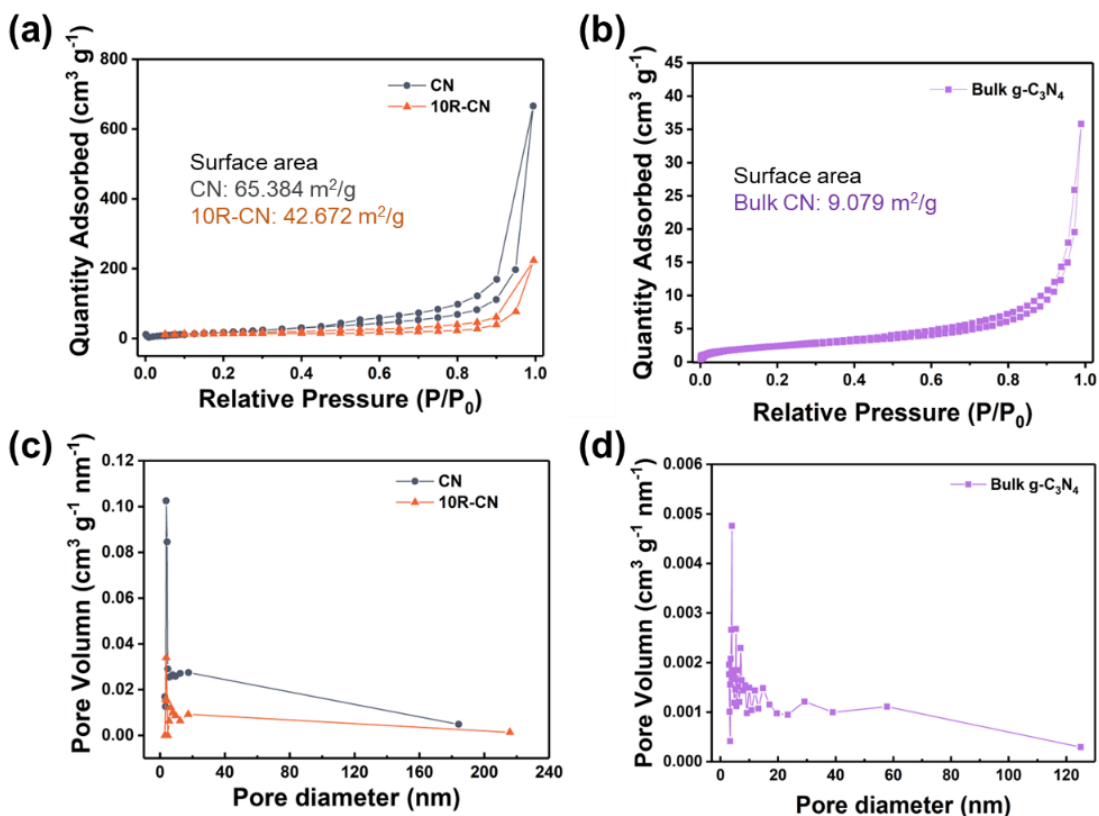


**Fig. 3.5.** Nitrogen adsorption-desorption isotherms of (a) CN and 10R-CN, (b) bulk g-C<sub>3</sub>N<sub>4</sub>, and corresponding pore-size distribution of (c) CN and 10R-CN, (d) bulk g-C<sub>3</sub>N<sub>4</sub>.

The functional groups were analyzed by FTIR spectra (Fig. 3.6c). CN presented the characteristic peaks of g-C<sub>3</sub>N<sub>4</sub>. The strong peak near 809 cm<sup>-1</sup> stands for the triazine ring vibrations, the band in the range of 1100–1750 cm<sup>-1</sup> corresponding to the typical N-C=N heterocycles. And a broad band in the range of 3000–3400 cm<sup>-1</sup> is contributed by the terminal N-H stretching. The band located around 3400 cm<sup>-1</sup> of 10R-CN and 15R-CN became wider compared to CN and 2R-CN could be due to the more N-H groups in the composites from the higher amount of RSTB1 [23, 24]. The similar FTIR spectra for all the samples indicate the good retention of g-C<sub>3</sub>N<sub>4</sub> units' structures. Besides, it could be ascribed that the covalent bond should not be the main interaction between RSTB1 and CN [37]. Moreover, the signal of  $\beta$ -sheet secondary structure was observed at 1631 cm<sup>-1</sup> in the FTIR of RSTB1 (Fig. 3.6d). The CN characteristic peak in 2R-CN, 10R-CN and 15R-CN was shifted from 1635 to 1631 cm<sup>-1</sup>, confirming the existence of peptide in the composites [38]. Zeta-potential of CN was -34.01

mV, while RSTB1 presented +9.34 mV at pH 7.5. With increased RSTB1 addition, the zeta-potential values became more positive, revealing that the electrostatic force existed between RSTB1 and CN (Fig. 3.7a). XRD was employed to analyze the crystalline phase (Fig. 3.7b). XRD pattern of CN exhibited the representative peaks at  $12.8^\circ$  and  $27.7^\circ$  corresponding to the (100) and (002) plane of g- $C_3N_4$ , respectively. The peak of (100) can be ascribed as tri-s-triazine in-plane packing, while the (002) plane is assigned to the interlayer stacking of aromatic conjugated structures [39]. It is observed that the sharp peak at  $12.8^\circ$  disappeared in 2R-CN, 10R-CN and 15R-CN, it is due to the long-range atomic structure disorder of g- $C_3N_4$  [40]. Moreover, the peak at  $27.7^\circ$  shifted to a lower degree in RSTB1 modified samples, indicating the interaction of g- $C_3N_4$  interlayers was decreased and the interplanar spacing was enlarged. It can be attributed to a weak interlayer stacking effect by the insertion of RSTB1 [2].

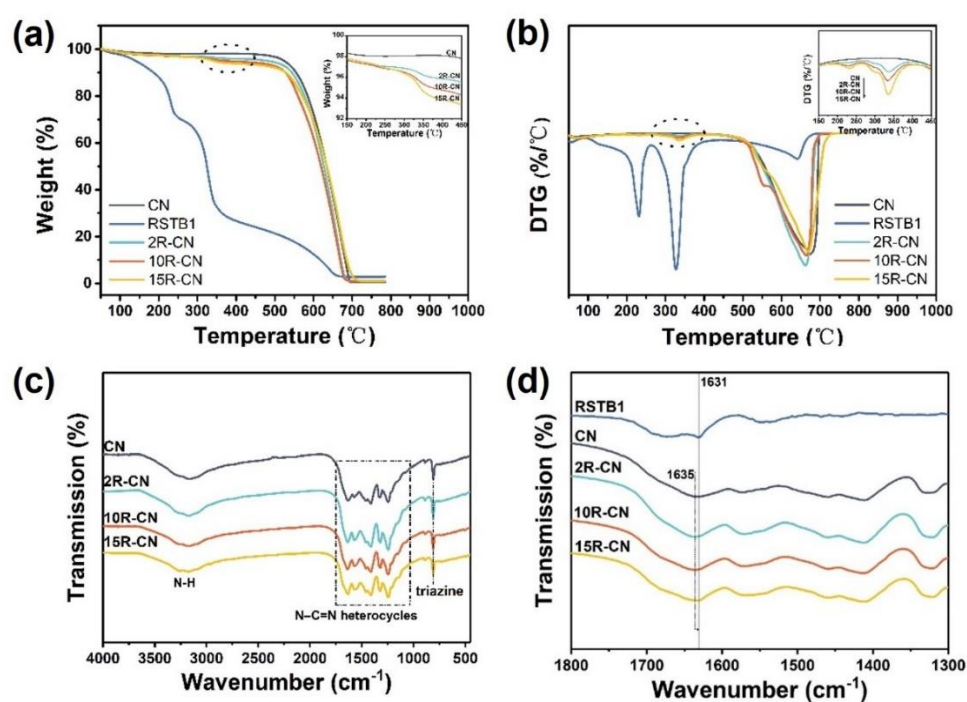


**Fig. 3.6.** (a) TGA and (b) DTGA of RSTB1, CN, 2R-CN, 10R-CN and 15R-CN; (c) FTIR spectra and (d) Enlarged FTIR of RSTB1, CN, 2R-CN, 10R-CN and 15R-CN.

**Table 3.1.** TGA results of RSTB1-CN.

Sample	Weight (%, at 450°C)	RSTB1 content (%)
CN	97.8	-
RSTB1	24.5	-
2R-CN	95.5	4.5
10R-CN	94.3	5.7
15R-CN	93.4	6.6

The chemical composition of CN and 10R-CN was evaluated by XPS spectra to understand the effect of the peptide on the g-C<sub>3</sub>N<sub>4</sub> structure (Fig. 3.8). The atomic ratio of C/N is determined to be 0.82 for CN and 1.03 for 10R-CN. The XPS survey spectra of 10R-CN exhibit a stronger O 1s peak than that of CN, suggesting that more oxygen atoms on its surface. In high resolution XPS spectra of O 1s, the only peak in CN at 531.1 eV is assigned as H<sub>2</sub>O. Meanwhile, a new peak was detected at 529.9 eV in 10R-CN, representing the C-O species on its surface. All the above results reveal that the RSTB1 has been grafted in CN, which is corresponded to the FTIR results. Fig. 3.8c shows that the high-resolution C 1s XPS spectra of CN were deconvoluted into three peaks at 287.3, 285.5 and 283.8 eV, corresponding to the sp<sup>2</sup>-hybridized carbon (N=C-N), C-NH<sub>x</sub>, and accident carbon, respectively [22]. Three peaks in C 1s spectra of 10R-CN shifted toward lower binding energies were observed. In N 1s spectra of CN ((Fig. 3.8d), a major peak at the binding energy of 397.6 eV is ascribed to the C-N=C from the two coordinated nitrogen atoms in the g-C<sub>3</sub>N<sub>4</sub> structure [41]. The peak at 399.0 eV is related to the N-C3 with high thermodynamic stability. Another peak observed at 399.8 eV could be the terminal amino group (C-NH<sub>x</sub>). Three peaks in N 1s of 10R-CN all shifted to lower binding energies as well. These results indicate that the electron density of carbon and nitrogen was increased, and the structure distortion of 10R-CN could modulate the electronic configuration of tri-s-triazine since RSTB1 is incorporated with CN [25, 42].



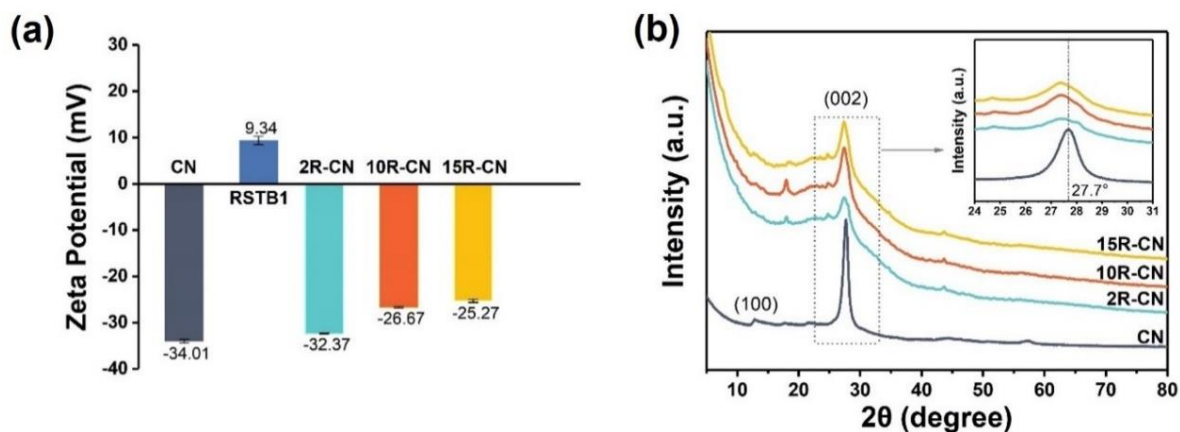


**Fig. 3.7.** (a) Zeta potential at pH 7.5, (b) XRD patterns of CN, 2R-CN, 10R-CN and 15R-CN. (The inset is the enlarged XRD in the range of 25-30°).

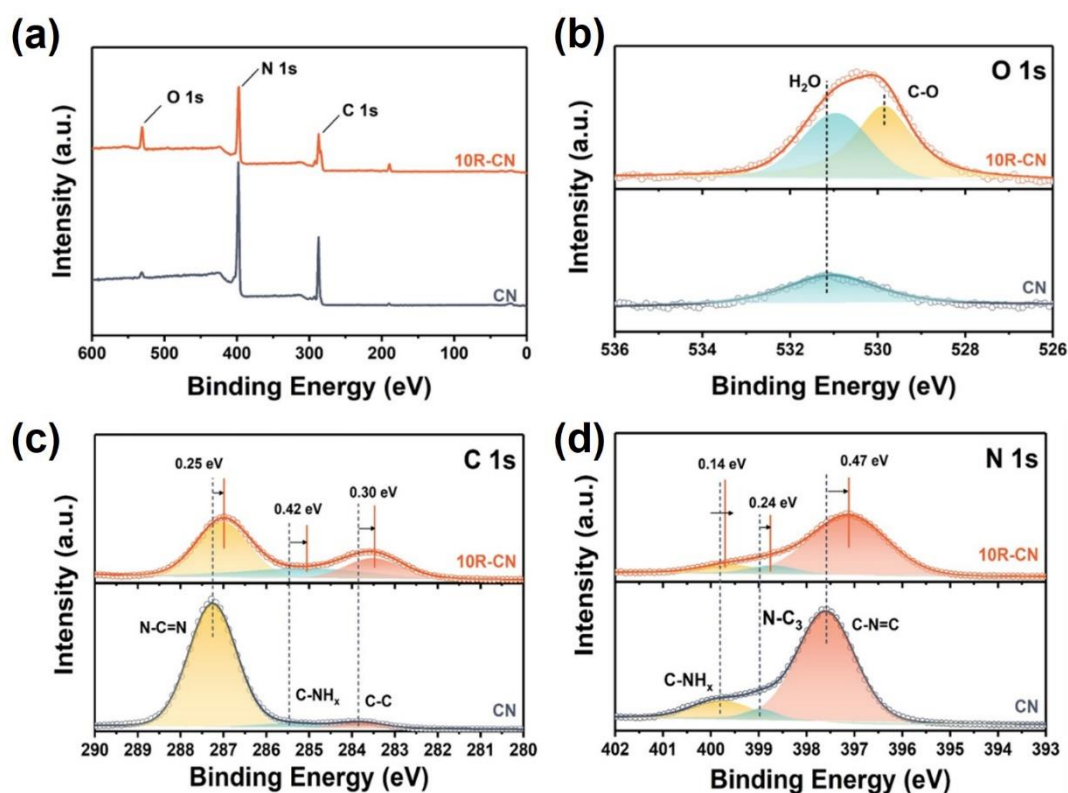


**Fig. 3.8.** XPS (a) survey spectra, High-resolution XPS spectra of (b) O 1s, (c) C 1s and (d) N 1s of CN and 10R-CN.

To further gain a deeper insight into the electronic modulation, MD simulation and DFT computation was performed to infer structure and electronic configuration in the presence of RSTB1. Fig. 3.9a presents MD snapshot of the RSTB1 and CN plane at 21.8 ns, demonstrating the adsorption of the RSTB1 on CN surface. It can be observed that amine groups from RSTB1 were approached and positioned at the center of N-encircling formed by three heptazine units, while these tri-s-triazine planes were inclined around  $2.48 \text{ \AA}^\circ$  above CN plane. It has been known that pyridine N in heptazine units possesses a negative charge which is able to attract positively charged amine groups of the RSTB1 via electrostatic interaction (Fig. 3.9b-c). Based on MD model, the supercell with  $4 \times 4$  tri-s-triazine units contained three  $2.48 \text{ \AA}^\circ$ -outward-inclined heptazine (D-CN) was constructed and optimized geometry using GGA-PBE method (Fig. 3.10). As the result of binding, the heptazine planes surrounding amine groups were outward twisted from the original plane which may generate short-range defects. To unveil electronic changes due to the outward twisting, the First-Principles DFT calculation was employed. Fig. 3.11a-b displays visualized charge different calculations of P-CN and D-CN. P-CN has a mostly symmetrical charge distribution which causes rapid electron-hole recombination, whereas D-CN shows breakage of  $\pi$ -conjugated aromatic heterocycles of C-C bonding and charge balance, thus leading to increase asymmetrical charge redistribution and electron delocalization. As reported in the literature [43], the short-range electron delocalization region in g- $\text{C}_3\text{N}_4$  plays an important role in generating a built-in electrical field that can effectively accelerate photo-induced electron-hole separation. To further study electronic configuration, the density of state (DOS) and partial density of state (PDOS) were calculated, as illustrated in Fig. 3.11c-d. In general,  $\text{N}_p$  contributes mainly to the top states of the valance band (VB), and the bottom states of conducting band (CB) is primarily originated from  $\text{C}_p$  and  $\text{N}_p$ . In comparison with CN, inclined tri-s-triazine planes have induced more CB states forward Fermi level and decreased band gap. It suggests that the introduction of electron delocalization significantly increases electron migration on the heptazine surface demonstrating the improved electron transfer which coincides with the results of XPS spectra. The calculation of the band gap also reveals narrowed value of D-CN (1.981 eV) which is smaller than that of CN (2.8 eV), as shown in Fig. 3.11e-f. Notably, this D-CN structure could be beneficial for facilitating more visible light response and favorable catalytic activity.

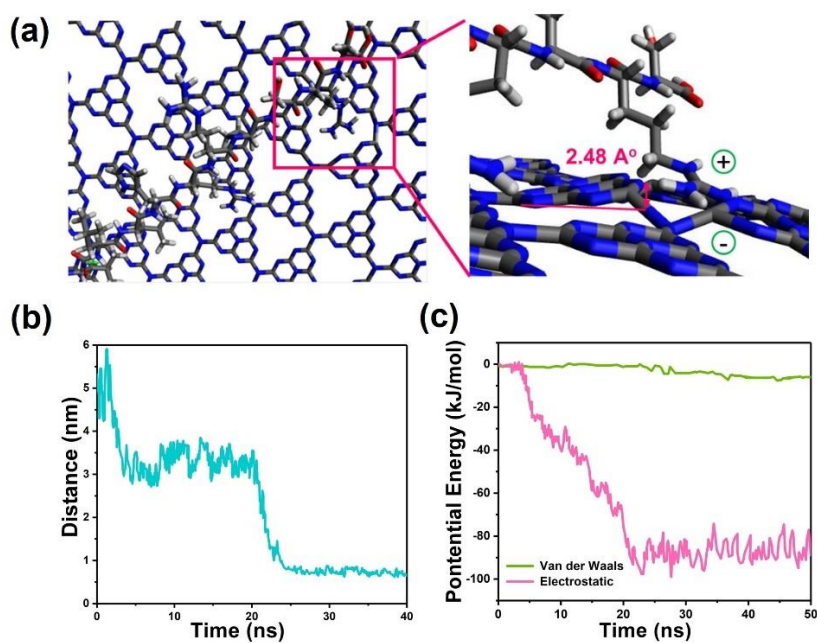


**Fig. 3.9.** (a) MD snapshots of interaction event between RSTB1 and CN plane at 21.8 ns. (b) The time-dependence centre of mass (COM) distance between CN and peptide. (c) Van der Waals and electrostatic interaction energies between components as the function of simulation.

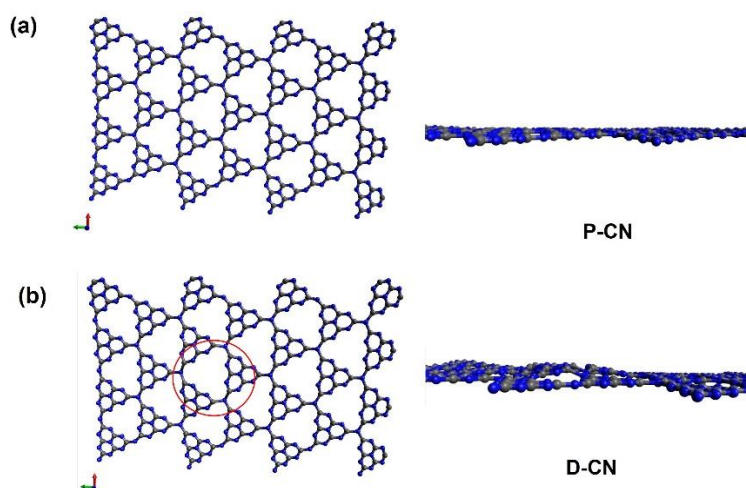


**Fig. 3.10.** Optimal geometry of P-CN and D-CN. Top view (left) and side view (right)

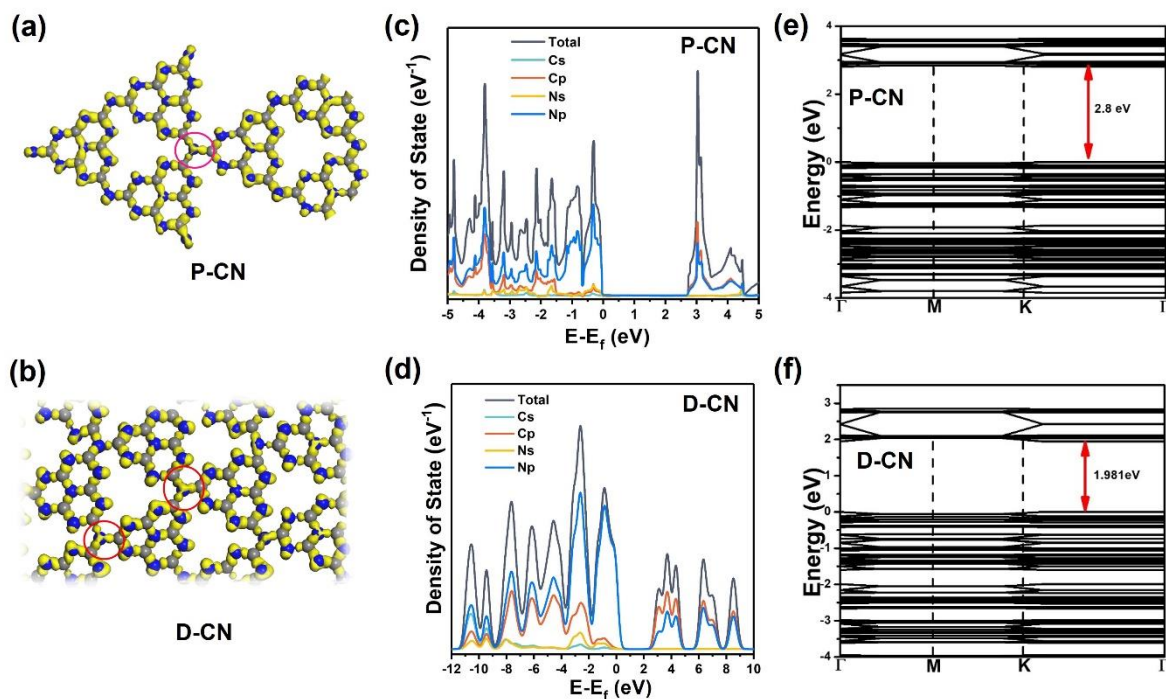


**Fig. 3.11.** DFT computation of charge difference of (a) P-CN, (b) D-CN with isosurface value of 0.009 (yellow color means electron accumulation and cyan color means electron depletion). QE-HSE calculated the electronic band structure of (c) P-CN, (d) D-CN, and DOS of (e) P-CN and (f) D-CN.

### 3.3.2. Optical and photoelectrochemical properties

The UV-Vis spectra of CN, 2R-CN, 10R-CN and 15R-CN were utilized for light harvest investigation. As exhibited in Fig.3.12a, the strong adsorption peaks of all prepared samples are centered at 330 nm. All as-prepared RSTB1-CN samples possess obvious redshift and increased absorption capacity. It is noted that 10R-CN shows the strongest absorption in the visible region. However, the reduced absorption in 15R-CN may be attributed to electrostatic interaction between peptides that could prevent the distorted effect of the peptide on the CN plane. The more inclined tri-s-triazine planes were generated, the more electron delocalized region could be contributed to light absorption capacity owing to effective charge transfer and increased CB states. The same behavior can be observed in the optical band gap calculated by Tauc formula in which 10R-CN shows the smallest band gap (2.1 eV) compared to other

samples including CN (2.99 eV), 2R-CN (2.75 eV) and 15R-CN (2.54 eV) (Fig. 3.12b). Moreover, the photo-generated electron-hole charge separation was clarified using PL, EIS, photocurrent, and time-resolved fluorescence decay spectra. Fig. 3.12c presents the PL emission peak located around 450 nm for all samples under 380 nm excitation wavelength. Compare with CN, the intensities of all RSTB1-CN samples exhibit a quenching effect, indicating enhanced photo-produced charge separation. Especially, 10R-CN shows the most quenching. It implies that the recombination process of photo-generated electron-hole pairs was suppressed. The PL quenching in 10R-CN could be attributed to the inhibition of photo-generated charges' recombination by a built-in electrical field at the intersection between short-range disorder and long-range atomic order on the g-C<sub>3</sub>N<sub>4</sub> surface [40]. Electrochemical impedance spectroscopy (EIS) and photocurrent measurements were further analyzed to evaluate visible light harvesting efficiency (Fig. 3.12d). Compared to CN, the arc radius of 2R-CN, and 10R-CN in Nyquist plots significantly decreased, suggesting a reduced resistance of electron transfer. It is worth noticing that 10R-CN exhibits the highest charge transfer, while, 15R-CN has the largest charge transfer resistance. Associating to the transit photocurrent response (Fig. 3.12e), the photocurrent of 10R-CN was obtained significantly higher than all the samples, denoting the largest mobility and the minimum recombination of photogenerated carriers. It is of notice that the photocurrent of 15R-CN was 0.8  $\mu$ A lower than that of CN, the lowest conductivity and photocurrent may be due to interchain interaction between peptide and insulator characteristic of peptide which declines photo-induced charge separation and block electron transfer on the surface of the electrode, confirming that the optimized RSTB1 modification is essential for the improvement of charge separation. The time-resolved PL spectra were analyzed to further investigate the separation of photogenerated charge carriers (Fig. 3.12f). The average PL lifetime values were calculated as 5.04 ns, 5.15 ns, 5.25 ns and 5.45 ns for CN, 2R-CN, 10R-CN and 15R-CN, respectively (the fluorescence decay lifetime parameters are summarized in Table 3.2). It suggests that the photogenerated carriers in the composites with higher RSTB1 amounts have prolonged lifetimes, therefore the chances for them to migrate to the surface for the photocatalytic reaction are extended, which primarily confirmed the enhancement of the charge separation efficiencies. These results can be demonstrated that 10R-CN possesses fast and effective

charge transport and photogenerated electron-hole pairs separation. Therefore, 10R-CN was chosen as the optimal sample. With no doubt, RSTBI-CN samples may be a promising metal-free visible-light photocatalyst.

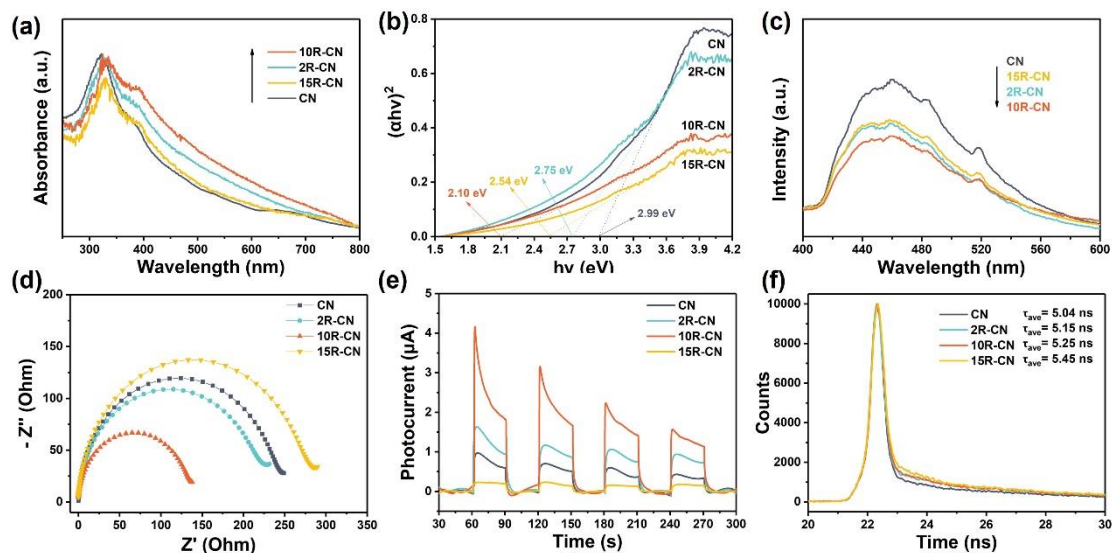


**Fig. 3.12.** (a) UV-Vis absorption spectra and (b) Tauc plots, (c) PL emission spectra, (d) EIS Nyquist plots, (e) The transient photocurrent response curves, and (f) Time-resolved PL spectra of CN, 2R-CN, 10R-CN and 15R-CN.

**Table 3.2.** Summary of the fluorescence decay lifetime parameters.

Sample	$\tau_1$	$A_1$	$\tau_2$	$A_2$	$\tau_3$	$A_3$	$\tau_{ave}$ (ns)
CN	0.1203	0.05	0.908	0.1101	5.875	0.8399	5.040368
2R-CN	0.1304	0.0672	1.483	0.1151	6.0836	0.8176	5.153601
10R-CN	0.1386	0.0643	1.9279	0.1178	6.1296	0.8179	5.249468
15R-CN	0.1935	0.0738	4.6308	0.6748	9.174	0.2514	5.445384

### 3.3.3. Photocatalytic H<sub>2</sub> generation

The photocatalytic activity of CN, 2R-CN, 10R-CN and 15R-CN was evaluated by the photocatalytic hydrogen generation under visible-light illumination without the addition of any co-catalysts. As shown in Fig. 3.13a-b, the H<sub>2</sub> generation rates of 2R-CN, 10R-CN and 15R-CN are significantly higher than that of CN. The highest H<sub>2</sub> generation rate was observed on 10R-CN (2018.4  $\mu\text{mol g}^{-1} \text{h}^{-1}$ ), which is 14 folds higher compared to CN (140.8  $\mu\text{mol g}^{-1} \text{h}^{-1}$ ). It is noted that 15R-CN presents a lower rate than it of 10R-CN, it could be ascribed to the blockage of the active site by the excess peptide amount. The composites of g-C<sub>3</sub>N<sub>4</sub> nanosheets and different peptides with various amine functional groups were synthesized to confirm the effect of the RSTB1 peptide. As shown in Fig. 3.14a, the composites with other peptides exhibit poor hydrogen production activity, demonstrating the improved photocatalytic efficiency through RSTB1 and g-C<sub>3</sub>N<sub>4</sub> with distorted planes (The properties of peptides were listed in Table 3.3). Notably, the photocatalytic performances of as-prepared catalysts are comparable to other metal-free organic modified g-C<sub>3</sub>N<sub>4</sub> materials (Table 3.4). The stability of 10R-CN was analyzed via a 4-hour H<sub>2</sub> generation process for 4 runs under the same condition. After a 4-cycle reaction, the accumulated H<sub>2</sub> generation can remain on a high yield level ( $\sim 8000 \mu\text{mol g}^{-1}$ , Fig. 3.13c). Great stability was presented via the relevant H<sub>2</sub> generation rate in Fig. 3.13d. It is obvious that the hydrogen generation rate still holds up to  $2005.8 \mu\text{mol g}^{-1} \text{h}^{-1}$ , which is a.u. 99% of photocatalytic capability was maintained after 4 cycle runs. Furthermore, the linear sweep voltammetry (LSV) for hydrogen evolution reaction (HER) of CN, 2R-CN, 10R-CN and 15R-CN samples was measured. In Fig. 3.13e, the 10R-CN possesses the small HER overpotential of 80 mV at the current density of  $10 \text{ mA/cm}^2$  which is lower than those other composite samples, indicating favored thermodynamics toward hydrogen evolution reaction. Interestingly, 10R-CN also performs excellent and stable photocatalysis in water splitting with generation rates of  $2047.7 \mu\text{mol g}^{-1} \text{h}^{-1}$  and  $1023.8 \mu\text{mol g}^{-1} \text{h}^{-1}$  for H<sub>2</sub> and O<sub>2</sub>, respectively, as presented in Fig. 3.13f. It is suggesting that 10R-CN is not only an efficient photocatalyst for photocatalytic hydrogen evolution but also a promising catalyst for water splitting with great reusability.



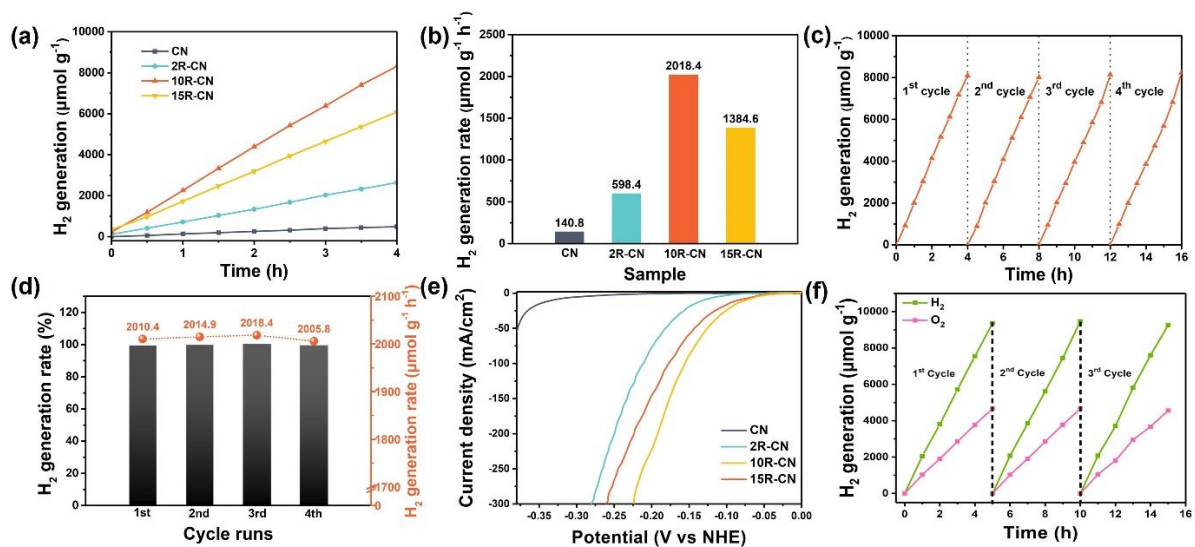


**Fig. 3.13.** (a) The amount of hydrogen generation vs. time and (b) hydrogen generation rate of CN, 2R-CN, 10R-CN and 15R-CN under visible-light irradiation. (c) Stability cycle runs for H<sub>2</sub> generation and (d) the corresponding rate of 10R-CN in recycling runs. (e) Electrochemical HER LSV curves of CN and RSTB1-CN composites. (f) Hydrogen and oxygen photocatalytic generation performance of 10R-CN during continuous three cycling.

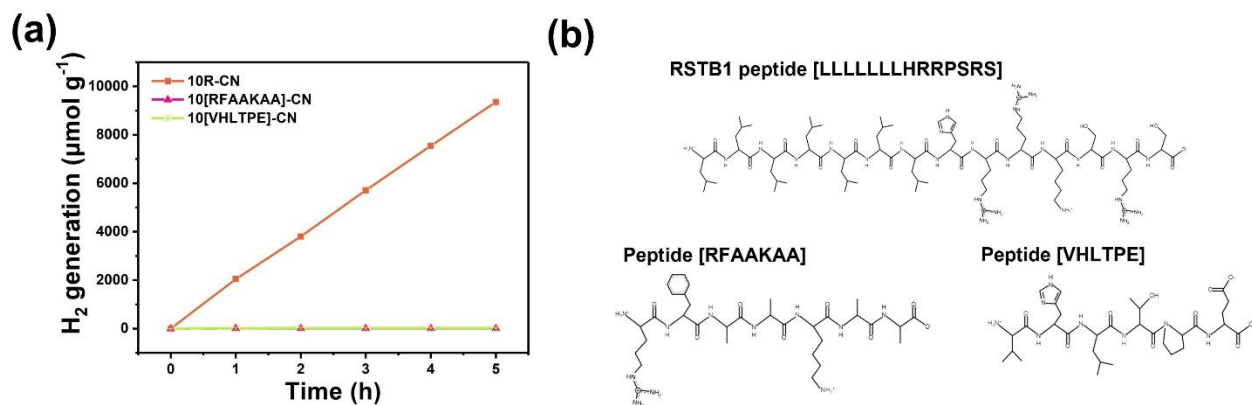


**Fig. 3.14.** (a) Hydrogen photocatalytic generation performance of 10R-CN, and CN with peptide [RFAAKAA] and peptide [VHLTPE]. (b) Illustration of peptide structures.



**Table 3.3.** Summary of peptide properties.

Peptide Sequence	Mass (g/mol)	Isoelectric point (pI)	Net charge
LLLLLLLHRRKSRS	1717.1	12.79	+4
RFAAKAA	733.4	11.56	+2
VHLTPE	694.4	5.06	-1

**Table 3.4.** Biomaterial-based metal-free g-C<sub>3</sub>N<sub>4</sub> for photocatalytic H<sub>2</sub> evolution.

Material	Sacrificial agent	Co-catalyst	H <sub>2</sub> generation (μmol h <sup>-1</sup> g <sup>-1</sup> )	Light Source	Ref. (year)
RSTB1-CN	TEOA	-	2018.4	300 W Xe lamp (λ > 400 nm)	This study
Carbon-Vacancy g-C <sub>3</sub> N <sub>4</sub>	TEOA	Pt	3304.5	300 W Xe lamp (λ > 420 nm)	[2] (2022)
Pyrimidine-modified g-C <sub>3</sub> N <sub>4</sub>	TEOA	Pt	1046	300 W Xe lamp (λ ≥ 420 nm)	[25] (2021)
Carbon/g-C <sub>3</sub> N <sub>4</sub>	TEOA	Pt	8.88	300 W Xe lamp (λ > 400 nm)	[44] (2020)
CN/CuPc	TEOA	-	71.2	300 W Xe lamp	[45] (2020)
g-C <sub>3</sub> N <sub>4</sub> -SiC	TEOA	Pt	595.3	300 W Xe lamp (λ ≥ 420 nm)	[46] (2019)
(F8T2) Pdots/g-C <sub>3</sub> N <sub>4</sub>	TEOA	-	929.3	300 W Xe lamp (λ > 400 nm)	[47] (2019)
O-g-C <sub>3</sub> N <sub>4</sub>	Glucose	Pt	1370	Simulated solar light (500 W m <sup>-2</sup> )	[48] (2018)
C-C3N4	TEOA	Pt	1636.45	150 W Xe lamp (λ ≥ 420 nm)	[49] (2018)
Black phosphorus/g-C <sub>3</sub> N <sub>4</sub>	Methanol	-	190	200 W Xe lamp	[50] (2018)
phosphorene/g-C <sub>3</sub> N <sub>4</sub>	Lactic acid	-	571	300 W Xe lamp (λ ≥ 420 nm)	[51] (2018)
Half-metallic g-C <sub>3</sub> N <sub>4</sub>	TEOA	-	1009	300 W Xe lamp (AM 1.5 G filter)	[52] (2018)
PFBT/g-C <sub>3</sub> N <sub>4</sub>	TEOA	Pt	722.3	300 W Xe lamp (λ > 420 nm)	[53] (2017)
P7-g-C <sub>3</sub> N <sub>4</sub>	TEOA + Methanol	-	1492	300 W Xe lamp (λ > 420 nm)	[54] (2016)
C-ZIF/g-C <sub>3</sub> N <sub>4</sub>	TEOA	-	32.6	300 W Xe lamp (λ > 400 nm)	[55] (2016)
CDots/g-C <sub>3</sub> N <sub>4</sub>	TEOA	-	218	350 W Xe lamp (λ ≥ 420 nm)	[56] (2016)
Few-layer g-C <sub>3</sub> N <sub>4</sub>	Ethanol / H <sub>2</sub> O	-	110.68	Xe lamp (λ > 400 nm) + Hg lamp (254 nm)	[57] (2015)
CQDs/g-C <sub>3</sub> N <sub>4</sub>	Methanol	-	219.5	1000 W Xe lamp (λ ≥ 420 nm)	[58] (2015)
Holey g-C <sub>3</sub> N <sub>4</sub>	TEOA	Pt	82.9	300 W Xe lamp (λ ≥ 420 nm)	[59] (2015)
MWCNT/g-C <sub>3</sub> N <sub>4</sub>	Methanol	-	42	300 W Xe lamp (λ > 395 nm)	[60] (2012)

### 3.3.4. Plausible mechanisms

The bandgap alignment was investigated to verify the photocatalytic hydrogen evolution mechanism. The Mott-Schottky curves were plotted in Fig. 3.15a. CN and 10R-CN present positive slopes, which confirmed that they are n-type semiconductors. The flat-band potentials ( $E_{fb}$ ) for CN and 10R-CN are observed as -1.53 and -0.87 eV vs. Ag/AgCl (-1.33 and -0.67 eV vs. NHE), respectively. Generally, the conduction band value ( $E_{CB}$ ) can be estimated via the equation  $E_{CB} = E_{fb} - 0.1$  [61], therefore, the  $E_{CB}$  of CN and 10R-CN are calculated as -1.43 and -0.77 eV (vs. NHE). Together with the optical bandgap ( $E_g$ ) value obtained by UV-Vis, the  $E_{VB}$  (valence band) can be calculated following the equation  $E_g = E_{VB} - E_{CB}$ . So that the  $E_{VB}$  for CN and 10R-CN are +1.56 and +1.33 eV (vs. NHE), respectively (Fig. 3.15b).  $E_{VB}$  values can be confirmed by UPS as well (Fig. 3.15c-d).

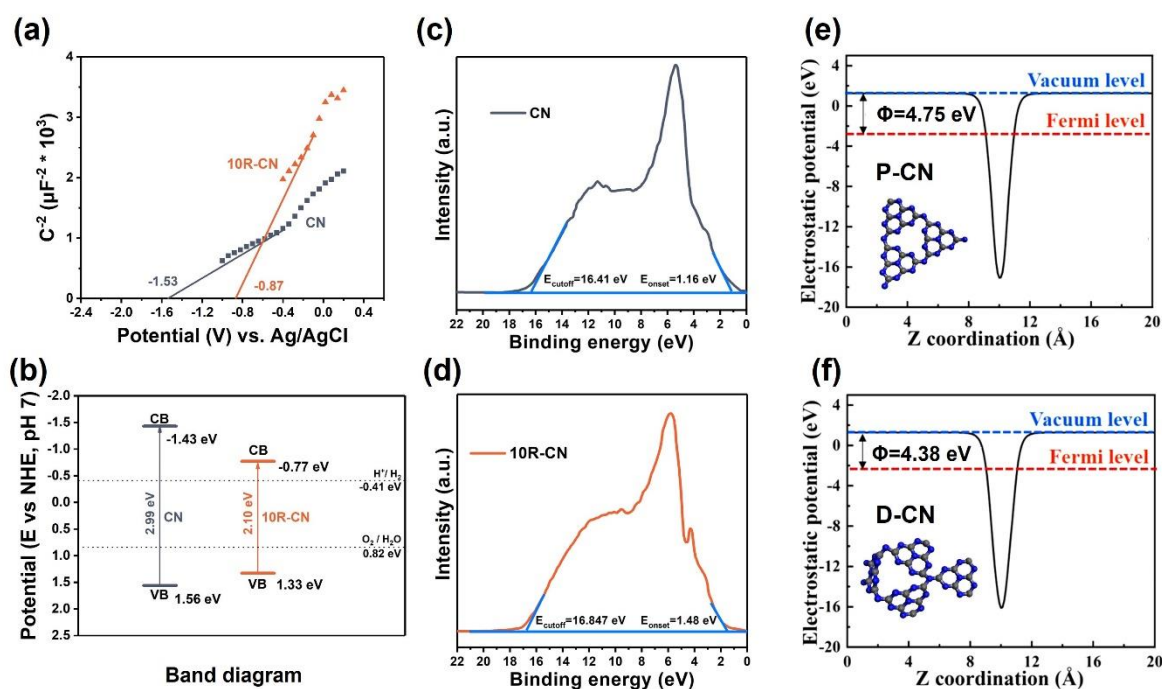


**Fig. 3.15.** CN and 10R-CN analysis of (a) Mott-Schottky plot, (b) band diagram, (c-d) UPS and DFT calculation of (e) P-CN, (f) 10R-CN.

$E_{VB}$  values can be confirmed by UPS as well (Figure 3.13 (b) and (e)). According to the equations below:

$$E_{VB} = (21.22 - E_w) - 4.44 \quad (3 - 1)$$

$$E_w = E_{cutoff} - E_{onset} \quad (3 - 2)$$

The  $E_{VB}$  of CN and 10R-CN from UPS were thus calculated as 1.53 and 1.393 eV, respectively [62]. The UPS results are in a good agreement to the  $E_{VB}$  obtained from optical bandgap values.

The work function ( $\Phi$ ) and Fermi levels ( $E_F$ ) of the CN and 10R-CN can be achieved from UPS results via the start value of secondary photoemission ( $E_{cutoff}$ ) following equation 3-3 and 3-4:

$$h\nu (\text{He}, 21.22 \text{ eV}) = E_{cutoff} + \Phi \quad (3 - 3)$$

$$E_F (\text{vs NHE, at pH} = 7) = -4.44 - E (\text{vs Vacuum level}) - 0.059 \text{ pH} \quad (3 - 4)$$

$E_F$  of CN and 10R-CN were thereby calculated to be -0.043 eV and -0.48, respectively [63][13]. Meanwhile, the work function ( $\Phi$ ) of isolated P-CN structure and D-CN structure were obtained by DFT as shown in Figure 3.13 (c, f). And Fermi levels ( $E_F$ ) of which were estimated as -0.103 eV and -0.473 eV for P-CN and D-CN by Equation 3-4, respectively. Notably, the Fermi level of 10R-CN (-0.043eV) has located in between isolated P-CN and D-CN.

Based on all the above evidence, it is reasonable to suggest that 10R-CN consists of both distorted (D-CN) and plane structures (P-CN) of  $g\text{-C}_3\text{N}_4$ . The work function ( $\Phi$ ) and Fermi levels ( $E_F$ ) of D-CN and P-CN were obtained from DFT calculations (Fig. 3.15e-f). The difference between  $\Phi$  would result in the generation of a built-in electric field with the direction from the lower  $\Phi$  towards the higher  $\Phi$  [64]. As illustrated in Fig. 3.16, before contact, the D-CN has a higher Fermi level than that of P-CN, thus leading to electron movement from D-CN to P-CN until the Fermi level reaches the same level after the contact. Because of electron migration, the CB and VB of P-CN were bent downward, while the CB and VB of D-CN surrounding area were curved upward. As a result, the electron depletion and accumulation region appeared at D-CN and P-CN, respectively. After the formation of

homojunction, the built-in electric field is generated owing to charge reorganization. Under light radiation, photo-generated electrons are accumulated in CB of D-CN, meanwhile, the photo-induced holes are accumulated in VB of P-CN. These electrons and holes with less redox abilities are enforced to the recombination in the contact region due to the driving force of the built-in electric field, bent band and columbic force. So that the photo-excited electrons in the CB of D-CN and the holes in the VB of P-CN can be preserved for more efficient photocatalytic reactions [65], thereby, such a S-scheme mechanism was suggested. The narrowed band structure still meets the thermodynamic requirements for redox potentials of  $H^+/H_2$  and  $O_2/H_2O$  [66]. The EPR was measured to evaluate the production of lone pair electrons under an excitation wavelength of 420 nm. As depicted in Fig. 3.17a, the 10R-CN exhibits the most intensified signal, which originated from the unpaired electrons of  $sp^2$  carbon in g- $C_3N_4$  heptazine rings [67, 68]. Compared to bulk g- $C_3N_4$  and CN, the significantly promoted EPR intensity of 10R-CN implies more generated lone-pair electrons for hydrogen evolution.

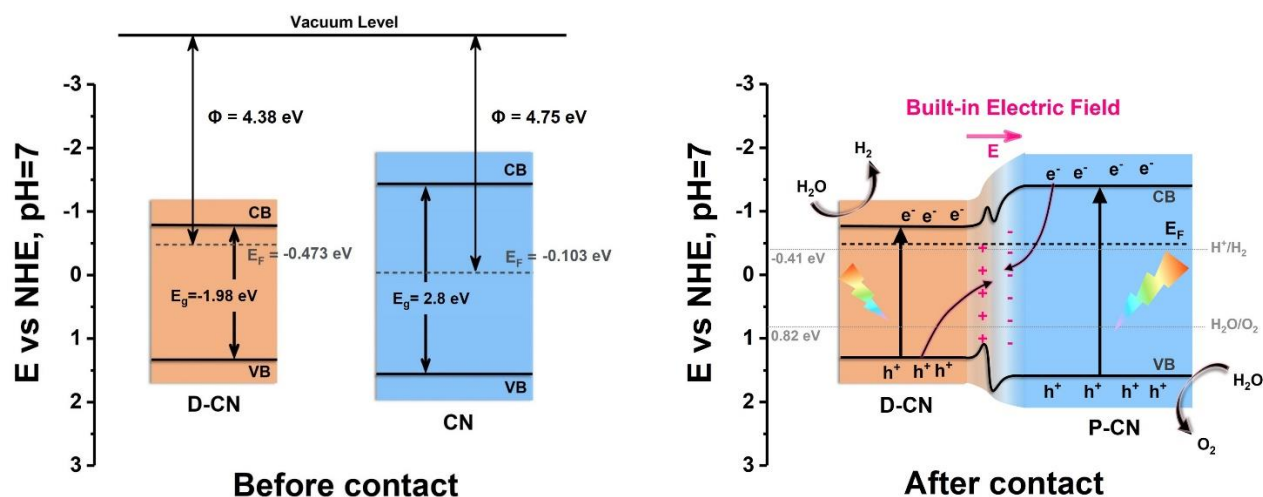


**Fig. 3.16.** Illustration of a plausible mechanism of peptide-modified CN.

The DFT computation was further constructed for a deeper understanding of the thermodynamic process of hydrogen evolution. As presented in Fig. 3.17b, the bulk g-C<sub>3</sub>N<sub>4</sub> emerged as a poor surface for water adsorption with low adsorption energy. The mono-layer P-CN with negatively charged N encircled atoms show improved water adsorption energy of -0.38 eV. As expected, the inclined D-CN structure possesses the highest water adsorption energy of -1.05 which 2.7-time higher than single-layer P-CN and 8.75 times higher than that of bulk g-C<sub>3</sub>N<sub>4</sub> (Relative water adsorption models by DFT were shown in Fig. 3.18). In addition, the free energy of each reaction step in water dissociation was calculated, as shown in Fig. 3.17c. P-CN has a high energy barrier for breaking water molecular (H<sub>2</sub>O→H\*+OH\*) and large H adsorption free energy ( $\Delta G_{H^*} = 0.87$  eV), signifying thermodynamically unflavored hydrogen evolution. In contrast, D-CN exhibits drastically decrease in the activated energy barrier ( $\Delta G_{\text{barrier}} = 0.32$  eV). Importantly, the small and negative free energy  $\Delta G_{H^*} = -0.11$  eV indicates easier H adsorption/desorption [69]. Additionally, the electrostatic potential map of P-CN and D-CN was visualized in Fig. 3.17d. Particularly, the charge is distributed uniformly and symmetrically on the P-CN surface, reflecting high-rate charge recombination and a weak polarized surface for water dissociation. Nobly, it is found that the introduction of the inclined heptazine plane has changed critically the charge distribution which breaks the charge balance in the N-C<sub>3</sub> bond. As strong sp<sup>3</sup> orbital hybridization, N-C<sub>3</sub> bond limits conjugated electron movements which hinder electron transfer and charge redistribution [70]. Since the appearance of a distorted heptazine plane, the change in orientation of N-C<sub>3</sub> bond disrupts the charge balance between N-C bonding. Subsequently, electrons were delocalized, and the surface turned into polarization, which is beneficial for visible light response and suitable hydrogen evolution. In sum, the combination of all the advantages mentioned above makes 10R-CN the best candidate for visible-light-driven photocatalytic hydrogen generation.

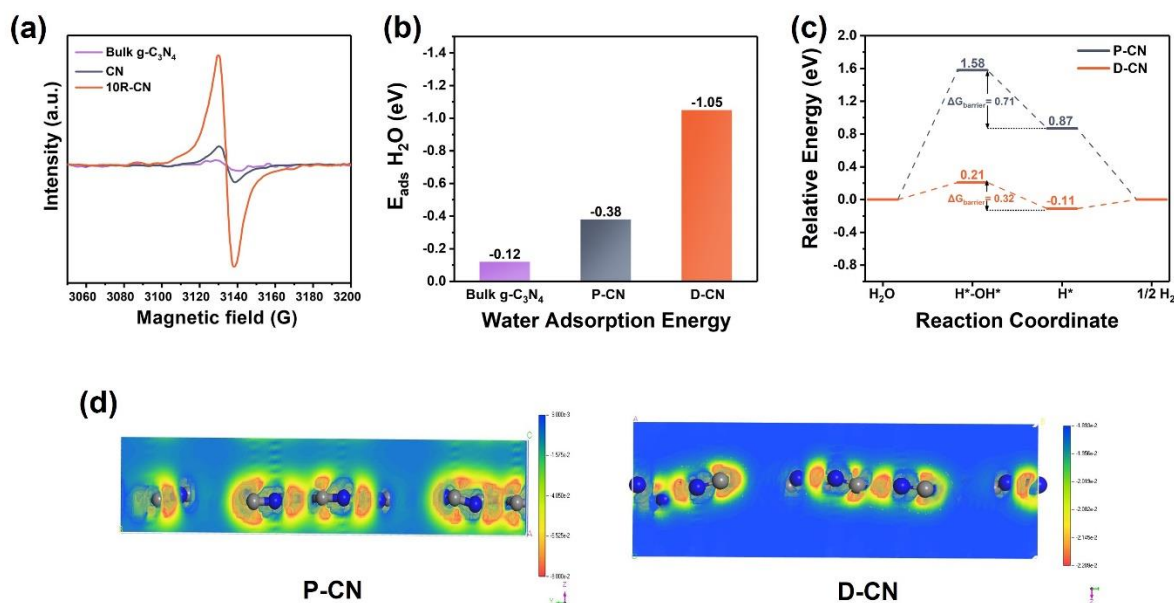


**Fig. 3.17.** (a) EPR, (b) Water adsorption energy of bulk  $g\text{-C}_3\text{N}_4$ , P-CN and D-CN. (c) Gibbs Free energy reaction pathway of water splitting, (d) electrostatic potential map of P-CN and D-CN calculated by VESTA.

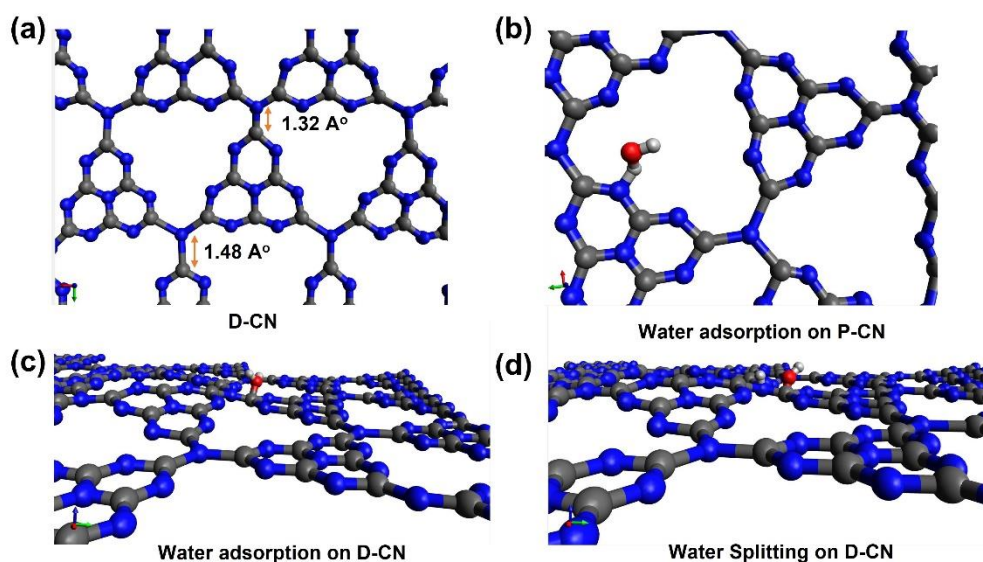


**Fig. 3.18.** (a) Optimized geometry of D-CN. DFT computed water adsorption models of (b) P-CN and (c) D-CN. And (d) illustration of water splitting on D-CN.

### 3.4. Summary

The porous g-C<sub>3</sub>N<sub>4</sub> was modified using RSTB1 via a facile bioinspired strategy to advance the solar-light-driven photocatalytic hydrogen generation. The amount of incorporated RSTB1 was optimized for the best performance in photocatalysis. Compared to the pristine CN, 10R-CN presented an improved result toward solar-driven H<sub>2</sub> generation rate of 2018  $\mu\text{mol g}^{-1} \text{h}^{-1}$ , which is 14 times the pristine CN. MD simulation has found electrostatic interaction between positive charge amine groups of peptide and negative pyridine N atoms attributing inclined heptazine planes as short-term disorder units. Experimental data and theoretical DFT calculation have determined the key role of heptazine planes in altering electronic configuration and breaking charge balance on the plane, thereby leading to electron delocalization. As a result of that, more new CB states appear toward the Fermi level which effectively narrows the band gap. Besides, an internal electric field formed by inclined-heptazine-planes and long-term g-C<sub>3</sub>N<sub>4</sub> surface boosted photo-induced electron-hole pair separation through the S-scheme mechanism. Nobly, this short-range disorder optimizes the adsorption/desorption free energy toward hydrogen evolution. Peptide-modified g-C<sub>3</sub>N<sub>4</sub> with enhanced photocatalytic activity might provide a new aspect for more economical modification studies regarding metal-free photocatalytic hydrogen generation.

## Reference

- [1] X.C. Meng, Z.H. Zhang, X.G. Li, Synergetic photoelectrocatalytic reactors for environmental remediation: A review, *J Photoch Photobio C*, 24 (2015) 83-101.
- [2] F. Rao, J. Zhong, J. Li, Improved visible light responsive photocatalytic hydrogen production over g-C<sub>3</sub>N<sub>4</sub> with rich carbon vacancies, *Ceramics International*, 48 (2022) 1439-1445.
- [3] Q. Zhu, Z. Xu, B. Qiu, M. Xing, J. Zhang, Emerging Cocatalysts on g-C<sub>3</sub>N<sub>4</sub> for Photocatalytic Hydrogen Evolution, *Small*, 17 (2021) e2101070.
- [4] Q. Duc Dao, T. Kim Anh Nguyen, T. Truong Dang, S. Gu Kang, H. Nguyen-Phu, L. Thi Do, V. Kim Hieu Van, K.H. Chung, J. Suk Chung, E. Woo Shin, Anchoring highly distributed Pt species over oxidized graphitic carbon nitride for photocatalytic hydrogen evolution: The effect of reducing agents, *Applied Surface Science*, 609 (2023).
- [5] M. Inagaki, T. Tsumura, T. Kinumoto, M. Toyoda, Graphitic carbon nitrides (g-C<sub>3</sub>N<sub>4</sub>) with comparative discussion to carbon materials, *Carbon*, 141 (2019) 580-607.
- [6] T.T. Dang, T.K.A. Nguyen, K.C. Bhamu, T. Mahvelati-Shamsabadi, V.K.H. Van, E.W. Shin, K.-H. Chung, S.H. Hur, W.M. Choi, S.G. Kang, J.S. Chung, Engineering Holey Defects on 2D Graphitic Carbon Nitride Nanosheets by Solvolysis in Organic Solvents, *ACS Catalysis*, 12 (2022) 13763-13780.
- [7] S. Yang, Y. Gong, J. Zhang, L. Zhan, L. Ma, Z. Fang, R. Vajtai, X. Wang, P.M. Ajayan, Exfoliated graphitic carbon nitride nanosheets as efficient catalysts for hydrogen evolution under visible light, *Adv Mater*, 25 (2013) 2452-2456.
- [8] T.K.A. Nguyen, T.-T. Pham, B. Gendensuren, E.-S. Oh, E.W. Shin, Defect engineering of water-dispersible g-C<sub>3</sub>N<sub>4</sub> photocatalysts by chemical oxidative etching of bulk g-C<sub>3</sub>N<sub>4</sub> prepared in different calcination atmospheres, *Journal of Materials Science & Technology*, 103 (2022) 232-243.
- [9] Y.B. Jiang, Z.Z. Sun, C. Tang, Y.X. Zhou, L. Zeng, L.M. Huang, Enhancement of photocatalytic hydrogen evolution activity of porous oxygen doped g-C<sub>3</sub>N<sub>4</sub> with nitrogen defects induced by changing electron transition, *Appl. Catal. B: Environ.*, 240 (2019) 30-38.
- [10] F. Wu, X. Li, W. Liu, S. Zhang, Highly enhanced photocatalytic degradation of methylene blue over the indirect all-solid-state Z-scheme g-C<sub>3</sub>N<sub>4</sub>-RGO-TiO<sub>2</sub> nanoheterojunctions, *Applied Surface Science*, 405 (2017) 60-70.
- [11] D. Yang, X. Zhao, Y. Chen, W. Wang, Z. Zhou, Z. Zhao, Z. Jiang, Synthesis of g-C<sub>3</sub>N<sub>4</sub> Nanosheet/TiO<sub>2</sub> Heterojunctions Inspired by Bioadhesion and Biomineralization Mechanism, *Industrial & Engineering Chemistry Research*, 58 (2019) 5516-5525.
- [12] W.-K. Jo, S. Kumar, S. Eslava, S. Tonda, Construction of Bi<sub>2</sub>WO<sub>6</sub>/RGO/g-C<sub>3</sub>N<sub>4</sub> 2D/2D/2D hybrid Z-scheme heterojunctions with large interfacial contact area for efficient charge separation and high-performance photoreduction of CO<sub>2</sub> and H<sub>2</sub>O into solar fuels, *Appl. Catal. B: Environ.*, 239 (2018) 586-598.
- [13] L. Huang, H. Xu, Y. Li, H. Li, X. Cheng, J. Xia, Y. Xu, G. Cai, Visible-light-induced WO<sub>3</sub>/g-C<sub>3</sub>N<sub>4</sub> composites with enhanced photocatalytic activity, *Dalton Trans*, 42 (2013) 8606-8616.
- [14] L. Ma, H. Fan, K. Fu, S. Lei, Q. Hu, H. Huang, G. He, Protonation of Graphitic Carbon Nitride (g-C<sub>3</sub>N<sub>4</sub>) for an Electrostatically Self-Assembling Carbon@g-C<sub>3</sub>N<sub>4</sub> Core-Shell Nanostructure toward High Hydrogen Evolution, *ACS Sustainable Chemistry & Engineering*, 5 (2017) 7093-7103.
- [15] T. Sano, S. Tsutsui, K. Koike, T. Hirakawa, Y. Teramoto, N. Negishi, K. Takeuchi, Activation of graphitic carbon nitride (g-C<sub>3</sub>N<sub>4</sub>) by alkaline hydrothermal treatment for photocatalytic NO oxidation in gas phase, *Journal of Materials Chemistry A*, 1 (2013) 6489-6496.



- [16] H. Mohtasham, B. Gholipour, S. Rostamnia, A. Ghiasi-Moaser, M. Farajzadeh, N. Nouruzi, H.W. Jang, R.S. Varma, M. Shokouhimehr, Hydrothermally exfoliated P-doped g-C<sub>3</sub>N<sub>4</sub> decorated with gold nanorods for highly efficient reduction of 4-nitrophenol, *Colloid Surface A*, 614 (2021).
- [17] J. Fang, H. Fan, M. Li, C. Long, Nitrogen self-doped graphitic carbon nitride as efficient visible light photocatalyst for hydrogen evolution, *Journal of Materials Chemistry A*, 3 (2015) 13819-13826.
- [18] Y. Wang, S. Shen, Progress and Prospects of Non-Metal Doped Graphitic Carbon Nitride for Improved Photocatalytic Performances, *Acta Physico-Chimica Sinica*, 36 (2020) 1905080-1905080.
- [19] H. Wang, Q. Lin, L. Yin, Y. Yang, Y. Qiu, C. Lu, H. Yang, Biomimetic Design of Hollow Flower-Like g-C<sub>3</sub>N<sub>4</sub>@PDA Organic Framework Nanospheres for Realizing an Efficient Photoreactivity, *Small*, 15 (2019) e1900011.
- [20] X. Liu, Y. Ji, Y. Du, X. Jing, Y. Zhao, K. Dou, L. Yu, L. Chu, Q. Zhou, M. Sun, A “green” all-organic heterostructure functionalized by self-assembled fullerene small molecule with enhanced photocatalytic activity, *Applied Surface Science*, 585 (2022).
- [21] I. Ghosh, J. Khamrai, A. Savateev, N. Shlapakov, M. Antonietti, B. Konig, Organic semiconductor photocatalyst can bifunctionalize arenes and heteroarenes, *Science*, 365 (2019) 360-+.
- [22] D. Yang, W. Wang, K. An, Y. Chen, Z. Zhao, Y. Gao, Z. Jiang, Bioinspired construction of carbonized poly(tannic acid)/g-C<sub>3</sub>N<sub>4</sub> nanorod photocatalysts for organics degradation, *Applied Surface Science*, 562 (2021).
- [23] P. Zhang, J. Zhang, D. Wang, F. Zhang, Y. Zhao, M. Yan, C. Zheng, Q. Wang, M. Long, C. Chen, Modification of g-C<sub>3</sub>N<sub>4</sub> with hydroxyethyl cellulose as solid proton donor via hydrogen bond to enhance H<sub>2</sub>O<sub>2</sub> production, *Appl. Catal. B: Environ.*, 318 (2022).
- [24] B. Zhao, J. Xu, Y. Liu, J. Fan, H. Yu, Amino group-rich porous g-C<sub>3</sub>N<sub>4</sub> nanosheet photocatalyst: Facile oxalic acid-induced synthesis and improved H<sub>2</sub>-evolution activity, *Ceramics International*, 47 (2021) 18295-18303.
- [25] Y. Chen, X. Xin, D. Yang, H. Ren, Y. Gao, Z. Zhao, W. Wang, K. An, J. Tan, Z. Jiang, Pyrimidine-modified g-C<sub>3</sub>N<sub>4</sub> nanosheets for enhanced photocatalytic H<sub>2</sub> evolution, *Mater Res Bull*, 144 (2021).
- [26] S. Plimpton, Fast Parallel Algorithms for Short-Range Molecular Dynamics, *Journal of Computational Physics*, 117 (1995) 1-19.
- [27] D.S. Kleinerman, C. Czaplewski, A. Liwo, H.A. Scheraga, Implementations of Nosé–Hoover and Nosé–Poincaré thermostats in mesoscopic dynamic simulations with the united-residue model of a polypeptide chain, *The Journal of Chemical Physics*, 128 (2008).
- [28] P. Giannozzi, S. Baroni, N. Bonini, M. Calandra, R. Car, C. Cavazzoni, D. Ceresoli, G.L. Chiarotti, M. Cococcioni, I. Dabo, A. Dal Corso, S. de Gironcoli, S. Fabris, G. Fratesi, R. Gebauer, U. Gerstmann, C. Gougoussis, A. Kokalj, M. Lazzeri, L. Martin-Samos, N. Marzari, F. Mauri, R. Mazzarello, S. Paolini, A. Pasquarello, L. Paulatto, C. Sbraccia, S. Scandolo, G. Sclauzero, A.P. Seitsonen, A. Smogunov, P. Umari, R.M. Wentzcovitch, QUANTUM ESPRESSO: a modular and open-source software project for quantum simulations of materials, *Journal of Physics: Condensed Matter*, 21 (2009) 395502.
- [29] P. Giannozzi, O. Baseggio, P. Bonfà, D. Brunato, R. Car, I. Carnimeo, C. Cavazzoni, S. de Gironcoli, P. Delugas, F. Ferrari Ruffino, A. Ferretti, N. Marzari, I. Timrov, A. Urru, S. Baroni, Quantum ESPRESSO toward the exascale, *The Journal of Chemical Physics*, 152 (2020).
- [30] J.P. Perdew, K. Burke, M. Ernzerhof, Generalized Gradient Approximation Made Simple, *Physical Review Letters*, 77 (1996) 3865-3868.
- [31] M. Re Fiorentin, F. Risplendi, M. Palumbo, G. Cicero, First-Principles Calculations of Exciton Radiative Lifetimes in Monolayer Graphitic Carbon Nitride Nanosheets: Implications for

- Photocatalysis, *ACS Applied Nano Materials*, 4 (2021) 1985-1993.
- [32] D. Vanderbilt, Soft self-consistent pseudopotentials in a generalized eigenvalue formalism, *Physical Review B*, 41 (1990) 7892-7895.
- [33] S. Grimme, J. Antony, S. Ehrlich, H. Krieg, A consistent and accurate ab initio parametrization of density functional dispersion correction (DFT-D) for the 94 elements H-Pu, *The Journal of Chemical Physics*, 132 (2010).
- [34] H.J. Monkhorst, J.D. Pack, Special points for Brillouin-zone integrations, *Physical Review B*, 13 (1976) 5188-5192.
- [35] G. Henkelman, B.P. Uberuaga, H. Jónsson, A climbing image nudged elastic band method for finding saddle points and minimum energy paths, *The Journal of Chemical Physics*, 113 (2000) 9901-9904.
- [36] S. Beck, A. Hampel, O. Parcollet, C. Ederer, A. Georges, Charge self-consistent electronic structure calculations with dynamical mean-field theory using Quantum ESPRESSO, Wannier 90 and TRIQS, *Journal of Physics: Condensed Matter*, 34 (2022) 235601.
- [37] X. Zeng, Y. Liu, Y. Kang, Q. Li, Y. Xia, Y. Zhu, H. Hou, M.H. Uddin, T.R. Gengenbach, D. Xia, C. Sun, D.T. McCarthy, A. Deletic, J. Yu, X. Zhang, Simultaneously Tuning Charge Separation and Oxygen Reduction Pathway on Graphitic Carbon Nitride by Polyethylenimine for Boosted Photocatalytic Hydrogen Peroxide Production, *ACS Catalysis*, 10 (2020) 3697-3706.
- [38] C.W. Jones, C.G. Morales, S.L. Eltiste, F.E. Yanchik-Slade, N.R. Lee, B.L. Nilsson, Capacity for increased surface area in the hydrophobic core of beta-sheet peptide bilayer nanoribbons, *J Pept Sci*, 27 (2021) e3334.
- [39] Y. Qian, H. Lai, J. Ma, G. Deng, B. Long, T. Song, L. Liu, X. Wang, Y. Tong, Molten salt synthesis of KCl-preintercalated C(3)N(4) nanosheets with abundant pyridinic-N as a superior anode with 10 K cycles in lithium ion battery, *J Colloid Interface Sci*, 606 (2022) 537-543.
- [40] Y.Y. Kang, Y.Q. Yang, L.C. Yin, X.D. Kang, G. Liu, H.M. Cheng, An Amorphous Carbon Nitride Photocatalyst with Greatly Extended Visible-Light-Responsive Range for Photocatalytic Hydrogen Generation, *Advanced Materials*, 27 (2015) 4572-4577.
- [41] D.Q. Dao, T.K. Anh Nguyen, S.G. Kang, E.W. Shin, Engineering Oxidation States of a Platinum Cocatalyst over Chemically Oxidized Graphitic Carbon Nitride Photocatalysts for Photocatalytic Hydrogen Evolution, *ACS Sustainable Chemistry & Engineering*, 9 (2021) 14537-14549.
- [42] X.X. Jin, L.X. Zhang, X.Q. Fan, J.J. Tian, M. Wang, J.L. Shi, A photo-excited electron transfer hyperchannel constructed in Pt-dispersed pyrimidine-modified carbon nitride for remarkably enhanced water-splitting photocatalytic activity, *Appl. Catal. B: Environ.*, 237 (2018) 888-894.
- [43] A. Kumar, H.-P. Komsa, D. Praveen Pathak, B. Marriyappan Sivagnanam, A.S.K. Sinha, J. Karthikeyan, Origin of Enhanced Photocatalytic Activity in Direct Band Gap g-C<sub>3</sub>N<sub>4</sub> Nanoribbons with Tunable Electronic Properties for Water-Splitting Reaction: A First-Principles Study, *The Journal of Physical Chemistry C*, 126 (2022) 19627-19636.
- [44] J. Cao, H. Fan, C. Wang, J. Ma, G. Dong, M. Zhang, Facile synthesis of carbon self-doped g-C<sub>3</sub>N<sub>4</sub> for enhanced photocatalytic hydrogen evolution, *Ceramics International*, 46 (2020) 7888-7895.
- [45] Y. Yi, S. Wang, H. Zhang, J. Liu, X. Lu, L. Jiang, C. Sui, H. Fan, S. Ai, J. Sun, High mobility organic semiconductor for constructing high efficiency carbon nitride heterojunction photocatalysts, *Journal of Materials Chemistry C*, 8 (2020) 17157-17161.
- [46] Z. Du, P. Sun, K. Wu, X. Zheng, X. Zhang, J. Huang, D. Sun, Y. Zheng, Q. Li, g-C<sub>3</sub>N<sub>4</sub>-SiC-Pt for Enhanced Photocatalytic H<sub>2</sub> Production from Water under Visible Light Irradiation, *Energy Technology*, 7 (2019).

- [47] W. Zhou, T. Jia, H. Shi, D. Yu, W. Hong, X. Chen, Conjugated polymer dots/graphitic carbon nitride nanosheet heterojunctions for metal-free hydrogen evolution photocatalysis, *Journal of Materials Chemistry A*, 7 (2019) 303-311.
- [48] A. Speltini, A. Scalabrini, F. Maraschi, M. Sturini, A. Pisanu, L. Malavasi, A. Profumo, Improved photocatalytic H<sub>2</sub> production assisted by aqueous glucose biomass by oxidized g-C<sub>3</sub>N<sub>4</sub>, *Int J Hydrogen Energ*, 43 (2018) 14925-14933.
- [49] H. Wang, G. Huang, Z. Chen, W. Li, Carbon Self-Doped Carbon Nitride Nanosheets with Enhanced Visible-Light Photocatalytic Hydrogen Production, *Catalysts*, 8 (2018).
- [50] L. Kong, Y. Ji, Z. Dang, J. Yan, P. Li, Y. Li, S.F. Liu, g-C<sub>3</sub>N<sub>4</sub> Loading Black Phosphorus Quantum Dot for Efficient and Stable Photocatalytic H<sub>2</sub> Generation under Visible Light, *Advanced Functional Materials*, 28 (2018).
- [51] J. Ran, W. Guo, H. Wang, B. Zhu, J. Yu, S.Z. Qiao, Metal-Free 2D/2D Phosphorene/g-C<sub>3</sub>N<sub>4</sub> Van der Waals Heterojunction for Highly Enhanced Visible-Light Photocatalytic H<sub>2</sub> Production, *Adv Mater*, 30 (2018) e1800128.
- [52] G. Zhou, Y. Shan, Y. Hu, X. Xu, L. Long, J. Zhang, J. Dai, J. Guo, J. Shen, S. Li, L. Liu, X. Wu, Half-metallic carbon nitride nanosheets with micro grid mode resonance structure for efficient photocatalytic hydrogen evolution, *Nat Commun*, 9 (2018) 3366.
- [53] J. Chen, C.L. Dong, D. Zhao, Y.C. Huang, X. Wang, L. Samad, L. Dang, M. Shearer, S. Shen, L. Guo, Molecular Design of Polymer Heterojunctions for Efficient Solar-Hydrogen Conversion, *Adv Mater*, 29 (2017).
- [54] R.S. Sprick, B. Bonillo, R. Clowes, P. Guiglion, N.J. Brownbill, B.J. Slater, F. Blanc, M.A. Zwijnenburg, D.J. Adams, A.I. Cooper, Visible-Light-Driven Hydrogen Evolution Using Planarized Conjugated Polymer Photocatalysts, *Angew Chem Weinheim Bergstr Ger*, 128 (2016) 1824-1828.
- [55] F. He, G. Chen, Y. Zhou, Y. Yu, L. Li, S. Hao, B. Liu, ZIF-8 derived carbon (C-ZIF) as a bifunctional electron acceptor and HER cocatalyst for g-C<sub>3</sub>N<sub>4</sub>: construction of a metal-free, all carbon-based photocatalytic system for efficient hydrogen evolution, *Journal of Materials Chemistry A*, 4 (2016) 3822-3827.
- [56] S. Fang, Y. Xia, K. Lv, Q. Li, J. Sun, M. Li, Effect of carbon-dots modification on the structure and photocatalytic activity of g-C<sub>3</sub>N<sub>4</sub>, *Appl. Catal. B: Environ.*, 185 (2016) 225-232.
- [57] Y. Ma, E. Liu, X. Hu, C. Tang, J. Wan, J. Li, J. Fan, A simple process to prepare few-layer g-C<sub>3</sub>N<sub>4</sub> nanosheets with enhanced photocatalytic activities, *Applied Surface Science*, 358 (2015) 246-251.
- [58] X. Xia, N. Deng, G. Cui, J. Xie, X. Shi, Y. Zhao, Q. Wang, W. Wang, B. Tang, NIR light induced H<sub>2</sub> evolution by a metal-free photocatalyst, *Chem Commun (Camb)*, 51 (2015) 10899-10902.
- [59] Q. Liang, Z. Li, Z.-H. Huang, F. Kang, Q.-H. Yang, Holey Graphitic Carbon Nitride Nanosheets with Carbon Vacancies for Highly Improved Photocatalytic Hydrogen Production, *Advanced Functional Materials*, 25 (2015) 6885-6892.
- [60] A. Suryawanshi, P. Dhanasekaran, D. Mhamane, S. Kelkar, S. Patil, N. Gupta, S. Ogale, Doubling of photocatalytic H<sub>2</sub> evolution from g-C<sub>3</sub>N<sub>4</sub> via its nanocomposite formation with multiwall carbon nanotubes: Electronic and morphological effects, *Int J Hydrogen Energ*, 37 (2012) 9584-9589.
- [61] F. He, G. Chen, Y. Yu, S. Hao, Y. Zhou, Y. Zheng, Facile approach to synthesize g-PAN/g-C<sub>3</sub>N<sub>4</sub> composites with enhanced photocatalytic H<sub>2</sub> evolution activity, *ACS Appl Mater*

- Interfaces, 6 (2014) 7171-7179.
- [62] S.Y. Gao, X.Y. Wang, C.J. Song, S.J. Zhou, F. Yang, Y. Kong, Engineering carbon-defects on ultrathin g-C<sub>3</sub>N<sub>4</sub> allows one-pot output and dramatically boosts photoredox catalytic activity, *Appl. Catal. B: Environ.*, 295 (2021).
- [63] X. Zhang, D. Kim, J. Yan, L.Y.S. Lee, Photocatalytic CO<sub>2</sub> Reduction Enabled by Interfacial S-Scheme Heterojunction between Ultrasmall Copper Phosphosulfide and g-C<sub>3</sub>N<sub>4</sub>, *Acs Appl Mater Inter*, 13 (2021) 9762-9770.
- [64] Q.L. Xu, L.Y. Zhang, B. Cheng, J.J. Fan, J.G. Yu, S-Scheme Heterojunction Photocatalyst, *Chem-US*, 6 (2020) 1543-1559.
- [65] X.Q. Tan, S.F. Ng, A.R. Mohamed, W.J. Ong, Point-to-face contact heterojunctions: Interfacial design of 0D nanomaterials on 2D g-C<sub>3</sub>N<sub>4</sub> towards photocatalytic energy applications, *Carbon Energy*, 4 (2022) 665-730.
- [66] A. Naseri, M. Samadi, A. Pourjavadi, A.Z. Moshfegh, S. Ramakrishna, Graphitic carbon nitride (g-C<sub>3</sub>N<sub>4</sub>)-based photocatalysts for solar hydrogen generation: recent advances and future development directions, *Journal of Materials Chemistry A*, 5 (2017) 23406-23433.
- [67] Y.F. Liu, M.F. He, R. Guo, Z.R. Fang, S.F. Kang, Z. Ma, M.D. Dong, W.L. Wang, L.F. Cui, Ultrastable metal-free near-infrared-driven photocatalysts for H<sub>2</sub> production based on protonated 2D g-C<sub>3</sub>N<sub>4</sub> sensitized with Chlorin e6, *Appl. Catal. B: Environ.*, 260 (2020).
- [68] L. Yang, J. Huang, L. Shi, L. Cao, Q. Yu, Y. Jie, J. Fei, H. Ouyang, J. Ye, A surface modification resultant thermally oxidized porous g-C<sub>3</sub>N<sub>4</sub> with enhanced photocatalytic hydrogen production, *Appl. Catal. B: Environ.*, 204 (2017) 335-345.
- [69] F. Li, G.-F. Han, H.-J. Noh, J.-P. Jeon, I. Ahmad, S. Chen, C. Yang, Y. Bu, Z. Fu, Y. Lu, J.-B. Baek, Balancing hydrogen adsorption/desorption by orbital modulation for efficient hydrogen evolution catalysis, *Nature Communications*, 10 (2019) 4060.
- [70] P. Xia, B. Cheng, J. Jiang, H. Tang, Localized  $\pi$ -conjugated structure and EPR investigation of g-C<sub>3</sub>N<sub>4</sub> photocatalyst, *Applied Surface Science*, 487 (2019) 335-342.

## CHAPTER 4. Conclusion

With the world facing pressing challenges related to energy shortages and environmental degradation, the development of efficient and sustainable energy technologies is of paramount importance. Photocatalysis, a green process capable of harnessing solar energy, holds great promise in this regard. While traditional semiconductor metal oxides have demonstrated impressive performance, there is a need for improved photocatalytic materials with larger surface areas, suitable redox potentials, and optimized bandgaps. Moreover, the synthesis and modification of photocatalysts must transition towards more environmentally friendly and accessible approaches. By drawing inspiration from biomineralization processes found in nature, the bioinspired modification of TiO<sub>2</sub> and g-C<sub>3</sub>N<sub>4</sub> has been explored as a means to enhance their photocatalytic efficiency. These endeavors represent significant strides toward realizing sustainable and efficient photocatalytic technologies for a greener future.

In this thesis, the bioinspired synthesis and modification of semiconductors such as titanium dioxide and graphitic carbon nitride were briefly introduced. The multiple solar light-driven photocatalytic applications (dye degradation and hydrogen generation) and corresponding mechanisms were investigated. In Chapter 2, the biomineralization of TiO<sub>2</sub> through a lysozyme (LYZ)-polystyrene (PS) biotemplate was illustrated. LYZ was well-covered on the PS surface by a simple passive adsorption process. The effect of pH, adsorption time, and the initial concentration of lysozyme were investigated. Then, the optimized LYZ-PS template was utilized to act as the core for the TiO<sub>2</sub> mineralization. The pyrolysis of PS after calcination enlarged the pore structures of the composite. The transformation of crystalline phases of TiO<sub>2</sub> was also studied. By varying the calcination temperature, a clear transition from anatase to anatase/rutile mixed phase was exhibited. The results confirmed that the harnessed photocatalytic degradation on RhB (98% degradation within 80 min under simulated solar irradiation) compared to the bare TiO<sub>2</sub> and LYZ-templated TiO<sub>2</sub> benefited from the nitrogen-rich biotemplate, mixed crystalline phase, and the construction of pore structure.

The development of biomaterial-based modification of g-C<sub>3</sub>N<sub>4</sub> for efficient free-metal visible-light photocatalytic H<sub>2</sub> generation is still a great challenge. In Chapter 3, a simple and green bioinspired route of g-C<sub>3</sub>N<sub>4</sub> nanosheet (CN) modification was addressed. Porous g-C<sub>3</sub>N<sub>4</sub> structure modified with biological molecular is successfully prepared by simply decorating a 14-mer peptide on porous g-C<sub>3</sub>N<sub>4</sub> (CN). The modified CN with special morphology and improved visible-light absorption performs a superior photocatalytic H<sub>2</sub> production which can possess a generation rate of 2018.4  $\mu\text{mol g}^{-1} \text{h}^{-1}$  without co-catalyst (i.e., Pt), which is about 14 folds higher than that of pristine CN (140.8  $\mu\text{mol g}^{-1} \text{h}^{-1}$ ). XPS spectra, along with MD and DFT computation have mainly identified that strained heptazine plane in g-C<sub>3</sub>N<sub>4</sub> structure, due to electrostatic interaction between positive-charge amine groups and negative-charge edge N atoms, plays a key role in contributing to electron redistribution and delocalization which may be attributed to band gap reduction, build-in electrical field, and electronic modulation, thus enhancing charge separation and optimized free energy of the reaction intermediates. This chapter provides a new route for designing excellent bio-based metal-free g-C<sub>3</sub>N<sub>4</sub>-based catalysts toward visible-light photocatalytic H<sub>2</sub> generation.

In summary, these chapters demonstrate the potential of biotemplates and bio-inspired modifications in enhancing photocatalytic processes. The utilization of nitrogen-rich biotemplates and the control of crystalline phases and pore structures have shown promising results in TiO<sub>2</sub> biomineralization. Similarly, the modification of g-C<sub>3</sub>N<sub>4</sub> with biological molecules has led to improved visible-light absorption and enhanced photocatalytic H<sub>2</sub> generation. These findings contribute to the development of efficient and environmentally friendly catalysts for various applications. Therefore, seeking a facile, non-toxic, and economical biomaterial and bioinspired method that are beneficial for advancing photocatalytic activities will be the next step of our work.